NCTSPM

NATIONAL CENTER FOR TRANSPORTATION SYSTEMS PRODUCTIVITY AND MANAGEMENT

Full-Scale Wall of Wind Testing of Variable Message Signs (VMS) to Develop Drag Coefficients for AASHTO Supports Specifications

Contract # DTRT12GUTC12 (AWD000000002293) with Research and Innovative Technology Administration (RITA)

Final Report

May 21, 2015

Principal Investigator: Dr. Arindam Gan Chowdhury (Florida International University)
Co-Principal Investigators: Dr. Amir Mirmiran (Florida International University)
Dr. Fouad H. Fouad (University of Alabama at Birmingham)
Dr. Ian Hosch (University of Alabama at Birmingham)

National Center for Transportation Systems Productivity and Management
O. Lamar Allen Sustainable Education Building
788 Atlantic Drive, Atlanta, GA 30332-0355
P: 404-894-2236   F: 404-894-2278
nctspm@ce.gatech.edu   nctspm.gatech.edu

Georgia Institute of Technology   FIU FLORIDA INTERNATIONAL UNIVERSITY   UAB THE UNIVERSITY OF ALABAMA AT BIRMINGHAM   UNIVERSITY OF CENTRAL FLORIDA

TABLE OF CONTENTS

LIST OF FIGURES

Executive Summary of Two Project Reports

A comprehensive study was conducted to develop and analyze drag coefficients for Variable Message Sign (VMS) structures for incorporation into the AASHTO Supports Specifications. The results and findings of the project are summarized in two reports prepared by Florida International University (FIU) and the University of Alabama at Birmingham (UAB). Report 1 (the current report), which is titled *Full-Scale Wall of Wind Testing of Variable Message Signs (VMS) to Develop Drag Coefficients for AASHTO Supports Specifications*, presents the experimental research conducted at the FIU Wall of Wind facility to develop the VMS drag coefficients. Report 2, *Investigation of Variable Message Sign (VMS) Drag Coefficients for AASHTO Supports Specifications*, discusses the experimental and analytical studies conducted at UAB to verify the accuracy of the proposed VMS drag coefficients and investigate the impact of the drag coefficients on the design of VMS structures.

1   INTRODUCTION

The increasing national interest in Intelligent Transportation Systems (ITS) and the need for more efficient transportation have led to the expanding use of variable message signs (VMS) technology. ITS improves safety and mobility by integrating advanced communication technology into the transportation infrastructure. VMS are the cornerstone of intelligent transportation systems and provide a high tech alternative to static flat panel signs. These remotely programmable traffic control devices relay to motorists real-time advisories about changing highway conditions and hazards such as inclement weather, traffic accidents, construction activity, congestion, and public service alerts. Variable message signs are substantially heavier than flat panel aluminum signs and have larger depth (dimension parallel to the direction of traffic, see Figure 1.1). The additional weight and depth can have a significant effect on the aerodynamic forces and inertial loads transmitted to the support structure.

Figure 1.1 VMS structures on Florida's Turnpike (a) side elevation (b) front elevation

VMS are typically installed on cantilever or bridge-type support structures. Figure 1.2 shows typical cantilever and bridge (or non-cantilever) VMS support structures. Cantilever support structures are characterized by a single vertical upright which supports a horizontal mast arm or truss. These structures have low natural frequencies in the range of 1 to 3 Hz and damping typically less than one percent of critical, resulting in highly flexible structures. These conditions make cantilever support structures particularly susceptible to large amplitude vibrations and fatigue problems (Kaczinski et al., 1998). Bridge type or non-cantilever structures are supported at each end by single or double vertical uprights and can span longer distances. They are typically more rigid than cantilever support structures and have a higher natural frequency. Table 1.1 shows the natural frequency of typical cantilever and non-cantilever structures determined from various research studies.
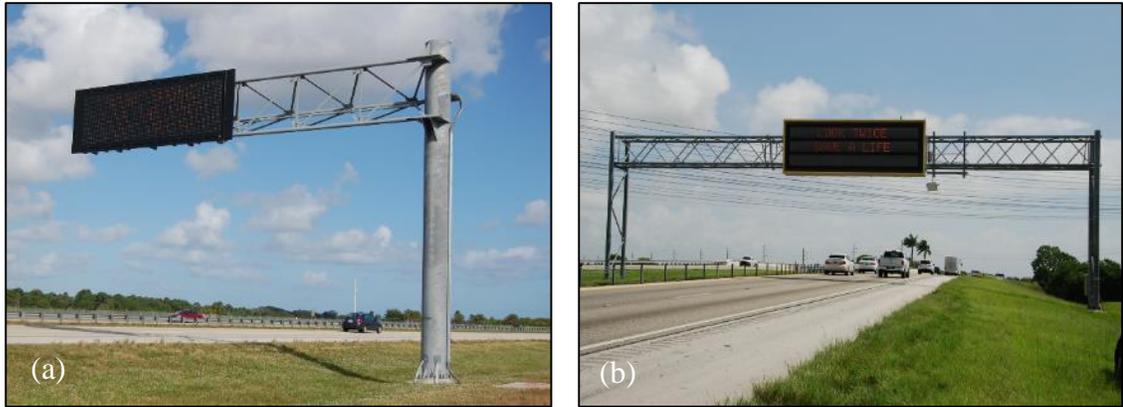
Figure 1.2 VMS structure types (a) cantilever (b) bridge or non-cantilever

Table 1.1 Typical natural frequencies for cantilever and non-cantilever structures

Support Type	Truss Type	Material	Truss Span (m)	VMS	Out of plane (Hz)	In plane (Hz)	Source
Cantilever	New Jersey; 2-chord	Steel	13.3	Yes	0.8	1.2	NCHRP 469 (200
Cantilever	California; 4-chord box	Steel	8.7	Yes	1.8	1.9	NCHRP 469 (200
Cantilever	Illinois; Vierendeel	Steel	10.3	Yes	1.3	1.9	NCHRP 469 (200
Cantilever	Illinois; 4-chord box	Alum.	9.4	Yes	1.0	1.4	NCHRP 469 (200
Cantilever	IDOT; 4 chord box	Alum.	9.1	No	2.3	2.5	Foutch et al (2006)
Cantilever	Monotube mast arm	Steel	10.6	No	1.2	1.3	Fouad et al (2002)
Cantilever	2 Chord	Steel	13.9	No	1.0	1.6	Fouad et al (2002)
Non-cantilever	IDOT; 4 chord box	Alum.	28.7	Yes	3.3	4.2	Foutch et al (2006)
Non-cantilever	IDOT; 4 chord box	Alum.	28.7	Yes	2.9	3.4	Foutch et al (2006)
Non-cantilever	WisDOT; 4 chord box	Steel	21.7	Yes	-	6.3	Ginal (2003)
Non-cantilever	WisDOT; 4 chord box	Steel	32.4	Yes	-	2.4	Ginal (2003)
Non-cantilever	WisDOT; 3 chord	Steel	20.5	No	-	8.4	Ginal (2003)
Non-cantilever	PennDOT; 4 chord box	Steel	59.1	No	2.4	1.9	Kacin (2007)
Non-cantilever	Monotube	Steel	30.5	No	0.9	1.2	Fouad et al (2002)
Non-cantilever	Monotube	Steel	18.3	No	1.1	2.1	Fouad et al (2002)
Non-cantilever	3 chord	Steel	25.0	No	4.1	3.1	Fouad et al (2002)
Non-cantilever	3 chord	Alum.	45.7	No	2.1	2.1	Fouad et al (2002)

Structure types can be categorized into four primary groups depending on the geometry of the horizontal span; 1) box truss, 2) tri-chord truss, 3) two-chord truss, and 4) monotubes. A typical example of each structure type is shown in Figure 1.3. Box trusses consist of four main chords positioned to form a three dimensional box. The main horizontal chords are typically large diameter tubes in single or multiple sections bolted together for longer spans. The truss elements consist of round welded pipe members or angles joined with

gusset plates. Tri-chord trusses are similar to box trusses but consist of three main members positioned to form a three dimensional triangle. Truss members, like the box truss, are typically round welded pipe members or angles joined with gusset plates. Two-chord trusses are planar structures consisting of two primary horizontal members with secondary members spanning vertically in-between. The truss may be composed of rounded or square tubular members arranged in triangular or rectangular patterns. Monotubes are large tubular structures of constant diameter or linearly tapered elements. The horizontal beam may be a single element or multiple linear sections joined together with bolted connections.
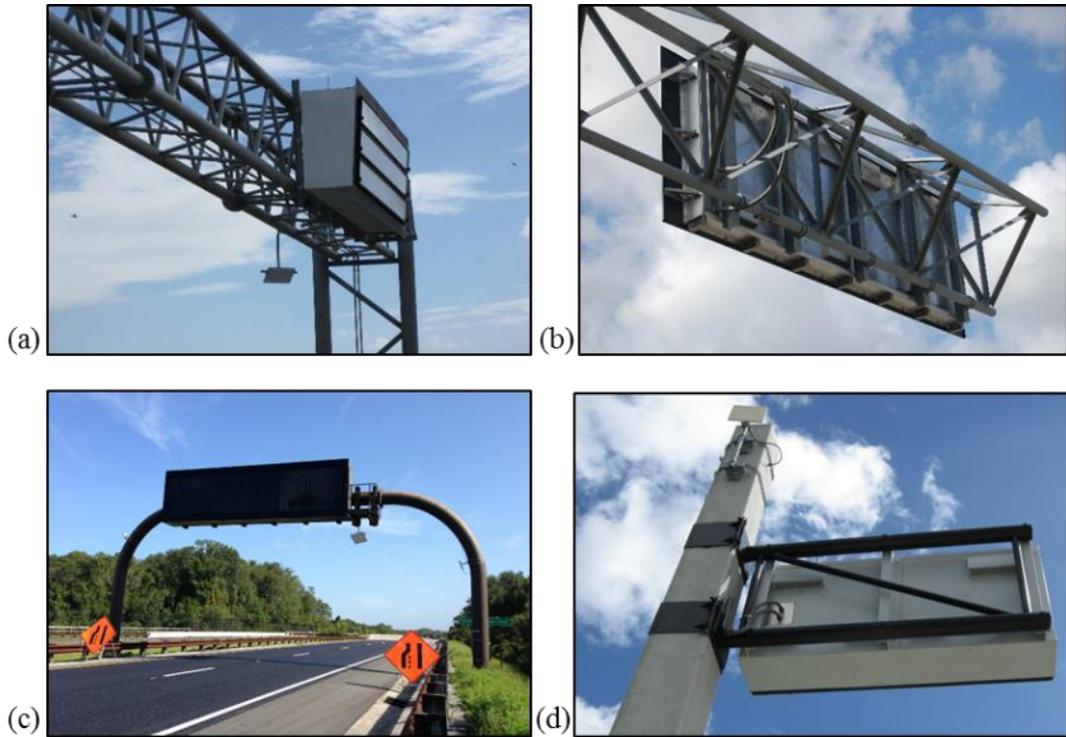
Figure 1.3 VMS support types (a) four-chord or box truss (b) three-chord or tri-chord truss (c) monotube (d) two-chord truss

There is no standard method for attaching VMS to the support structure. The number and size of the hangers and connectors will depend on the VMS size, weight, and shape. Typically, aluminum extrusions (z shapes, channels, W shapes, etc.) are arranged vertically and horizontally in a grid pattern depending on the access configuration (walk-in, rear access, front access) and support structure type. Generally, the hangers evenly distribute the weight of the sign to the attachment points on the support structure.

Several State Department of Transportations have reported wind induced vibrations and fatigue related problems in VMS support structures (Dexter and Ricker, 2002). These problems can lead to costly repairs, premature removal, and occasional structural failure. To address this issue, the American Association of State Highway and Transportation Officials Standard Specifications for Structural Supports for Highway Signs, Luminaires and Traffic Signals (AASHTO Specification, 2013) has identified four wind loading

mechanisms with potential for inducing large amplitude vibrations in VMS support structures: 1) galloping, 2) vortex shedding, 3) natural wind gusts, and 4) truck induced gusts. As indicated in Table 1.2, each VMS structure support type is susceptible to different wind loading phenomena.

Table 1.2 AASHTO fatigue design requirements for VMS structures (AASHTO, 2013)

Type of Structure	Galloping	Vortex Shedding	Natural Wind	Truck Gusts
Cantilever Sign (1-, 2- or 3-chord)	X	*	X	X
Cantilever Sign (four-chord)	**	*	X	X
Non-cantilever Sign		*	X	X

* Vortex shedding has occurred in a monopole bridge support and can occur in cantilevered structures if the sign attachment is not attached
** Owner may choose to exclude galloping loads for 4-chord trusses

1.1 Statement of problem and research objectives

Minimum strength and fatigue design requirements for VMS support structures are contained in the American Association of State Highway and Transportation Officials (AASHTO) Specification (2013). Table 3.8.6-1 of the Specification suggests for VMS a drag coefficient of 1.7 to be used in the wind pressure equation for strength and fatigue design. However, the code does not take into account the prismatic geometry of VMS and the complex interaction of the applied aerodynamic forces to the support structure.

The primary load on VMS structures is generally due to wind-induced drag. However, aeroelastic phenomena, caused by the interaction between the wind flow and the structure's vibrational characteristics, can lead to significant vertical forces. These forces may be due to the phenomena of vortex shedding and galloping instability. The resulting vibrations can lead to fatigue damage and ultimately failure of the structure (Kaczinski et al., 1998). Note that vortex shedding and galloping responses are characterized by aeroelastic feedback whereby motions of the structure normal to the direction of wind flow affect the flow itself and can amplify the aerodynamic force fluctuations.

In view of the lack of code guidance and the limited research performed so far, targeted experimentation and dynamic analysis was conducted in the Wall of Wind facility (WOW) at Florida International University (FIU) to provide reliable drag coefficients and investigate the susceptibility of VMS to aeroelastic instability.

The work includes an extensive literature review, investigation of industry standards, large-scale experimental testing in the 12-fan WOW facility at FIU, an in-depth analysis

4

of obtained data and formulation of drag coefficient recommendations for incorporation into the AASHTO Specification. Experimental objectives are as follows:

- Determine reliable drag coefficients for VMS with various geometric configurations.

- Investigate twisting moment coefficients and eccentricity ratios for VMS with various geometric configurations.

- Investigate Reynolds number effects on VMS drag coefficients.

- Investigate the effect of wind driven rain on drag coefficients.

- Characterize the mitigating effects of round and chamfered corners.

- Evaluate drag coefficient trends based on aspect (b/c) and depth (d/c) ratios.

Drag coefficient results from this study can be used by other researchers for finite element modeling/analysis (FEM) of full-scale VMS structures. Such analyses may focus on stresses generated at connections, design and selection of member sizes, base shear and moment, and foundation forces.

Since galloping and vortex shedding are also potentially important phenomena, the opportunity was taken to gather additional data. Since the drag calculation also involves the gust factor, a theoretical evaluation of the potential range of gust factors was carried out. These objects were as follows:

- Evaluate the galloping potential of VMS structures.

- Evaluate vortex shedding for VMS structures.

- Estimate gust factors and recommend drag force evaluation methodology for incorporation into the AASHTO Specification.

1.2 Terminology

Figure 1.4 is a picture of a full scale structure showing the primary dimensions of the VMS: lateral length b, height c, depth (along wind length) d, and the distance from the ground to the top of the model h. Geometric ratios used throughout this study were:

$$\text{Aspect ratio} = b/c \qquad\qquad (1\text{-}1)$$
$$\text{Depth ratio} = d/c \qquad\qquad (1\text{-}2)$$
$$\text{Clearance ratio} = c/h \qquad\qquad (1\text{-}3)$$
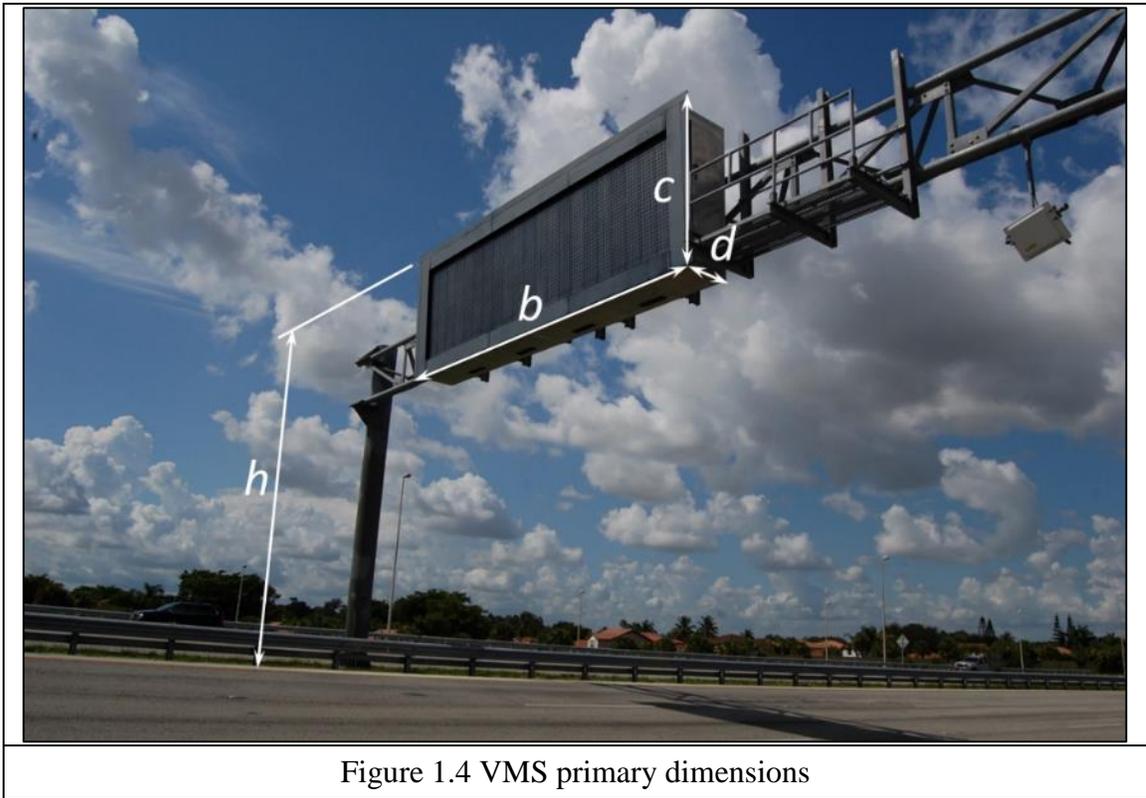
Figure 1.4 VMS primary dimensions

Two model support configurations were used for testing. The models were mounted on cantilever support masts which incorporated load cells. Two support masts were used for the longer models and a single support mast was used for the shorter models. These were called the double and single support configurations respectively. Figure 1.5 shows the axes and force orientation for the single and double support configuration used throughout the study. Body-axes have been used in this study as shown. The x-axis is positive in the along wind direction and the y-axis is positive to the right. The z-axis is positive in the upward direction and counterclockwise is positive for the twisting moment, M_z. The loads and moments measured by individual load cells for this study are also shown. Angle θ defines the horizontal wind approach direction and 0° is defined as wind normal to the front face of the model.
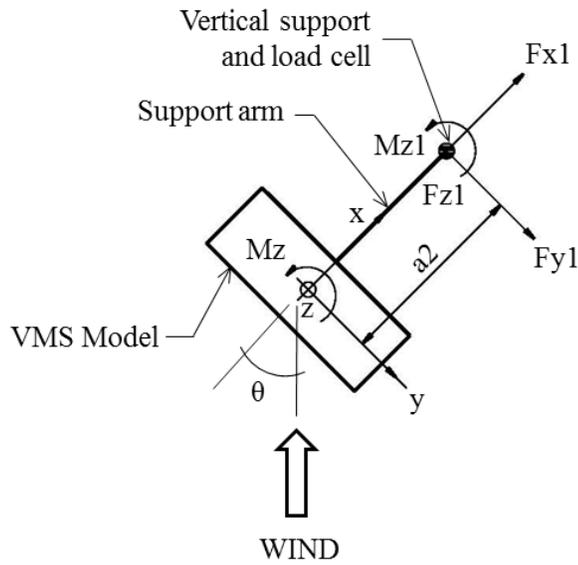
(a)

(b)
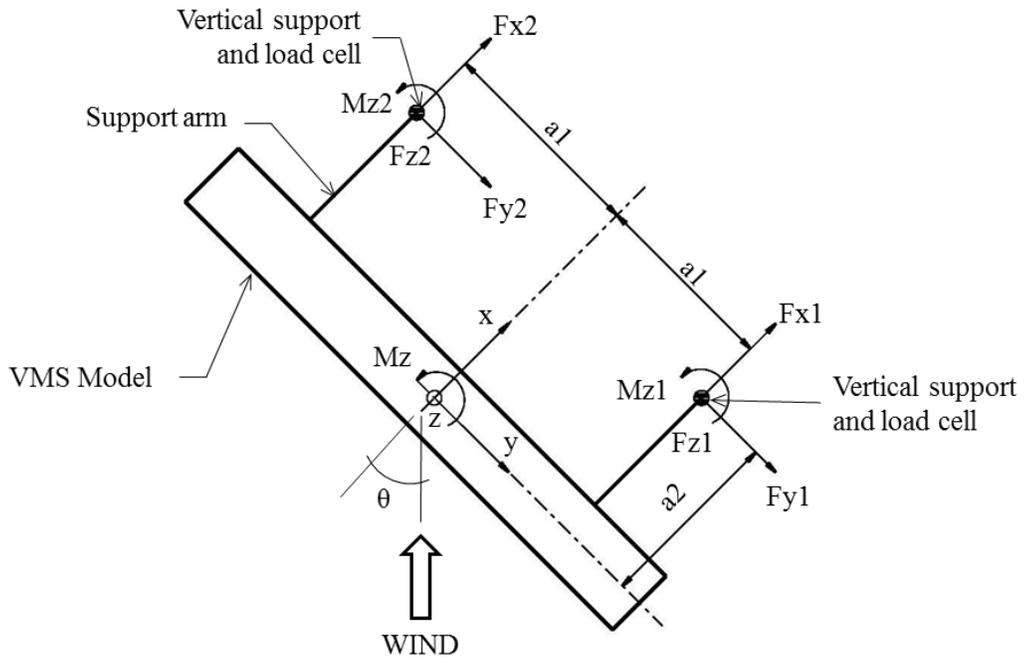
Figure 1.5 Force orientation (a) Single support configuration (b) Double support configuration

1.3 Force and moment coefficients

The time averaged aerodynamic forces on VMS subjected to wind loading can be expressed non-dimensionally as force coefficients defined as

$$C_{Fx} = \frac{F_x}{\frac{1}{2}\rho\bar{U}^2(bc)} \qquad (1\text{-}4)$$

$$C_{Fy} = \frac{F_y}{\frac{1}{2}\rho\bar{U}^2(bc)} \qquad (1\text{-}5)$$

$$C_{Fz} = \frac{F_z}{\frac{1}{2}\rho\bar{U}^2(bc)} \qquad (1\text{-}6)$$

where F_x, F_y and F_z are the resultant forces along the x, y and z axis respectively, ρ is the density of air (assumed as 1.225 kg/m³), $\bar{U}$ (m/s) is the mean wind speed, b (m) is the lateral length of the VMS, and c (m) is the height of the VMS. Refer to Figure 1.5 for axis and force orientation. The resultant forces used in this study for the single and double support configurations were determined as follows

Single Support Setup

$$F_x = F_{x1} \qquad (1\text{-}7)$$

$$F_y = F_{y1} \qquad (1\text{-}8)$$

$$F_z = F_{z1} \qquad (1\text{-}9)$$

Double Support Setup

$$F_x = F_{x1} + F_{x2} \qquad (1\text{-}10)$$

$$F_y = F_{y1} + F_{y2} \qquad (1\text{-}11)$$

$$F_z = F_{z1} + F_{z2} \qquad (1\text{-}12)$$

The force coefficients in this study were normalized using the area of the front face of the model (b x c), unless otherwise noted, and the forces were resolved into orthogonal components parallel and perpendicular to the body-axes of the structure (Figure 1.5). The resultant forces (F_x, F_y and F_z) and corresponding force coefficients (C_{Fx}, C_{Fy}, and C_{Fz}) along the x, y, and z axis are conventionally termed normal force, lateral force and vertical lift respectively. Numerical subscripts for F_x, F_y, and F_z refer to the component reactions at each load cell. See Figure 1.5 for the location and orientation of component forces. The moment about the z axis is termed the twisting moment and defined as

$$C_{Mz} = \frac{M_z}{\frac{1}{2}\rho\bar{U}^2(b^2 c)}$$

(1-13)

Where M_z is the moment around the centroidal z axis and calculated as

Single Support Setup

$$M_z = M_{z1} - F_{y1}{\cdot}a_2$$

(1-14)

Double Support Setup

$$M_z = M_{z1} + (F_{x1}{\cdot}a_1) - (F_{y1}{\cdot}a_2) + M_{z2} - (F_{x2}{\cdot}a_1) - (F_{y2}{\cdot}a_2)$$

(1-15)

where the centroidal moment arm for the x axis is a_1 and the centroidal moment arm for the y axis is a_2. Numerical subscripts for M_z refer to the moment at each load cell.

The eccentricity ratio about the central vertical (z) axis is defined as

$$\frac{r}{b} = \frac{C_{Mz}}{C_{Fx}}$$

(1-16)

where C_{Mz} is the mean twisting moment coefficient about the centroidal z axis, C_{Fx} is the mean normal force coefficient, r is the distance from the centroid of the model to the point of application of the force, and b is the lateral length of the model. See Figure 1.5 for the location and orientation of component forces.

2 BACKGROUND OF AERODYNAMICS RELATED TO SIGN STRUCTURES

2.1 General aerodynamics

VMS are generally rectangular prismatic shapes that are considered bluff bodies aerodynamically. The wind flow around a VMS is therefore characterized by separation from the upstream leading edges of the structure. This forms an outer flow region and an inner turbulent wake region separated by a thin layer of high shear and vorticity. This unstable free shear layer generates discrete vortices which are shed into the downstream wake region. The base pressure in the wake region determines the amount of vorticity that is shed from each side of the body which in turn affects the distance to vortex formation and the strength of the fully formed vortices (see Figure 2.1). This complex equilibrium between the vorticity shedding, the distance to vortex formation, and the base pressure significantly influences the pressure distribution and total forces experienced by the structure (Bearman and Trueman, 1972).
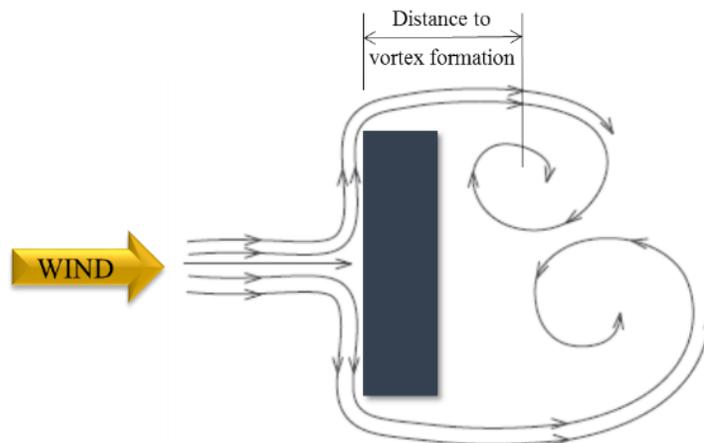
Figure 2.1 Flow around prismatic shape

2.1.1 Drag coefficients

Initially it was thought that the drag coefficient for flat panels was the same as for prismatic bluff bodies (i.e., for 2D and 3D shapes), with a value around 2. However, the drag coefficient for a 2D flat sign panel can be significantly different from the drag coefficient for a 3D prismatic VMS. This depends in part on whether separation of the flow at the leading edge is followed by reattachment along the sides. Many researchers have studied wind flow around rectangular prisms with different depth ratios to evaluate the potential for reattachment along the sides and the resulting effect on drag (Nakaguchi et al., 1968; Bearman and Truman, 1972; Laneville et al., 1975; Larose and D'Auteuil, 2008; Sohankar, 2008). An early study conducted by Bearman and Trueman (1972) investigated the difference between flow around thin plates (small values of d/c) and flow around prismatic rectangular shapes (large values of d/c). They demonstrated that the distance

from the leading edge separation point to the onset of vortex formation is longer (further downstream) for the elongated shape. Their results indicated that drag is affected by the downstream distance to vortex formation and the narrowness of the wake. Since vortices represent regions of low pressure, the further downstream that they form, the higher the base pressure and the lower the drag. Laneville et al. (1975) showed that in the case of thin shapes, where no reattachment occurs, free stream turbulence increases mixing and entrainment in the separated shear layers. This causes a decrease in base pressure (i.e., high magnitude of suction) and a reduced radius of curvature of the shear layer streamlines, resulting in an increase in drag. However, in the case of elongated shapes, reattachment along the sides of the body may occur if the entrainment within and across the shear layer is strong enough. The streamlines eventually separate from the trailing edges but the wake is narrower and the distance to vortex formation is further downstream, resulting in reduced drag.
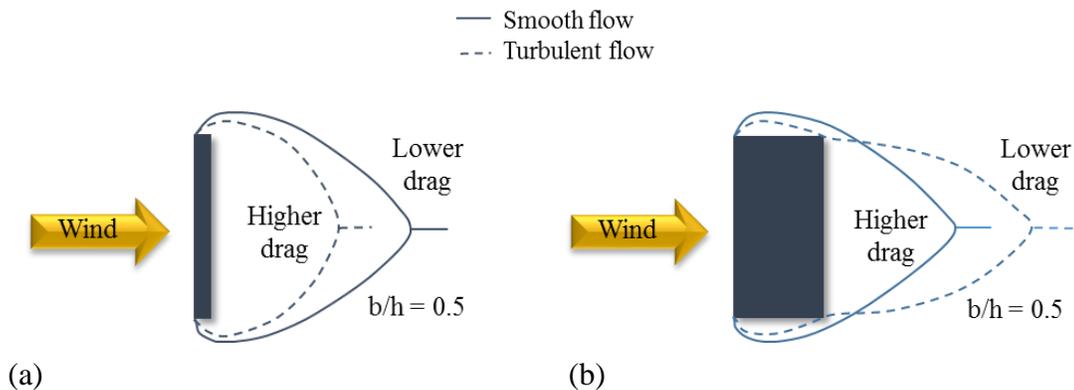
Figure 2.2 Sketches of dividing streamlines (Laneville et al. 1975) (a) thin shape (b) Elongated shape

Although numerous research studies have been conducted to investigate wind loading on prismatic bluff bodies, targeted experimental research to investigate elevated sign panels and VMS is very limited. Letchford (2001) conducted the first comprehensive investigation of the effect of drag on a variety of elevated flat panel sign geometries. A series of wind tunnel tests were performed in a simulated turbulent boundary layer on 1:50 scale flat rectangular sign models to investigate the effect of aspect ratio (b/c), clearance ratio (c/h), and wind direction on drag coefficients. Letchford's results demonstrated that for aspect ratios greater than one, as the sign panel becomes short and wide, the mean drag force increases for bigger gaps and decreases for smaller gaps. For aspect ratios less than one, as the panel becomes tall and skinny, the drag force increased irrespective of the clearance ratio. Letchford's (2001) drag coefficient results form the basis of the ASCE7-10 specification. Quinn et al. (2001) instrumented and monitored full scale roadside signs in the grass field at the Silsoe Research Institute. Results indicated that the sign shape did not appear to contribute significantly to the magnitude of the wind force coefficient. However, the addition of a frame around the square sign increased the force coefficient. The Quinn et al. (2001) results for mean force coefficients are considerably lower than

11

Letchford's (2001), even though the turbulence intensity for both studies was approximately 25%,

The previously discussed research focused on elevated flat panel signs. Recent studies conducted by Smith et al. (2014) and Zuo et al. (2014) investigated wind loading on elevated rectangular box signs (VMS). The study by Smith et al. (2014) consisted of measuring wind loads on a full scale VMS with geometric ratios $b/c = 2$, $d/c = 0.47$, and $c/h = 0.5$. The mean force coefficient was determined to be $C_{Fx} = 1.13$ and the eccentricity ratios (r/b) were generally less than 0.15. Smith et al. (2014) makes the point that the results of earlier small scale wind tunnel studies on flat panel signs provide an upper bound to the full scale results obtained in their study. The study by Zuo et al. (2014) investigated wind load effects on thirty nine 1:50 scale rectangular box shapes with various geometric configurations in the Texas Tech University wind tunnel. A scaled model of the full size sign used in the Smith et al. study was also tested to validate the wind tunnel results. The effect of depth ratio was not investigated even though the researchers acknowledged that the depth of the model was expected to affect the wind loading. It was evident from the data that the mean force coefficients for the rectangular box models were consistently lower than those obtained for flat panel signs with the same aspect and clearance ratio. This finding was attributed to partial reattachment of flow as reported by Laneville et al. (1975). The dependency of the force coefficient on aspect ratio was also evaluated and shown to increase with increasing aspect ratio when the clearance ratio is smaller than 0.7. Results for the mean eccentricity ratio were also significantly smaller than comparable results for flat panel sign models.

2.1.2   Corner modification

The aerodynamics of bluff bodies like VMS depends largely on the behavior of the separated shear layers. As a result, forces due to wind loading on these structures can be reduced by controlling the separated flow around the structure. Several research studies have investigated the effects of modified corners on drag. Following is a summary and discussion of three key research studies that focused on the aerodynamic effects of rounded and chamfered corners.

Tamura and Miyagi (1999) conducted wind tunnel tests on 2D and 3D square cylinders each with sharp, chamfered or rounded corners in smooth and turbulent flows. Two dimensional flow characteristics were maintained by using end plates above and below the model. The same model was used in three dimensional tests with only the top plate removed. The Reynolds number for the test setup was 3×10^4 based on a length dimension of 50 mm and the longitudinal turbulence intensities were 6.5% and 14%. Their results for cylinders with sharp corners indicated that the drag coefficient decreases as turbulence intensity increases. The research also showed that the value of the drag coefficient was affected by corner modification and found to decrease for both uniform and turbulent flows. The largest decrease in the drag coefficient was obtained for cylinders with rounded corners but a reduction was also noted for cylinders with chamfered corners. Tests on 2D and 3D models with all corner configurations quantitatively indicated that value of the drag coefficient for 3D cylinders is smaller and varies less with vertical angle of attack than 2D

cylinders. A plot of Tamura and Miyagi (1999) lift coefficient (C_L) data in turbulent flow indicates a negative slope for square cylinders with sharp and chamfered corners at a vertical attack angle of 0°. The researchers suggests this is an indication of complete separation of flow in the wake region. However, the slope is positive for cylinders with rounded corners which they suggest indicates a separation of flow followed by reattachment. Tamura and Miyagi (1999) concluded that corner modification decreases the wake width and promotes reattachment resulting in reduced drag forces.

Yamagishi et al. (2010) also examined the flow characteristics around cylinders with modified corners. They conducted wind tunnel experiments, numerical analysis, and applied visualization techniques on square cylinders with various chamfer dimensions. The cylinder cross section dimensions (*d* x *d*) used in the wind tunnel experiments were 30 x 30 mm and 420 mm in length. Chamfers were cut along each edge of the cylinder. Three models were configured for the tests, C1, C3, and C5 with chamfer sizes of C = 1 mm, 3 mm, and 5 mm which corresponded to *C/d* = 0.033, 0.100 and 0.167 respectively. Turbulence intensity for the wind tunnel flow was 0.65% with a maximum wind speed of approximately 35 m/s. This corresponded to test Reynolds numbers ranging from 1×10^3 to 6×10^4. Numerical analysis was performed using Fluent 6.3 utilizing the finite volume method. Wind tunnel tests indicated that the drag coefficient remained constant in the tested Reynolds number range for all cylinder configurations. Computational results were in good agreement with the experimental results. Wind tunnel tests for a Reynolds number of 6×10^4 and computational analysis showed that the drag coefficient for the C1 cylinder and the cylinder without chamfers (*C/d* = 0) was approximately equal with a value around 2. However, the drag coefficient dropped abruptly (40%) to approximately 1.2 for C3 (*C/d* = 0.1). It then increased slightly (20%) to approximately 1.5 for C5 (*C/d* = 0.167). Visible flow patterns obtained by Yamagishi et al. (2010) using a propylene glycol mist tracer showed that the separation area of C3 was smaller than the areas for the sharp edge square and C5. They also noted that the tangential velocity of the corner end side of C5 was large compared to C3 which they thought contributed to the enlarged separation area of C5 and increased drag (the drag coefficient for C5 was still smaller than the cylinder with square corners). Visualization techniques also confirmed that the drag coefficient increased as the width of the wake behind the cylinder became larger (Yamagishi et al., 2010).

Larose and D'Auteuil (2008) carried out experiments to study the effect of Reynolds number on chamfered corners for 2D rectangular prisms with depth ratios of 2, 3, and 4. Models were tested in a pressurized wind tunnel to determine the static force coefficients of drag, lift, and pitching moment. The test Reynolds number ranged from 0.15×10^6 to 4×10^6 based on a constant model depth of 76.2 mm. Pitch angles from -2° to 10° were tested for each run of the three depth ratios (2, 3, and 4), three edge configurations (sharp, small chamfer and large chamfer) and two flow conditions (smooth and turbulent). The researchers chose the shapes because they were suspected to have separated flow regions and possible flow reattachment. Results for the sharp edge configuration with a depth ratio of 2 showed a gradual increase in the drag coefficient as the Reynolds number increased from 0.25×10^6 to 1.0×10^6. The lift coefficient remained constant over the same Reynolds number test range. However, the configuration with large chamfers showed a significantly

different trend. The lift coefficient varied with Reynolds number, even having a sign reversal when the Reynolds number was increased from 0.4 x 10^6 to 1.0 x 10^6, while the drag coefficient remained invariant over the same Reynolds number test range. Larose and D'Auteuil (2008) noted that this difference in results for sharp edges and large chamfers demonstrated the sensitivity of edge configuration to Reynolds number for the specified test conditions.

It should be noted that in tall building design, corner geometry changes have played an important role in reducing wind loads. For example, corner refinements on the 509 m tall Taipei 101 building led to a 25% reduction in the wind-induced base moments (Irwin, 2008).

2.2 Aeroelastic instability

2.2.1 Vortex shedding

Vortex shedding occurs during steady uniform flow when alternating vortices are periodically shed into the wake of a structure. The alternating pattern of vortices is commonly referred to as von Kármán vortex street. The frequency at which the vortices are shed (f_s) is proportional to the approaching mean wind speed ($\overline{U}$) and inversely proportional to the height (c) of the structure. This is expressed non-dimensionally as the Strouhal number

$$S_t = \frac{f_s c}{\overline{U}}$$ (2-1)

The Strouhal number for a circular cross section depends on the Reynolds number of the oncoming flow but for sharp edged cross sections like VMS, where flow separation occurs at the leading edge, the Reynolds number effects are not expected to be significant. However, the Strouhal number for sharp edged rectangular cross sections has been shown to be a function of the depth ratio (Taylor et al., 2014; Cao et al., 2014; Liu and Kopp, 2012). A relationship between the Strouhal number and depth ratio for rectangular cross sections was developed by Dyrbye and Hansen (1997). Since VMS are principally rectangular prismatic shapes, their Strouhal number should be in the range of 0.06 to 0.15 (Ginal, 2003).

Parkinson (1989) compiled results from Brooks (1960), Hoerner (1965), Nakamura and Tomonari (1977), and Washizu et al. (1978) and showed how the Strouhal number is affected by the depth ratio. For smooth flow and a depth ratio in the range of $0 < d/c < 1.0$, the base pressure changes abruptly with increasing d while the Strouhal number only changes slightly. An explanation for this is provided by Bearman and Trueman (1972). If d is small enough, the downstream edges of the afterbody will not interfere with the inward curvature of the streamlines and full strength vortices will form closer to the rear of the cylinder. This lack of interference with the shear layers is why the Strouhal number is not significantly affected. When d is sufficiently large, the downstream edges of the afterbody

will begin to interfere with the inward curvature of the streamlines forcing the vortices to form further downstream and the shear layers to be more diffused. This results in a smaller vortex shedding frequency and a drop in the Strouhal number (Gerrard, 1966). Reattachment of flow along the sides of the afterbody results in an increase in base pressure and a sharp increase in the Strouhal number. The abrupt change arises due to the decrease in lateral spacing of the shear layers after separating from the downstream corners. Smaller lateral spacing of the shear layers corresponds to a smaller streamwise spacing of vortices and therefore a larger vortex shedding frequency (Parkinson, 1989).

The alternating shedding of vortices produce periodic forces that result in oscillations in a plane normal to the direction of wind flow. Significant oscillation can occur when the frequency of vortex shedding is close to the natural frequency of a flexible structure. These lateral vibrations have a strong organizing effect on the vortex shedding pattern which can increase the strength of the vortices and couple the vortex shedding frequency to the natural frequency of the structure. This phenomenon is known as lock-in. The critical wind speed (U_{cr}) at which lock-in occurs can be estimated using the Strouhal number relation

$$U_{cr} = \frac{f_n c}{S_t}$$

(2-2)

where in this case f_n is the natural frequency of the structure. The amplitude of the vibrations resulting from lock-in is limited by the balance between the energy input into the motion by the vortices and the dissipation of that energy by structural damping. Eventually large oscillations of the structure interfere with the uniform shedding of vortices and therefore the maximum amplitude of vortex induced vibrations may be self-limiting (Blevins, 1977). The drag force on a structure vibrating at or near the vortex shedding frequency is also a function of vibration amplitude. Bearman and Obasaju (1982) showed that drag on a square structure increases at resonance.

The range of wind speeds at which vortex shedding can occur is bounded by the ability of the vortices to stay locked onto the structural motion. According to the commentary in the AASHTO Specification (2009), vortices shed at wind velocities below approximately 5 m/s do not possess sufficient energy to excite most sign support structures and at wind speeds greater than about 20 m/s the natural turbulence in the flow disturbs the formation of vortices. This would imply VMS structures are susceptible to vortex induced vibrations only for the range of wind speeds between 5 m/s and 20 m/s. In fact there is little evidence that the turbulence intensity increases with wind speed. Therefore vortex excitation at speeds above 20 m/s cannot be discounted.

15

2.2.2 Galloping

Galloping of a prismatic structure is the self-excited response to natural wind due to the aeroelastic instability of the structure. Galloping is typically characterized by predominately horizontal wind flow and vertical motion of the structure. To initiate galloping there must be an initial displacement of the structure that changes the angle of attack (α) of the wind flow relative to the structure. The initial displacement may be due to fluctuations in the wind or vortex shedding. The vertical velocity ($\dot{z}$) of the structure results in the angle of attack of the wind being

$$\alpha = arctan\left(\frac{\dot{z}}{\bar{U}}\right) \tag{2-3}$$

where $\bar{U}$ is the horizontal velocity of the oncoming wind. For $\dot{z} \ll \bar{U}$ this becomes

$$\alpha = -\left(\frac{\dot{z}}{\bar{U}}\right) \tag{2-4}$$

Let C_L denote the lift coefficient, α the angle of attack, and C_D the drag coefficient. The equations of motion of the body yield the *necessary* condition for incipient galloping motion, known as the Den Hartog criterion:

$$\left[\frac{dC_L}{d\alpha} + C_D\right]_{\alpha=0} < 0 \tag{2-5}$$

where the left-hand side of Eq. 2-5 is evaluated at $\alpha = 0$. A small vertical motion of the structure results in a force given by

$$F_z = -\frac{1}{2}\rho\bar{U}\dot{z}A\left(\frac{dC_L}{d\alpha} + C_D\right)_{\alpha=0} \tag{2-6}$$

The force is in the same direction as the body velocity $\dot{z}$ if $dC_L/d\alpha + C_D < 0$ and is proportional to that velocity. Therefore it is effectively a negative aerodynamic damping force. The sufficient condition for incipient galloping motion is that this force exceed the positive damping force due to the mechanical damping. It follows from this condition that the minimum wind speed required to initiate galloping is proportional to the mechanical damping of the structure (Novak, 1972).

Parkinson (1963) explained that flow reattachment will occur along a side of a prismatic shape for sufficiently large values of α. The galloping characteristics of the

structure will be affected by the resulting asymmetry in the pressure distribution which produces a net force in the vertical direction. Parkinson (1989), using data from Brooks (1960), Smith (1962), Laneville (1973), Novak (1974), and Nakamura and Tomonari (1977), showed that rectangular cylinders with $d/c < 0.75$ in smooth flow did not gallop from rest (hard galloping) and required an initial vibration. Sections in the range $0.75 < d/c < 3.0$ did gallop spontaneously from rest (soft galloping). The lower boundary for the beginning of soft galloping corresponds to the abrupt change in base pressure noted previously when the trailing edges of the afterbody begin to interfere with the inward curvature of the streamlines. For $d/c > 3.0$ no galloping could be induced. This upper boundary corresponds to an afterbody length that is sufficiently long for reattachment of the shear layer to occur. Parkinson (1989) also demonstrated that as turbulence in the oncoming flow is increased, soft galloping sections experience weaker galloping and eventually become stable and hard galloping sections become soft galloping.

Kaczinski et al. (1998) had difficultly reproducing galloping results in wind tunnel experiments. A model observed to gallop in one test did not gallop in another test under identical test conditions. The same unpredictability has been observed in the field. Only one structure experienced galloping in a series of structures subjected to the same wind conditions. The researchers attributed the difficulty in reproducing galloping results in the laboratory and the unpredictability observed in the field to the sensitivity of these structures to very specific conditions such as the dynamic properties of the structure, aerodynamic properties of the attachments, and flow characteristics (Kaczinski et al., 1998). In-service VMS attached to cantilever support structures with fundamental frequency of $1.04 - 1.10$ Hz and mechanical damping ratio of $0.4 - 0.7\%$ have been observed galloping, indicating that the flow velocity was high enough to induce the aerodynamic damping ratio required for galloping to occur. Structural failure due to galloping was documented for a bent monopole structure in California in 1995. Instrumentation and monitoring of this structure showed that it was galloping in steady winds (Dexter and Ricker, 2002). The susceptibility of non-cantilever (i.e. bridge-type) VMS support structures to galloping is still unclear. Dexter and Ricker (2002) did not expect VMS mounted on non-cantilever structures to be susceptible to galloping "due to the rigidity of the sign bridge." Fouad et al. (2003) points out that the question of susceptibility of non-cantilever support structures to galloping (and vortex shedding) is unresolved and additional laboratory testing and field evaluation is necessary. However, Fouad et al. (2003) did not specifically address VMS.

Ginal (2003) evaluated the galloping instability of two non-cantilever four chord VMS support structures in Wisconsin. Each structure supported a VMS with dimensions corresponding to geometric ratios of $b/c \approx 3$ and $d/c \approx 0.5$. A modal analysis using FEM was performed and the onset wind velocities were determined using the universal galloping response curves for rectangular prisms developed by Novak and Tanaka (1974). Based on calculations and assumptions by Ginal (2003), the onset wind velocities for the two structures were greater than 98 m/s. Given these high velocities, Ginal (2003) concluded that galloping vibrations do not need to be considered as a loading scenario for the non-cantilevered VMS support structure as configured in his test group. He adds, however, that since galloping of sign support structures is highly dependent on the characteristics of the

structure including cross section, total damping ratio, and natural frequencies as well as flow characteristics, a wind tunnel study should be conducted to validate the results of his research.

3 EXPERIMENTAL DESIGN, PROCEDURE, AND INSTRUMENTATION

3.1 Industry specifications and model size selection

The experimental design was initiated by contacting major manufacturers of VMS. Three manufacturers Daktronic, Ledstar, and Skyline provided design specifications and typical sign dimensions. The aspect ratio (b/c) and depth ratio (d/c) for each sign configuration was calculated and plotted in Figure 3.1. Prototype aspect ratios ranged from 0.62 to 9.81 and depth ratios range from 0.11 to 0.91. Three aspect ratios ($b/c = 1$, 3 and 5) and three depth ratios ($d/c = 0.1$, 0.4 and 0.7) were selected to encompass a wide range of typical VMS sizes and shapes. The ranges of selected ratios covered in this study are delineated by the red rectangle in Figure 3.1. The selected geometries represent approximately 89% of the aspect ratios and 98% of the depth ratios provided. A fixed clearance ratio of $c/h = 0.24$ was used for all tests. This value is based on a full scale sign height of 1.8 m and a minimum vertical clearance of 6 m which corresponds to a full scale minimum mounting height of 6.9 m. A length scale of 1:3 was utilized to minimize blockage effects and ensure that the largest model was completely immersed in the FIU WOW wind field.
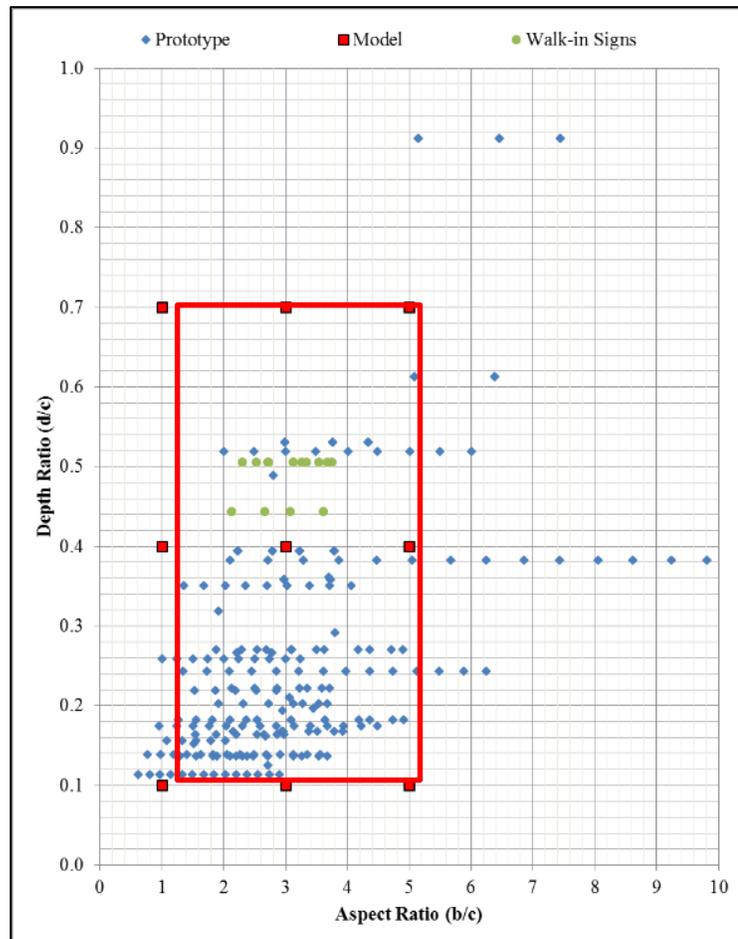
Figure 3.1 Prototype geometric ratios

3.2 Model design

A total of 13 models were constructed for testing. Models 1 - 9 have sharp edges and vary in length from 0.6 m to 3 m with depths varying from 61 mm to 427 mm. Model 10 was constructed with 32 mm round edges and Model 11 was constructed with 32 mm chamfered edges. Models 12 and 13 are flat panels consisting of a single sheet of plywood with a depth dimension of approximately 13 mm. Scaled dimensions of the models and applicable geometric ratios are included in Table 3.1.

Table 3.1 Model dimensions and geometric ratios

Model No.	Width b (m)	Height c (m)	Depth d (m)	Aspect Ratio b/c	Depth Ratio d/c
1	0.6	0.6	0.06	1	0.1
2	1.8	0.6	0.06	3	0.1
3	3.0	0.6	0.06	5	0.1
4	0.6	0.6	0.2	1	0.4
5	1.8	0.6	0.2	3	0.4
6	3.0	0.6	0.2	5	0.4
7	0.6	0.6	0.4	1	0.7
8	1.8	0.6	0.4	3	0.7
9	3.0	0.6	0.4	5	0.7
10	3.0	0.6	0.4	5	0.7
11	3.0	0.6	0.4	5	0.7
12	3.0	0.6	0.013	5	0.021
13	1.5	0.3	0.013	5	0.042

The models were fabricated from 13 mm shop grade maple plywood and reinforced with 51 x 102 mm southern pine. Models 4-11 were fitted with removable top panels to facilitate connection to the support structure and Models 1-3 and 12-13 were through bolted to the support structure with threaded 13 mm countersunk bolts. All wood to wood connections were joined with 25 mm screws and structural wood glue.

The model support structure consisted of either a single or double rigid steel cantilever system. Major components and dimensions of the support system are illustrated in Figure 3.2. The single support system was used for the $b = 0.6$ m models (Models 1, 4, and 7) and the double support system was used for the $b = 1.8$ m and $b = 3.0$ m models (Models 2-3, 5-6, and 8-13). The horizontal cantilever arm for both the single and double support systems was 762 mm long and fabricated from 152 x 152 x 6 mm steel tubes. A vertical 305 x 305 x 6 mm steel plate was welded to the front end of the cantilever arm to provide a mounting point for the models. A second horizontal 305 x 305 x 6 mm steel plate was welded to the rear end of the cantilever arm which was then attached to the top plate of the

load cell with four 13 mm lag bolts. The vertical supports were also fabricated from 152 x 152 x 6 mm steel tubes. A 305 x 305 x 6 mm steel plate was welded to the top of each vertical support which was then connected to the bottom plate of the load cell with four lag bolts. The vertical posts of the double support system were spaced 1.2 m apart. Each vertical support was bolted to the base with four 13 mm bolts and then rigidly connected to the WOW floor with 19 mm bolts. A total of three complete support systems were required and assembled for testing.
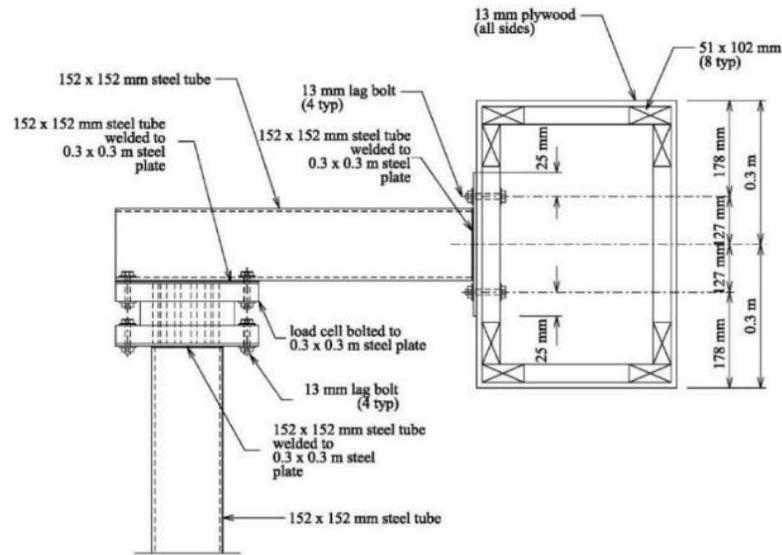
Figure 3.2 Major components of the cantilever support system

All models were mounted at mid height, 2.3 m above the WOW test facility floor, and attached to the cantilever arm steel connection plate with four 13 mm bolts centered horizontally and vertically on the model. The bolt holes (14 mm) in the back face of the models were drilled slightly larger than the 13 mm bolt. This was done to accommodate any minor misalignments in the support structure that might induce initial stresses in the setup. Additional stability was provided by three wire cables attached to eye bolts at the top of each vertical support (below the load cells) and fixed to the WOW floor.

3.3   Instrumentation

A multi-axis load cell supplied by JR3, Inc. (model 75E20S4 – M125D – AF 1350L) was mounted on top of each vertical support to simultaneously measure forces, moments and torques. A picture of the load cell is shown in Figure 3.3a. The load cells are equipped with six degree of freedom force torque sensors which simultaneously measure forces along three orthogonal axes (x, y, and z) and moments and torques about those axes. The load cells are oriented with the x- and y- axes at the horizontal mid-plane of the load cell and the z axis along the central vertical axis. The load cells used in this study were oriented with respect to the VMS model axes and positioned with the positive x axis in the along wind direction, the positive y axis to the right, and the positive z axis up. Refer to Figure

21

1.5 for axis and force orientation. Measured forces and moments were multiplied by the manufacturer's calibration matrix to obtain actual forces and moments (the calibration matrices are included in Appendix A). A total of three load cells were assembled and wired in accordance with the manufacturer's specifications.

Figure 3.3 Instrumentation (a) JR3 load cell (b) Turbulent Flow Instruments cobra probe

Cobra probes supplied by Turbulent Flow Instruments (Figure 3.3b) were used to measure the wind velocity and turbulence in three orthogonal directions. Probes were mounted vertically 0.9 m above the model at an elevation of 3.5 m above the WOW floor. This distance was considered sufficient to ensure that the cobra probe wind speed readings were not affected by the flow around the model (this is discussed in more detail in Section 3.6). Each probe was mounted on a vertical uni-strut support suspended from the fixed gantry. Three probes spaced at 1.2 m on center were utilized with the middle probe centered horizontally on the model. Figure 3.4 shows the configuration of the cobra probes with a model in place. In addition, wind speed measurements were also conducted for the free flow case where the speeds were measured without the model in place at the mid-height of the model (refer to Section 3.6.3).
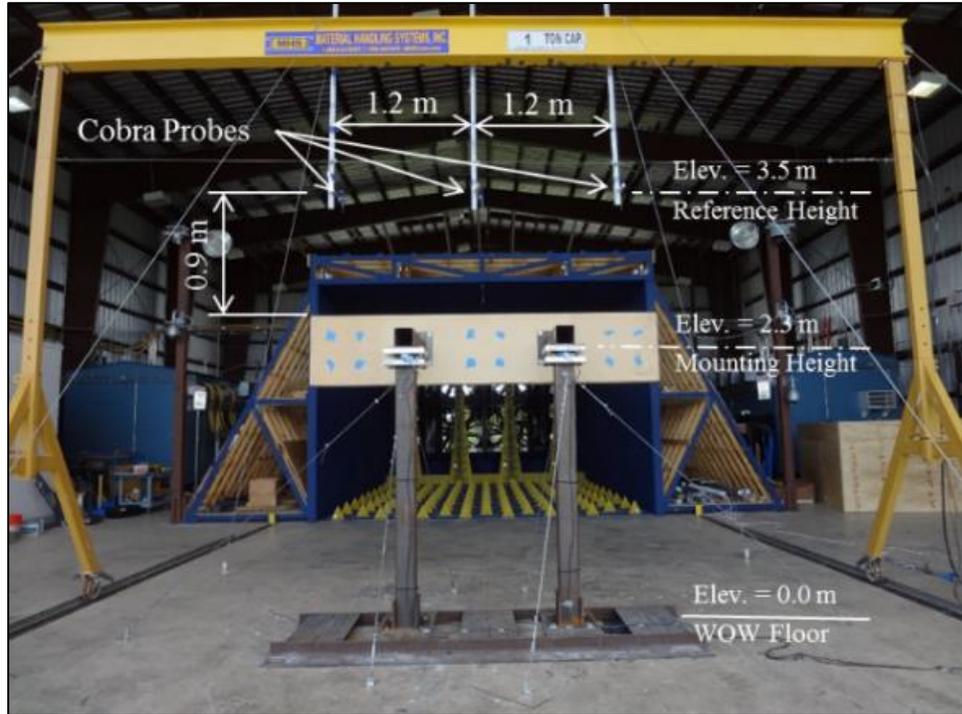
Figure 3.4 Cobra probe configuration (a) looking upstream (b) side elevation

3.4 Wall of Wind (WOW)

Experiments were conducted in the Wall of Wind (WOW) facility at Florida International University (FIU). The test section of this open jet system is 6.1 m wide x 4.3 m high and wind is generated by two rows of six electric fans arranged in a convex arc (Figure 3.5). Each fan has a maximum flow rate of 113.3 cubic m/s and the rotational speed is controlled by variable frequency drives (VFD). The wind flow from each fan merges into a contraction zone which is designed to generate a high velocity uniform flow field. Vertical vanes at the contraction exit guide the flow in the longitudinal direction. A 9.8 m flow simulation box consisting of triangular spires and floor roughness elements help develop the desired atmospheric boundary layer (ABL) profile.

Figure 3.5 Wall of Wind (WOW)

3.4.1 Test wind speeds

Measurements were conducted for several throttle percentages which represent the percentage of fan motor speed and correspond to a test wind speed. A summary of test throttle percentages and corresponding measured mean wind speeds for the probes at a height of 2.3 m and 3.5 m (without a model in place) is given in Table 3.2. The measured mean wind velocities used in this study at the mounting height of the models (2.3 m) were approximately 15 m/s (25% throttle) and 40 m/s (65% throttle).

Table 3.2 Free flow wind speeds at 2.3 m and 3.5 m

| Throttle | Mean Free Flow Wind Speed | |
| | at 2.3 m | at 3.5 m |
	(m/s)	(m/s)
20%	12	13
25%	15	17
30%	18	20
40%	24	27
50%	30	33
60%	37	40
65%	40	44
70%	43	47
80%	49	54
90%	55	60
100%	61	67

3.4.2 Partial turbulence simulation

Tests were conducted using 1:3 scale models in a simulated suburban atmospheric boundary layer. The turbulence intensity at the model mounting height of 2.3 m was approximately $I_u \approx 8\%$. The turbulence intensity of the WOW laboratory flow is lower than the full-scale target suburban terrain ABL. This is due to the partial turbulence simulation method that is utilized in the WOW which reproduces only the high frequency portion of the ABL spectrum (see Yeo and Gan Chowdhury, 2013 and Fu, 2013). The partial simulation flow in the WOW and the full-scale suburban ABL flow have similar high frequency spectral content but the partial spectrum flow in the WOW is characterized by significantly weaker low frequency fluctuations.

The partial turbulence simulation utilized in the WOW is governed by the following formula provided by Irwin (1998)

$$\frac{I_{um}}{I_{up}} = \left(\frac{^xL_{um}}{^xL_{up}}\right)^{\frac{1}{3}} \left(\frac{b_p}{b_m}\right)^{\frac{1}{3}}$$

(3-1)

where I_u is the turbulence intensity, L_u is the integral length scale and b is the reference length. The subscripts m and p denote model and prototype respectively.

The missing low frequency content of the WOW spectrum represents the large scale turbulence associated with slowly moving gusts. This large scale turbulence does not significantly affect local vortex formation, flow separation, or flow reattachment. However, the proper simulation of small-scale or high frequency turbulence is critical in the investigation of aerodynamic parameters and flow separation from sharp edged objects like VMS. It was shown by Fu et al. (2012) that two flows with approximately similar high-frequency spectral content will produce comparable aerodynamic effects even though one flow is characterized by weak low frequency fluctuations. More information about the partial turbulence simulation used in the WOW and the validation of aerodynamic results can be found in Irwin (1998), Fu et al. (2012), Yeo and Gan Chowdhury (2013), and Fu (2013).

3.5   Tare tests

Tare tests were conducted to isolate and correct for the secondary aerodynamic forces applied to the support system. Two configurations, Setup A and B were utilized and shown schematically in Figures 3.6a and 3.6b respectively. Setup A was used to determine the tare correction for the single support configuration. This setup consisted of independently supporting Model 7 25 mm in front of Vertical Support 1. The model was held in place by mounting Support 2 to the front face of the model. Wire cables were attached to each vertical support to provide additional stability. Load cells were mounted and wired on both Support 1 and 2 but only data from Load Cell 1 was utilized. The positive x-axis for Load Cell 1 was oriented to correspond with the longitudinal along-wind direction. Setup B was used to determine the tare correction for the double support configuration. This setup consisted of detaching Model 8 from the horizontal cantilever arm and independently supporting it 25mm in front of Vertical Support 1. The position of Support 1 corresponded to the same location of the support during the force coefficient testing and the leading windward support for the 45° tests. The model was held in place by rotating Supports 2 and 3 ninety degrees and attaching them to each end of the model. This preserved the flow pattern around the model and isolated the aerodynamic forces applied to the support structure. Wire cables were attached to each vertical support to provide additional stability. Load cells were mounted on all three supports but only data from Load Cell 1 was utilized. The positive x-axis for Load Cell 1 was oriented to correspond with the longitudinal along-wind direction. Figure 3.7a shows a picture of tare test Setup A configured for the 0° horizontal wind approach direction and Figure 3.7b is a picture of tare test Setup A configured for the 45° horizontal wind approach direction. Similarly, Figure 3.8a shows a picture of tare test Setup B configured for the 0° horizontal wind approach and Figure 3.8b is a picture of tare test Setup B configured for the 45° horizontal wind approach.
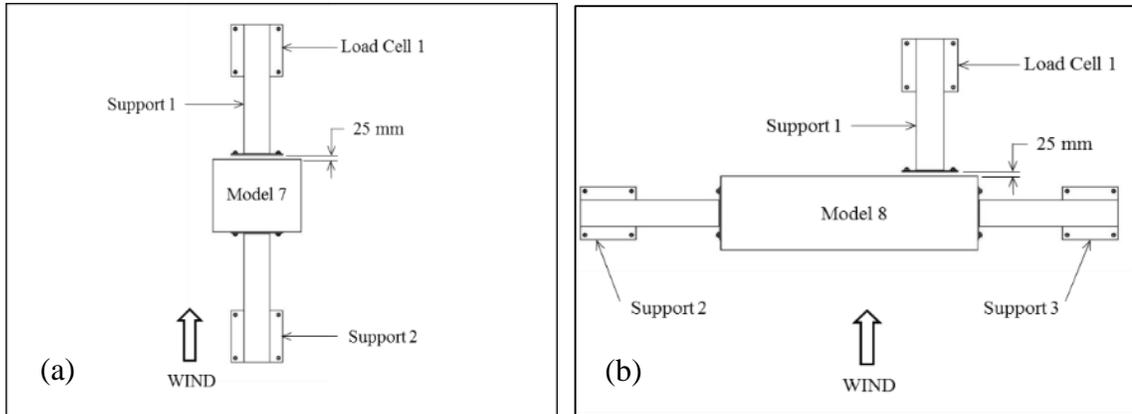
Figure 3.6 Tare test schematics (a) Setup A – single support (Models 1, 4, and 7) (b) Setup B – double support (Models 2, 3, 5, 6, and 8-13)

Figure 3.7 Tare test Setup A in the WOW (a) 0° configuration (b) 45° configuration

Figure 3.8 Tare test Setup B in the WOW (a) 0° configuration (b) 45° configuration

Tare test data was sampled at 100 Hz for 1 minute. Both setups were tested for horizontal wind approach directions of 0° and 45°. Setups A and B were rotated clockwise for the 45° horizontal wind approach test. For Setup B this ensured that data was measured on the windward load cell (Load Cell 1). Baseline data sampled one minute before and one minute after each test run was subtracted from the measured test data to account for zero offset effects. Tare tests were conducted for wind speeds of 12 m/s, 15 m/s, 30 m/s, and 40 m/s.

The measured tare correction for Setup A was applied to Models 1, 4, and 7 and the tare correction obtained using Setup B was applied to Models 2-3, 5-6, and 8-13. A summary of tare test results for the single support (Setup A) configuration is included in Table 3.3 and a summary of results for the double support (Setup B) configuration is included in Table 3.4.

Table 3.3 Summary of tare test results – single support (Model 7)

0°

Wind Speed	Forces (N)			Moments (N-m)		
	$F_{x\,1}$	$F_{y\,1}$	$F_{z\,1}$	$M_{x\,1}$	$M_{y\,1}$	$M_{z\,1}$
12 m/s	-0.24	0.14	1.46	-0.02	-0.06	-0.01
15 m/s	-0.59	0.12	1.06	-0.01	-0.10	0.00
30 m/s	-3.69	0.95	1.98	0.08	-0.40	0.00
40 m/s	-6.86	1.77	4.68	0.16	-0.65	-0.09

45°

Wind Speed	Forces (N)			Moments (N-m)		
	$F_{x\,1}$	$F_{y\,1}$	$F_{z\,1}$	$M_{x\,1}$	$M_{y\,1}$	$M_{z\,1}$
12 m/s	1.62	-8.00	15.07	-1.05	-0.29	-0.56
15 m/s	1.25	-12.95	10.40	-1.66	-0.48	-0.79
30 m/s	0.80	-51.46	24.76	-6.68	-2.24	-3.73
40 m/s	1.67	-85.64	38.43	-11.05	-3.92	-6.52

Table 3.4 Summary of tare test results – double support (Model 8)

0°

Wind Speed	Forces (N)			Moments (N-m)		
	$F_{x\,1}$	$F_{y\,1}$	$F_{z\,1}$	$M_{x\,1}$	$M_{y\,1}$	$M_{z\,1}$
12 m/s	0.25	-0.02	10.99	-0.02	0.16	0.30
15 m/s	-0.16	0.22	6.64	0.03	0.21	0.56
30 m/s	-4.84	2.03	2.25	0.37	0.67	2.31
40 m/s	-9.86	3.97	-7.14	0.79	0.96	4.05

45°

Wind Speed	Forces (N)			Moments (N-m)		
	$F_{x\,1}$	$F_{y\,1}$	$F_{z\,1}$	$M_{x\,1}$	$M_{y\,1}$	$M_{z\,1}$
12 m/s	-2.21	-8.65	2.45	-0.97	0.17	-1.07
15 m/s	-4.10	-13.22	2.16	-1.48	0.33	-1.61
30 m/s	-20.13	-49.23	11.01	-5.45	2.19	-5.71
40 m/s	-36.43	-79.37	21.35	-8.62	4.79	-9.33

3.6   Wind-field adjustments

The presence of the model has two effects on the wind field: (1) local flow field distortion and (2) blockage. Local flow field distortion is caused by accelerations and decelerations in the flow field very close to the model as the air negotiates its way around the VMS. These effects attenuate as you move upwards or downwards away from the model so ideally speed measurements should be taken far enough away to be out of this zone. The second effect due to the presence of the model is blockage of the whole flow field. This is the difference between the model being in an infinitely large wind field (as in real wind) and being in a 6.1 x 4.3 m jet near the mouth of the flow simulation box. The general flow at the model could either experience an overall acceleration or deceleration depending on whether the constraint of the simulation box dominated over the lack of constraint of the jet or vice versa. A blockage test was performed to get an overall measure of whether the wind speed measurements were sampled sufficiently far enough away and to correct for local flow effects.

3.6.1   Blockage correction test

The blockage test consisted of testing Model 12 with dimensions of 3.0 x 0.6 m at a wind speed of 19 m/s and Model 13 (1.5 x 0.3 m) which was 1/4 blockage, at twice the wind speed at 38 m/s. Both models were flat panels ($d = 13$ mm) with $b/c = 5$. Pictures of the blockage test setup for Models 12 and 13 in the WOW are shown in Figure 3.9.

Figure 3.9 Blockage test setup in the WOW (a) 0° configuration (b) 45° configuration

The blockage test was conducted for 0° and 45° horizontal wind approach directions in the simulated suburban boundary layer flow. Data for each test run was sampled at 100 Hz for 1 minute. Baseline data sampled one minute before and one minute after each test run was subtracted from the measured test data to account for zero offset effects. The double cantilever support was used for the blockage test and the applicable tare correction was applied to the measured blockage test data for the 0° horizontal wind approach. Tare corrections were derived from testing large prismatic models (Models 7 and 8) which were not representative of the models used in the blockage tests. Therefore, no tare correction was applied to the measured blockage test data for the 45° horizontal wind approach direction.

The measured wind speed at the reference height of 3.5 m was intended to be far enough away from the model to avoid the local flow effects. However, testing revealed that the measurements may not have been completely free of local effects. Tests using Model 12 (1:3 scale) showed that the model was probably still in a slightly accelerated local flow. This caused the drag coefficient results to be slightly low. For Model 13 at half the scale (1:6), the flows were less affected which resulted in larger drag coefficients. To account for this effect, the zero blockage correction was extrapolated from the plot of the normal force coefficient (C_{Fx}) versus the ratio of the model area to the wind field area (A/As) as shown in Figure 3.10 for the 0° horizontal wind direction. Where A is the area of the front face of the model (b x c) and As is the area of the WOW wind field equal to 26 m^2. As shown in the graph, a negative blockage effect was observed (the net effect was to reduce the drag compared to the zero blockage case). The zero blockage drag coefficient extrapolated from the graph for Model 12 (0° horizontal wind direction) was 1.04. A summary of the 0° blockage correction percentage used for each model is shown in Table 3.5. The graph for the 45° horizontal wind direction is shown in Figure 3.11. The zero blockage drag coefficient extrapolated from the graph for Model 12 for the 45° direction was 0.86. The percent blockage correction applied to each model was then calculated as a proportion of A/As. A summary of the 45° blockage correction percentage used for each model is shown in Table 3.6.
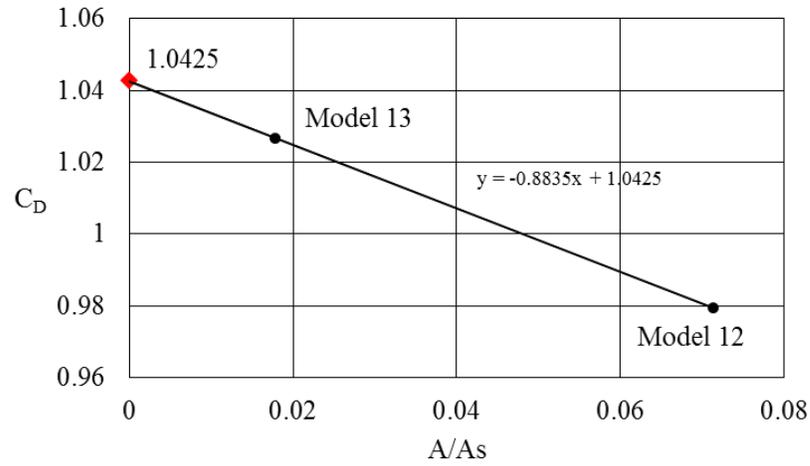
Figure 3.10 Blockage correction graph - 0° wind direction

Table 3.5 Blockage correction results - 0° wind direction

Model	Blockage Correction
1, 4, and 7	1.3%
2, 5, and 8	3.9%
3, 6, and 9	6.4%
10 and 11	6.4%
12	6.4%
13	1.6%
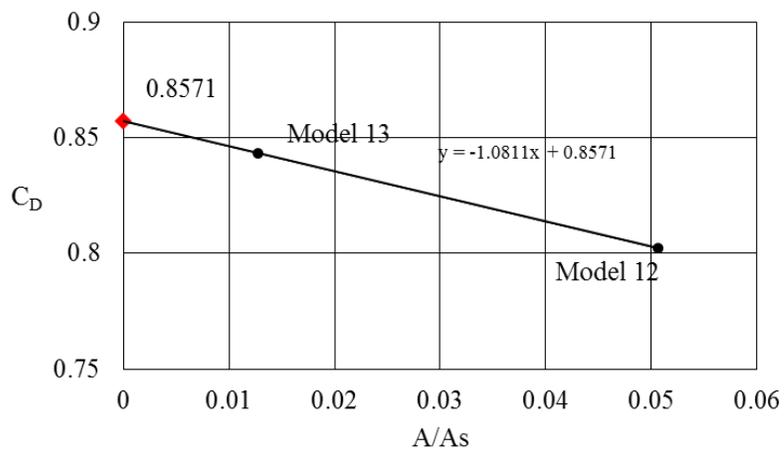
Figure 3.11 Blockage correction graph - 45° wind direction

Table 3.6 Blockage correction results - 45º wind direction

Model	Blockage Correction
1	1.50%
2	4.22%
3	6.94%
4	1.91%
5	4.63%
6	7.35%
7	2.31%
8	5.04%
9, 10, 11	7.76%
12	6.84%
13	1.72%

3.6.2   Wind speed spatial relationship

The mean wind speed ($\overline{U}$) used in the calculation of the drag coefficient was determined by averaging the mean temporal wind speeds measured at different locations during model testing. Wind speed measurements were recorded during each test run using three cobra probes mounted at the reference height of 3.5 m which was 0.9 m above the model. The probes were spaced horizontally 1.2 m apart with the middle probe centered with respect to the model (see Figure 3.4). The mean temporal wind speed for the one minute test length was determined for each probe. The measured mean wind speeds at 3.5 m (with the model in place) are provided in Table 3.7. Analysis of the mean temporal wind speeds for each probe showed that the wind profile along the horizontal length of the model was not quite uniform. The measured wind speed at the center probe was approximately 4% higher than the wind speeds measured at each of the two outer probes for the 0° horizontal wind direction and 5% higher for the 45° wind direction. The percent difference between the mean measured wind speed at 3.5 m and the mean adjusted spatial wind speed for each model test is shown in Table 3.8. Consequently, a linear interpolation was applied to calculate the wind speed at a horizontal location corresponding to the outer edge of each model. These three spatial wind speeds (left edge, center, and right edge) were averaged to determine the mean spatial wind speed at the reference height of 3.5 m. This is the wind speed used in the force coefficient calculation. A summary of the calculated spatial wind speeds at the reference height of 3.5 m for each model tested is provided in Table 3.9.

Table 3.7 Mean wind speeds at 3.5 m

Model No.	Measured Mean Wind Speed (m/s)			
	0° Wind Direction		45° Wind Direction	
	25% Throttle	65% Throttle	25% Throttle	65% Throttle
1	18	48	18	48
2	18	48	15	48
3	18	48	15	48
4	18	48	18	48
5	18	48	15	48
6	18	48	18	48
7	18	48	18	48
8	18	49	18	48
9	19	49	18	48
10	18	49	18	48
11	19	49	18	48

Table 3.8 Percent difference between center and edge probes at 3.5 m

Model No.	% Difference Between Center and Edge Probes			
	0° Wind Direction		45° Wind Direction	
	25% Throttle	65% Throttle	25% Throttle	65% Throttle
1	-5%	-6%	-5%	-5%
2	-2%	-3%		-4%
3	-2%	-2%		-4%
4	-5%	-6%	-5%	-5%
5	-3%	-4%		-4%
6	-2%	-2%	-4%	-5%
7	-5%	-6%	-5%	-6%
8	-4%	-5%	-5%	-7%
9	-2%	-3%	-6%	-6%
10	-4%	-3%	-4%	-5%
11	-4%	-4%	-4%	-5%
Mean	**-3%**	**-4%**	**-5%**	**-5%**

Table 3.9 Spatial wind speeds at 3.5 m

Model No.	Mean Spatial Wind Speed (m/s)			
	0° Wind Direction		45° Wind Direction	
	25% Throttle	65% Throttle	25% Throttle	65% Throttle
1	19	49	19	49
2	18	48	15	48
3	18	47	14	47
4	19	49	19	49
5	18	49	15	48
6	18	48	18	48
7	19	49	19	49
8	19	49	19	48
9	18	49	18	48
10	18	49	18	47
11	18	49	18	47

3.6.3 Free flow wind

Free flow wind speed measurements were conducted to determine the relationship between the wind speeds at the reference height of 3.5 m and the desired wind speeds at the model mounting height of 2.3 m.

The Free Flow Wind Testing used an array of cobra probes mounted on a grid of vertical and horizontal uni-strut supports. Three vertical uni-struts at 1.2 m on center were attached to the fixed gantry at the top and bolted to the WOW floor at the bottom. The gantry was bolted to tracks on the WOW floor at the desired location. Wire cables attached at the top of the gantry and bolted to the WOW floor provided supplemental support and stability to the gantry. Additional uni-strut bracing was provided at the 2/3 point of the uni-strut vertical span. An array of six cobra probes were mounted in two horizontal rows. The top row of three probes was mounted at 3.5 m and spaced horizontally 1.2 m on center with the middle probe centered on the model (however no model was in place). The bottom row of three probes was mounted at 2.3 m. and also spaced horizontal at 1.2 m on center. Looking upstream, the probes on the top row were numbered from right to left 1-3 and the bottom row from right to left were numbered 4-6. Figure 3.12 shows the free flow wind test setup in the WOW and the configuration of the cobra probes. Testing was conducted in the simulated suburban boundary layer flow (power law exponent $\alpha = 0.25$) and data was sampled at 100 Hz for 1 minute. Baseline data sampled one minute before and one minute after each test run was subtracted from the measured test data to account for zero

offset effects. The Free Flow Wind Test was only conducted for the 0° horizontal wind direction. A summary of the measured free flow wind speeds is provided in Table 3.2.
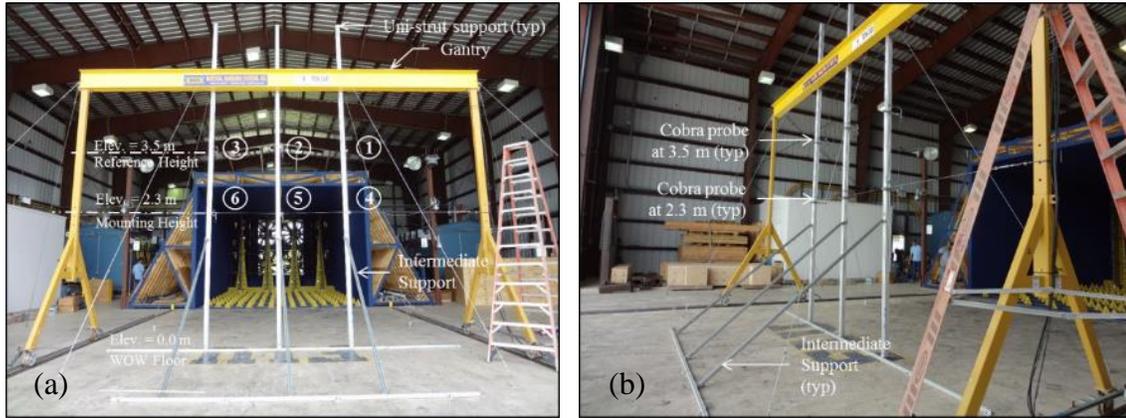
Figure 3.12 Free flow wind test setup in the WOW a) looking upstream b) side view

The ratio of the measured free flow wind speed at 3.5 m to the mean wind speed at 2.3 m was established for each set of corresponding probes. The mean vertical height adjustment (*VHA*) ratio for the 15 m/s and 40 m/s tests was calculated using the mean ratio of Probe 1: Probe 4, Probe 2: Probe 5, and Probe 3: Probe 6. The calculated *VHA* ratios are tabulated in Table 3.10. The measured wind speed used in the drag coefficient calculation was adjusted to the mounting height wind speed by multiplying the calculated drag coefficient at 3.5 m by the mean *VHA* squared for each tested wind speed as follows

$$C_{Fx\_15} \times (VHA_{15})^2 \tag{3-1}$$

$$C_{Fx\_40} \times (VHA_{40})^2 \tag{3-2}$$

where C_{Fx_15} and C_{Fx_40} are the drag coefficients calculated at 3.5 m for the 15 and 40 m/s wind speeds respectively. VHA_{15} and VHA_{40} are the mean vertical height adjustment ratios for the 15 and 40 m/s test wind speeds. The mean *VHA* ratio for the 15 m/s wind speed was determined to be $VHA_{15} = 1.10$ and the mean *VHA* ratio for the 40 m/s wind speed was also determined to be $VHA_{40} = 1.10$.

Table 3.10 Vertical height adjustment (VHA) ratios

Throttle	20%	25%	30%	40%	50%	60%	65%	70%	80%	90%	100%
Wind Speed (m/s)	12	15	18	24	30	37	40	43	49	55	61
Probe 1:Probe 4	1.17	1.13	1.15	1.13	1.13	1.14	1.14	1.14	1.13	1.12	1.12
Probe 2:Probe 5	1.11	1.11	1.11	1.11	1.11	1.11	1.12	1.12	1.11	1.12	1.12
Probe 3:Probe 6	1.07	1.07	1.06	1.06	1.06	1.05	1.05	1.05	1.05	1.04	1.04
Mean Correction	**1.12**	**1.10**	**1.10**	**1.10**	**1.10**	**1.10**	**1.10**	**1.10**	**1.10**	**1.09**	**1.09**

3.7 Test setups and procedures

3.7.1 Force coefficient tests

Models 1-9 were utilized in the force coefficient testing. Testing consisted of 18 model configurations and 36 individual aerodynamic tests (tests configurations are shown in Appendix B). The test assembly began with bolting the steel base to the WOW floor then bolting either the single or double cantilever support system to the base depending on the model size. The single cantilever support system was utilized for models 1, 4 and 7 and the double cantilever support system was utilized for models 2-3, 5-6, and 8-9. The single or double cantilever support system and the base remained in place while the models were interchanged for each test. Baseline data indicated that erection of the model and bolt tightening induced minor stresses in the system. Loosening and then retightening the load cell bolts after mounting the model reduced this effect. Three wire cables bolted to the WOW floor were attached to the top of each vertical support (below the load cell) to provide additional stability and reduce vibration in the system. The wire cables were tightened and adjusted after each model was erected. All models were mounted to the cantilever support at mid height which was 2.3 m measured from the WOW floor. This provided 2 m vertical clearance, except for Model 13 which had a vertical clearance of 2.1 m ($c/h = 0.13$). Based on the model height of 0.6 m, this corresponded to a clearance ratio of $c/h = 0.24$. Typical model setups in the WOW for the 0° and 45° tests are shown in Figures 3.13 and 3.14. As shown in the figures, three cobra probes were mounted at the reference height of 3.5 m which provided 0.9 m of clearance above the top of the model. Each probe was mounted on a uni-strut suspended vertically from the fixed gantry. The probes were spaced horizontally 1.2 m on center with the middle probe centered on the model. A horizontal cable attached to the fixed gantry and the bottom of the uni-struts helped to reduce vibration of the cobra probes.
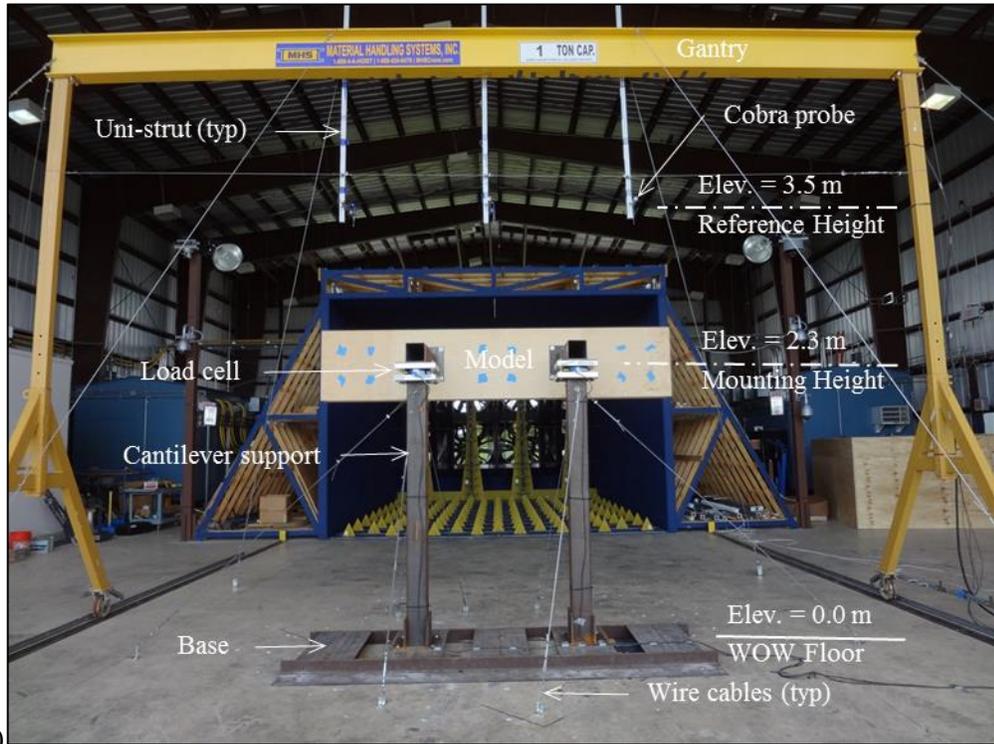
Figure 3.13 Force coefficient test setup in the WOW - 0° wind direction (a) Looking upstream (b) Side view
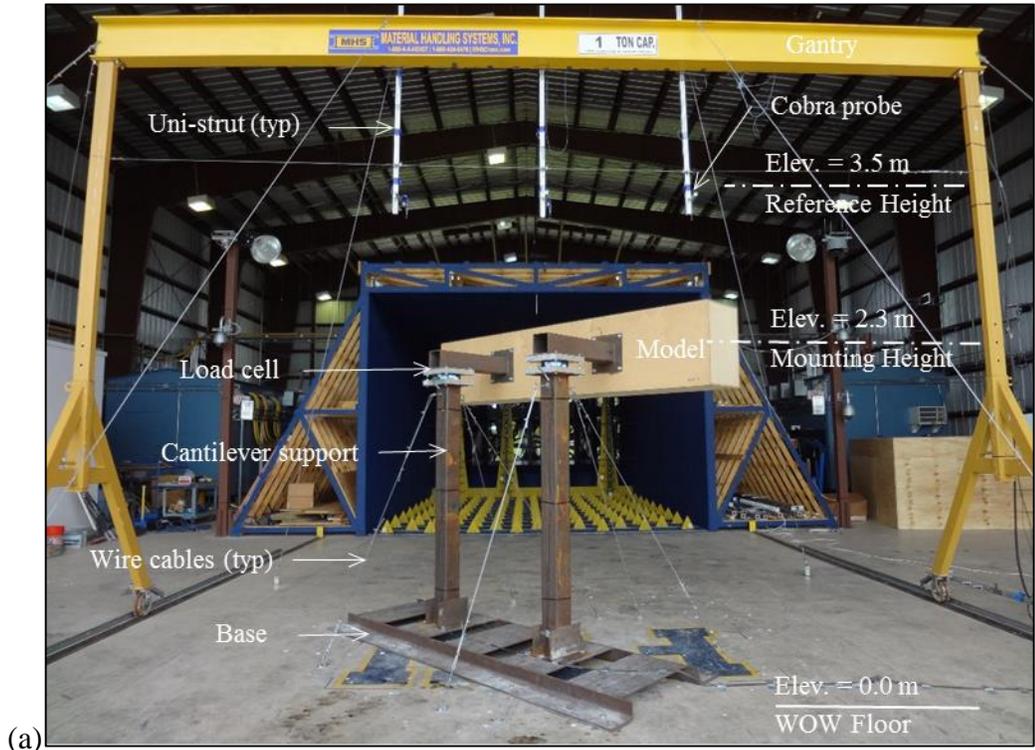
Figure 3.14 Force coefficient test setup in the WOW - 45° wind direction (a) Looking upstream (b) Side view

All models were tested for 0° and 45° horizontal wind directions. Zero degree was defined as the direction of the approaching wind normal to the front face of the model. The base was rotated clockwise about the vertical axis of the model to obtain the 45° approach direction. Wind tunnel tests for each model were conducted at fan motor speed percentages of 25% and 65% which corresponds to test wind speeds of 15 m/s and 40 m/s. The ambient temperature and air pressure readings were monitored and updated before each test. Data was sampled at 100 Hz for 1 minute for each test run. Baseline data sampled one minute before and one minute after each test run was subtracted from the measured test data to account for zero offset effects. The appropriate tare correction (Table 3.3 and 3.4), blockage correction (Table 3.5 and 3.6), and wind speed adjustments (Section 3.6) were applied to all test data.

3.7.2 Corner modification tests

This series of tests investigated the effects of modifying the model edges with round (Model 10) and chamfered (Model 11) corners. It was hypothesized that modified corners would reduce the drag coefficient by delaying the separation of flow around the VMS. Model 10 and 11 have the same overall dimensions as Model 9 (3.0 m. x 0.6 m. x 427 mm) but were constructed with 32 mm (5% of the vertical height) round and chamfered corners. Figures 3.15 and 3.16 show the round and chamfered model setups in the WOW respectively and Figure 3.17 shows close-up photos of the modified corners.

Figure 3.15 Round corner test setup in the WOW (a) Side view (b) Close-up

Figure 3.16 Chamfer corner test setup in the WOW (a) Side view (b) Close-up
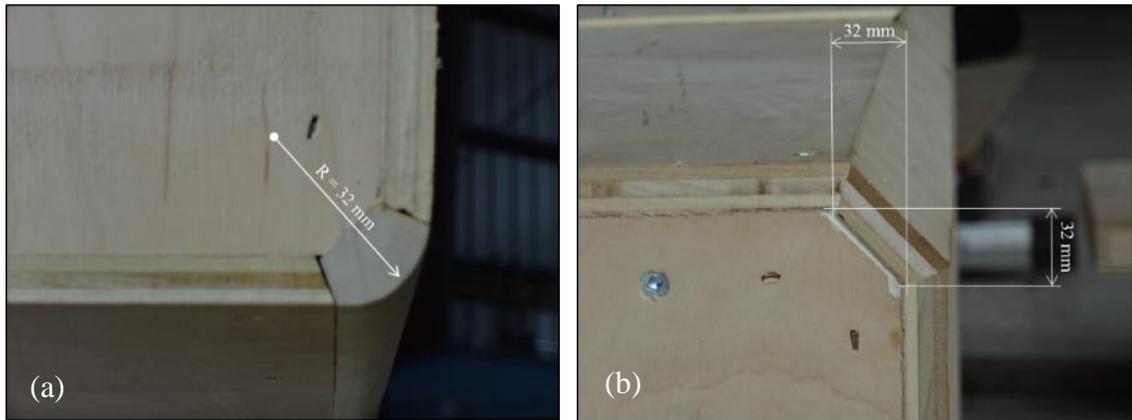
Figure 3.17 Modified corner close-up photos (a) Round corner (b) Chamfer corner

Testing was performed using the same parameters and conditions as the sharp edge tests. Corner modification tests were conducted for 0° and 45° horizontal wind approach directions in the simulated suburban boundary layer flow. Tests were conducted for 15 m/s and 40 m/s wind speeds. Data for each test run was sampled at 100 Hz for 1 minute. Baseline data sampled one minute before and one minute after each test run was subtracted from the measured test data to account for zero offset effects. The appropriate tare correction (Table 3.3 and 3.4), blockage correction (Table 3.5 and 3.6) and wind speed adjustments (Section 3.6) were applied to all test data.

3.7.3 Galloping tests

Tests were conducted to investigate the galloping potential of VMS. Model 9 ($b/c = 5$, $d/c = 0.7$) was attached to the double support configuration with a series of 2.5° and 4.5° wedges to vary the angle of attack of the approaching wind. The wedges were positioned to simulate both negative and positive angles of attack. The tests were conducted for wind attack angles of $\alpha = -4.5, -2.5, 0, 2.5,$ and 4.5 at wind speeds of 15 and 40 m/s. Figure 3.18 shows a schematic of the galloping test setup and Figure 3.19 shows pictures of the test setup in the WOW.
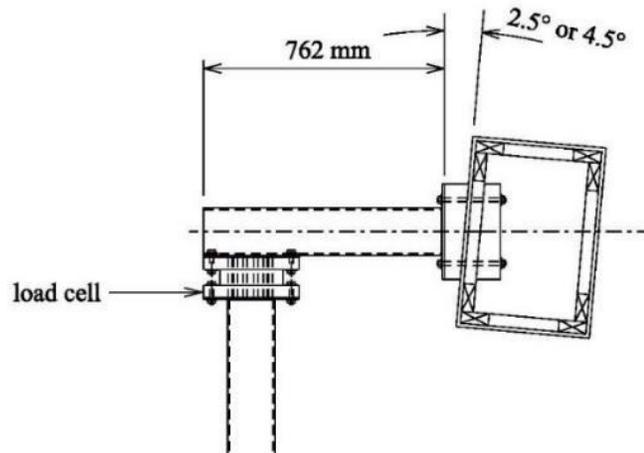
Figure 3.18 Galloping test schematic
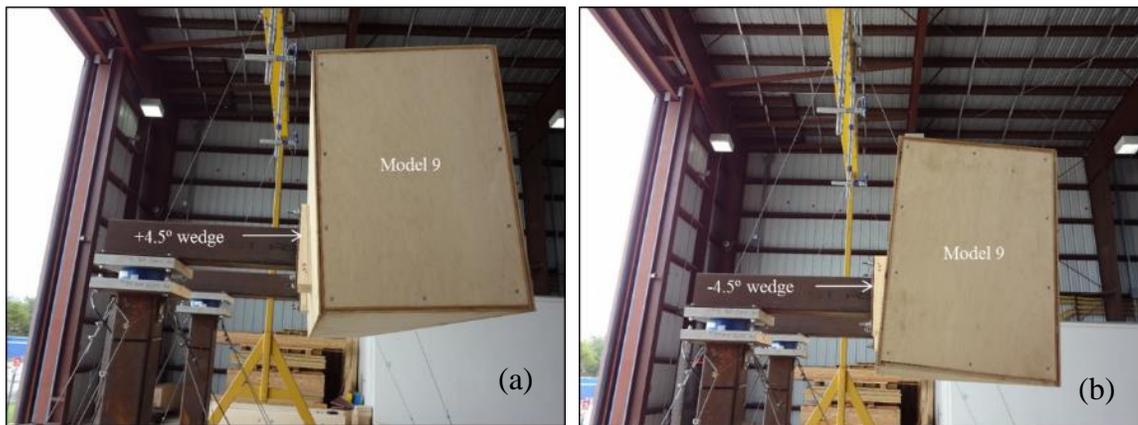
Figure 3.19 Galloping test setup in the WOW (a) Positive 4.5° angle (b) Negative 4.5° angle

The tests conditions were identical to the test conditions for the force coefficient tests for Models 1-9. Tests were conducted in the simulated suburban boundary layer for only the 0° horizontal wind approach direction. Data was sampled at 100 Hz for one minute. Baseline data sampled one minute before and one minute after each test run was subtracted

from the measured test data to account for zero offset effects. The appropriate tare correction (Table 3.3 and 3.4), blockage correction (Table 3.5), and wind speed adjustments (Section 3.6) were applied to all test data.

3.7.4 Wind driven rain test

Model 8 (3.0 m x 0.6 m x 427 mm) was subjected to a simulated high velocity wind driven rain environment by utilizing spray nozzles mounted on the exhaust side of the WOW fans. Figure 3.20 shows the configuration of four vertical lines of equally spaced spray nozzles utilized for the test setup. Since cobra probes could not be utilized during the wind driven rain test, the wind speed was assumed to be equal to the average wind speeds for the Model 8 force coefficient test (wind only). Testing was performed using the same parameters and conditions as the force coefficient tests for Model 8. This test was only conducted for the 45° horizontal wind direction. Tests were conducted for 15 m/s mph and 40 m/s wind speeds in the simulated suburban boundary layer flow. Data for each test run was sampled at 100 Hz for 1 minute. To account for zero offset effects, baseline data was subtracted from the measured test data. The appropriate tare correction (Table 3.3 and 3.4), blockage correction (Table 3.6), and wind speed adjustments (Section 3.6) were applied to all test data.

Figure 3.20 Wind driven rain test nozzle configuration

4.   TEST RESULTS AND DISCUSSIONS

Wind tunnel tests in the WOW were performed with the models and test configurations discussed in Chapter 3. A comprehensive research plan and test procedure was developed to attain the objectives of this project. The plan provided a logical sequence of work and ensured efficient use of the WOW facility. Table 4.1 shows the testing matrix for this study. Laboratory testing was conducted at the FIU WOW from May 28, 2013 to June 7, 2013.

Table 4.1 Testing matrix

Model No.	Test Speed						Wind Approach	
	20% 12 m/s	25% 15 m/s	30% 18 m/s	50% 30 m/s	60% 37 m/s	65% 40 m/s	0°	45°
1	✓	✓				✓	✓	✓
2	✓					✓	✓	✓
3	✓					✓	✓	✓
4	✓	✓				✓	✓	✓
5	✓					✓	✓	✓
6	✓	✓				✓	✓	✓
7	✓	✓				✓	✓	✓
8	✓	✓	✓	✓	✓	✓	✓	✓
9	✓	✓				✓	✓	✓
10	✓	✓		✓		✓	✓	✓
11	✓	✓		✓		✓	✓	✓
12			✓				✓	✓
13					✓		✓	✓

4.1   Force coefficients

Mean normal (C_{Fx}), lateral (C_{Fy}), and vertical lift (C_{Fz}) force coefficients were calculated from the measured data for each model using Equations 1-4, 1-5, and 1-6 respectively. Raw force measurements were adjusted using the load cell calibration matrix (see Appendix A) and initial baseline loads (no wind) were subtracted from the data. Applicable tare corrections (refer to Section 3.5) and wind field adjustments (see Section 3.6) were applied based on the model setup and test configuration. All force coefficients, except noted otherwise, were normalized using the area of the front face of the model ($A_x = b$ x c). A summary of mean force coefficient results for the 0° horizontal wind direction is included in Table 4.2 and the results for the 45° horizontal wind direction is included in Table 4.3.

Table 4.2 Summary of mean force coefficient results for the 0° wind direction

| Model No. | b | d | c | Aspect Ratio | Depth Ratio | 0° Wind Direction | | | | | |
| | | | | | | 15 m/s | | | 40 m/s | | |
	(m)	(m)	(m)	b/c	d/c	C_{Fx}	C_{Fy}	C_{Fz}	C_{Fx}	C_{Fy}	C_{Fz}
1	0.6	0.06	0.61	1	0.1	1.16	0.00	-0.06	1.15	0.00	-0.05
2	1.8	0.06	0.61	3	0.1	1.20	0.03	-0.08	1.22	0.01	-0.01
3	3.0	0.06	0.61	5	0.1	1.24	0.01	-0.07	1.28	0.01	0.00
4	0.6	0.24	0.61	1	0.4	1.05	0.03	-0.12	1.12	0.00	-0.03
5	1.8	0.24	0.61	3	0.4	1.17	0.03	-0.07	1.21	0.02	0.00
6	3.0	0.24	0.61	5	0.4	1.23	0.00	-0.06	1.25	0.00	0.00
7	0.6	0.43	0.61	1	0.7	0.97	0.00	0.00	0.98	0.01	0.01
8	1.8	0.43	0.61	3	0.7	1.12	-0.01	-0.05	1.16	0.02	0.04
9	3.0	0.43	0.61	5	0.7	1.19	0.00	-0.05	1.22	0.01	0.03
10	3.0	0.43	0.61	5	0.7	0.85	0.03	0.24	1.06	0.04	0.12
11	3.0	0.43	0.61	5	0.7	0.97	0.03	0.04	1.01	0.04	0.12
12	3.0	0.01	0.61	5	0.02	1.27	0.01	-0.04	-	-	-
13	1.5	0.01	0.30	5	0.04	-	-	-	1.27	0.01	0.06

Table 4.3 Summary of mean force coefficient results for the 45° wind direction

| Model No. | b | d | c | Aspect Ratio | Depth Ratio | 45° Wind Direction | | | | | |
| | | | | | | 15 m/s | | | 40 m/s | | |
	(m)	(m)	(m)	b/c	d/c	C_{Fx}	C_{Fy}	C_{Fz}	C_{Fx}	C_{Fy}	C_{Fz}
1	0.6	0.06	0.61	1	0.1	1.23	-0.12	-0.02	1.24	-0.10	0.06
2	1.8	0.06	0.61	3	0.1	1.13	-0.03	0.00	1.18	-0.06	0.04
3	3.0	0.06	0.61	5	0.1	1.02	-0.01	-0.04	1.11	-0.04	0.02
4	0.6	0.24	0.61	1	0.4	0.99	-0.35	-0.08	1.02	-0.36	0.01
5	1.8	0.24	0.61	3	0.4	1.03	-0.13	-0.06	1.06	-0.16	-0.01
6	3.0	0.24	0.61	5	0.4	0.99	-0.04	-0.05	1.03	-0.07	-0.04
7	0.6	0.43	0.61	1	0.7	0.93	-0.54	-0.07	0.94	-0.56	0.01
8	1.8	0.43	0.61	3	0.7	0.93	-0.21	0.05	0.95	-0.22	0.08
9	3.0	0.43	0.61	5	0.7	0.89	-0.11	0.02	0.91	-0.11	0.04
10	3.0	0.43	0.61	5	0.7	0.69	-0.07	0.00	0.74	-0.11	0.03
11	3.0	0.43	0.61	5	0.7	0.74	-0.06	0.10	0.72	-0.10	-0.06
12	3.0	0.01	0.61	5	0.02	1.04	-0.11	0.04	-	-	-
13	1.5	0.01	0.30	5	0.04	-	-	-	1.04	-0.47	0.22

4.1.1 Effect of aspect ratio

Variation of the normal force coefficient (C_{Fx}) as a function of aspect ratio (b/c) for the 0° horizontal wind direction is presented in Figure 4.1a and 4.1b for the selected depth ratios $d/c = 0.1, 0.4$, and 0.7. The plotted results for both the 15 m/s and 40 m/s wind speeds clearly show that the drag coefficient increased with aspect ratio. This is consistent with the normal force coefficient trends noted in the studies by Letchford (2001) and Zuo et al. (2014). The effect of increasing drag with increasing aspect ratio is attributed to the model becoming more two-dimensional as the aspect ratio increases. For models with a $b/c = 1$, flow is directed around the model equally, producing a narrow three-dimensional wake region. This results in less drag and a lower drag coefficient. As the width increases ($b/c = 3$ and $b/c = 5$), the end effects become less dominant and the flow interaction with the model is more two-dimensional. The flow is forced to travel faster over the top and bottom of the model which produces a wider, more two-dimensional wake region resulting in a higher drag coefficient. The lowest drag coefficient is obtained for model (Model 7) which has the smallest aspect ratio ($b/c = 1$) and the largest depth ratio ($d/c = 0.7$). This is because the model with lowest aspect ratio and highest depth ratio has the potential of forming the narrowest 3-D conical downwind wake due to dominant end effects and partial flow reattachment on the side faces as well as the top and bottom faces.

Figure 4.1a Effect of aspect ratio (b/c) on the normal force coefficient (C_{Fx}) for the 0° wind direction and 15 m/s wind speed

45
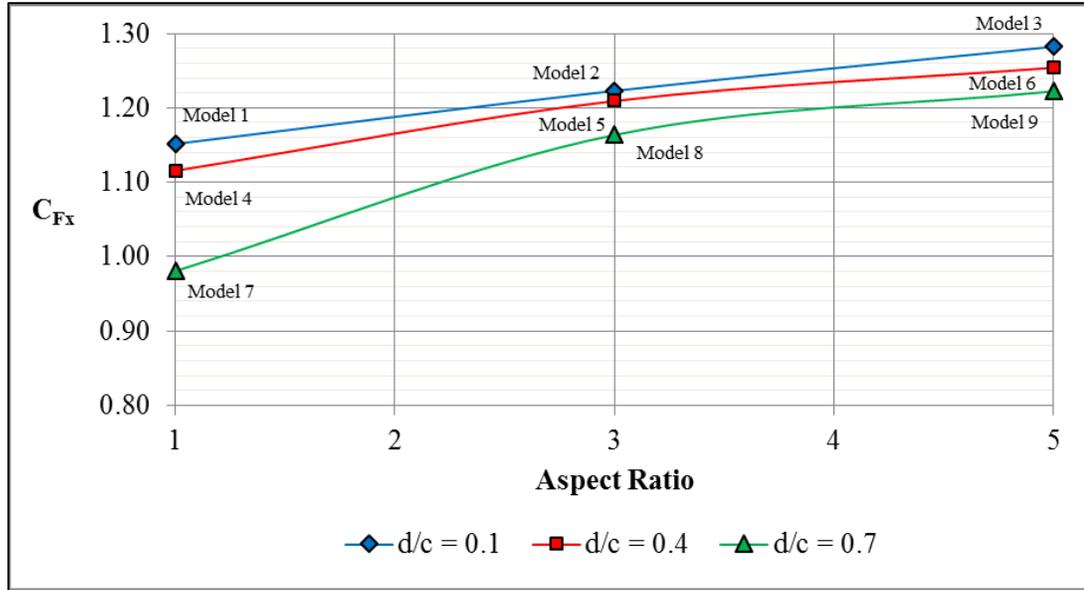
Figure 4.1b Effect of aspect ratio (*b/c*) on the normal force coefficient (C_{Fx}) for the 0°
wind direction and 40 m/s wind speed

Variation of the normal force coefficient (C_{Fx}) as a function of aspect ratio (*b/c*) for the
45° horizontal wind direction is presented in Figure 4.2a and 4.2b for the depth ratios *d/c*
= 0.1, 0.4, and 0.7. The results show that for a given depth ratio, the drag coefficient
generally decreases as the aspect ratio increases. However, for *d/c* = 0.4 and 0.7, C_{Fx}
increases slightly from *b/c* = 1 to *b/c* = 3 then decreases to *b/c* = 5. The sharpest decrease
in the normal force coefficient was measured for the models with the smallest depth ratio
(*d/c* = 0.1) corresponding to Models 1, 2 and 3.This is a reversal of the trend observed for
the 0° horizontal wind direction. In general, the largest drag coefficient for each tested
depth ratio was obtained for the model with the smallest aspect ratio.

The lateral force coefficient (C_{Fy}) was calculated using the following values for area in
the drag coefficient equation

$$A_x = b \text{ x } c \tag{4-1}$$

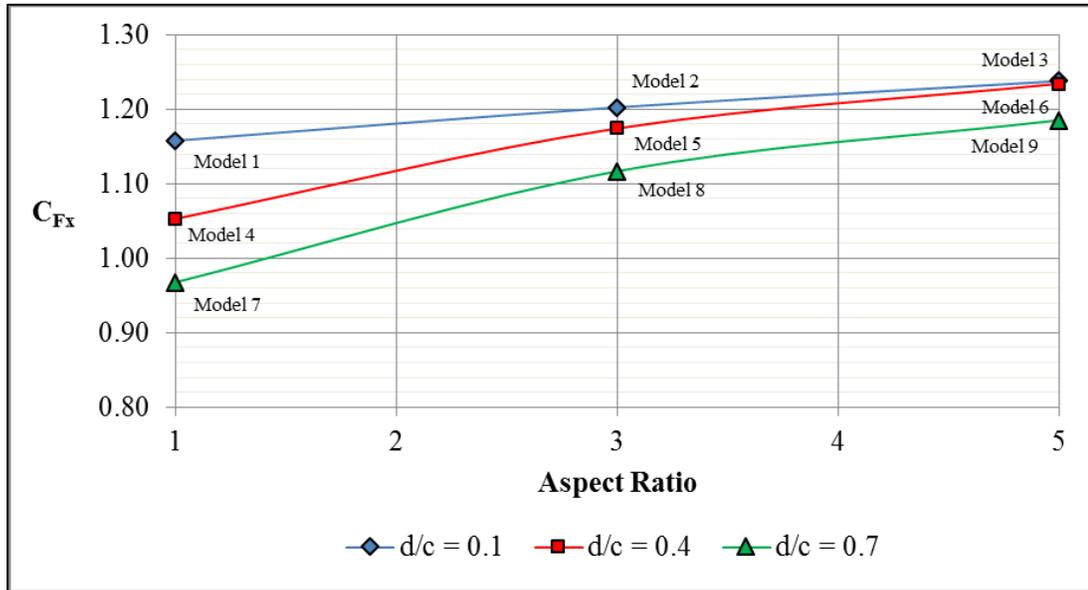$$A_y = d \text{ x } c \tag{4-2}$$

46

Figure 4.2a Effect of aspect ratio (*b/c*) on the normal force coefficient (*C_Fx*) for the 45°
wind direction and 15 m/s wind speed

Figure 4.2b Effect of aspect ratio (*b/c*) on the normal force coefficient (*C_Fx*) for the 45°
wind direction and 40 m/s wind speed

A summary and comparison of the result are included in Tables 4.4 and 4.5. As expected,
the results for C_{Fy} using A_x are small compared to the results for C_{Fy} using A_y since the area
of the front face for all the models is significantly larger than the area of the side face.
Consequently, the results for the 0° wind direction are approximately zero and only the 45°
wind direction results are discussed further for C_{Fy} using A_x. Figure 4.3a and 4.3b is a plot
of C_{Fy} using A_x as a function of aspect ratio for the tested depth ratios of 0.1, 0.4, and 0.7
in the 45° horizontal wind direction. All results indicate a decrease in C_{Fy} with increasing

aspect ratio. The largest decrease was measured for models with $d/c = 0.7$ (Model 7) which decreased from $C_{Fy} = -0.54$ for $b/c = 1$ to $C_{Fy} = -0.11$ for $b/c = 5$ (Model 9) resulting in 80% reduction in C_{Fy}. A negative value for C_{Fy} represents a result in the direction normal to the front face of the model (refer to Figure 1.5 for force orientation). The value of C_{Fy} using A_x for $b/c = 5$ appears to converge at approximately -0.05 for the 15 m/s wind speed and -0.07 for the 40 m/s wind speed. The largest C_{Fy} using A_x was obtained for Model 7 ($b/c = 1$ and $d/c = 0.7$) which was approximately $C_{Fy} = -0.55$. The smallest value of C_{Fy} using A_x was approximately $C_{Fy} = 0$ obtained for Model 3. The results for C_{Fy} using A_x are significantly affected by dividing the measured force by the comparatively large area of the front face. Consequently, it was decided that C_{Fy} using A_y would be a better representation of the findings.

Table 4.4 Summary of results for C_{Fy} using A_x and A_y for the 0° wind direction

Model No.	b	d	c	Aspect Ratio	Depth Ratio	A_x	A_y	C_{Fy} for 0° Wind Direction			
								15 m/s		40 m/s	
	(m)	(m)	(m)			(m²)	(m²)	Using A_x	Using A_y	Using A_x	Using A_y
1	0.61	0.06	0.61	1	0.1	0.37	0.04	0.00	0.01	0.00	0.02
2	1.83	0.06	0.61	3	0.1	1.11	0.04	0.03	0.84	0.01	0.35
3	3.05	0.06	0.61	5	0.1	1.86	0.04	0.01	0.37	0.01	0.39
4	0.61	0.24	0.61	1	0.4	0.37	0.15	0.03	0.08	0.00	0.00
5	1.83	0.24	0.61	3	0.4	1.11	0.15	0.03	0.24	0.02	0.13
6	3.05	0.24	0.61	5	0.4	1.86	0.15	0.00	0.03	0.00	0.04
7	0.61	0.43	0.61	1	0.7	0.37	0.26	0.00	0.01	0.01	0.01
8	1.83	0.43	0.61	3	0.7	1.11	0.26	-0.01	-0.03	0.02	0.07
9	3.05	0.43	0.61	5	0.7	1.86	0.26	0.00	0.01	0.01	0.08

Table 4.5 Summary of results for C_{Fy} using A_x and A_y for the 45° wind direction

Model No.	b	d	c	Aspect Ratio	Depth Ratio	A_x	A_y	C_{Fy} for 45° Wind Direction			
								15 m/s		40 m/s	
	(m)	(m)	(m)			(m²)	(m²)	Using A_x	Using A_y	Using A_x	Using A_y
1	0.61	0.06	0.61	1	0.1	0.37	0.04	-0.12	-1.16	-0.10	-1.05
2	1.83	0.06	0.61	3	0.1	1.11	0.04	-0.03	-0.86	-0.06	-1.89
3	3.05	0.06	0.61	5	0.1	1.86	0.04	-0.01	-0.31	-0.04	-2.21
4	0.61	0.24	0.61	1	0.4	0.37	0.15	-0.35	-0.87	-0.36	-0.89
5	1.83	0.24	0.61	3	0.4	1.11	0.15	-0.13	-0.95	-0.16	-1.22
6	3.05	0.24	0.61	5	0.4	1.86	0.15	-0.04	-0.48	-0.07	-0.87
7	0.61	0.43	0.61	1	0.7	0.37	0.26	-0.54	-0.77	-0.56	-0.79
8	1.83	0.43	0.61	3	0.7	1.11	0.26	-0.21	-0.91	-0.22	-0.93
9	3.05	0.43	0.61	5	0.7	1.86	0.26	-0.11	-0.76	-0.11	-0.75

Figure 4.3a Effect of aspect ratio (*b/c*) on the lateral force coefficient (C_{Fy}) using A_x for the 45° wind direction and 15 m/s wind speed
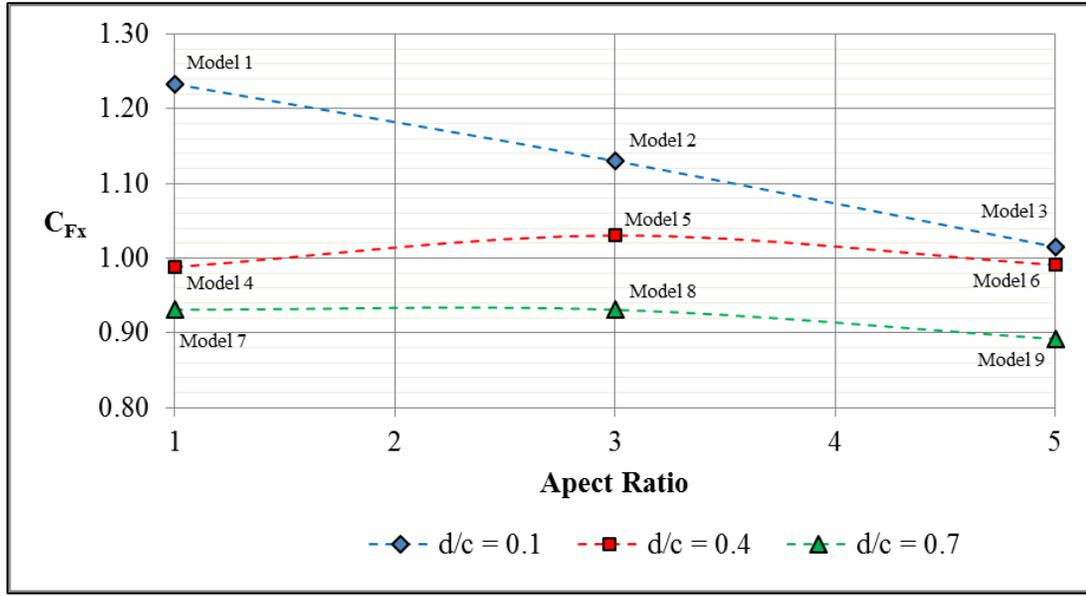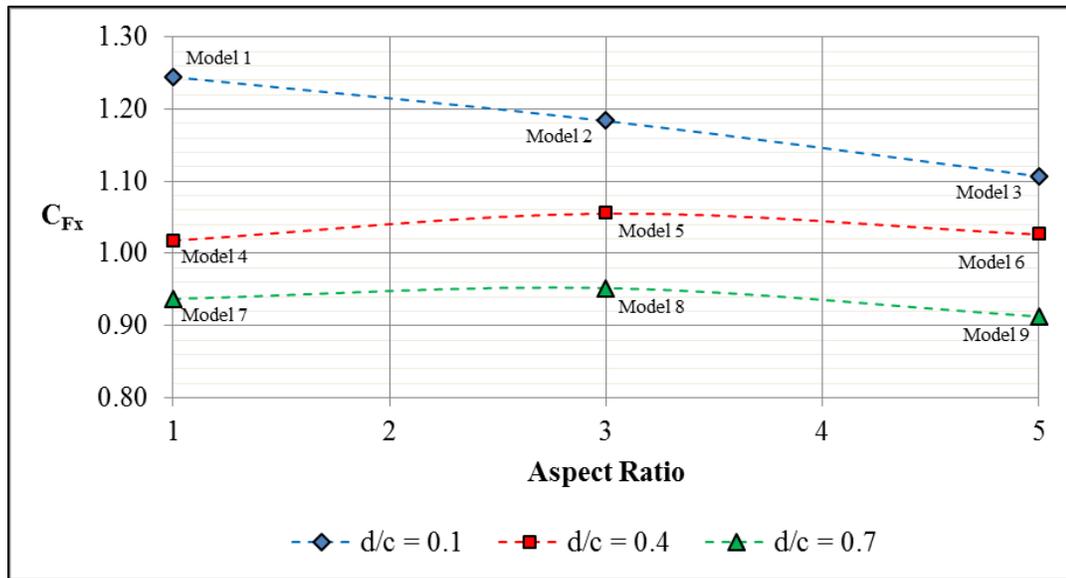

Figure 4.3b Effect of aspect ratio (*b/c*) on the lateral force coefficient (C_{Fy}) using A_x for the 45° wind direction and 40 m/s wind speed

As shown in Table 4.4, the results for C_{Fy} using A_y in the 0° wind direction for the 15 m/s test speed varies from approximately 0 to -0.84 and for the 40 m/s test speed varies from 0 to -0.39. For the 15 m/s wind speed the largest value ($C_{Fy} = 0.84$) was obtained for Model 2 (*b/c* = 3 and *d/c* = 0.1) and the smallest value ($C_{Fy} \approx 0$) was obtained for Models

1 and 6-9. For the 40 m/s wind speed the largest value ($C_{Fy} = 0.39$) was obtained for Model 3 ($b/c = 5$ and $d/c = 0.1$) and the smallest value ($C_{Fy} \approx 0$) was obtained for Models 1, 4, and 6. Figure 4.4a and 4.4b is a plot of C_{Fy} using A_y as a function of aspect ratio for the tested depth ratios of 0.1, 0.4, and 0.7 in the 0° horizontal wind direction. For the 15 m/s wind speed the value of C_{Fy} using A_y was approximately $C_{Fy} = 0$ for $d/c = 0.7$ (Models 7, 8, and 9). This was thought to occur because the flow partially reattached along the sides of the models and no lateral force develops. However, for $d/c = 0.1$ and 0.4, C_{Fy} using A_y increases dramatically from $b/c = 1$ to $b/c = 3$ then decreases for $b/c = 5$. This can be explained by noting that the flow around models with $b/c = 3$ and $b/c = 5$ is predominately over the top and bottom and an unequal force is produced in the lateral direction due to the alternating formation of vortices around the sides close to the rear of the model. This effect is more pronounced for the thinnest models ($d/c = 0.1$). The largest C_{Fy} using A_y for the 0° wind direction was $C_{Fy} = 0.84$ obtained for Model 2 ($b/c = 3$ and $d/c = 0.1$) and the largest increase in C_{Fy} using A_y was between $C_{Fy} \approx 0$ for Model 1 ($b/c = 1$ and $d/c = 0.1$) and $C_{Fy} = 0.84$ for Model 2. Similar trends in C_{Fy} using A_y were noted for the 40 m/s wind speed test but the values were generally smaller. An exception was also noted for models with $d/c = 0.1$. There was a slight increase in C_{Fy} using A_y from $b/c = 3$ to $b/c = 5$ instead of the sharp decrease noted in the 15 m/s wind speed tests. In summary, mean lateral forces are expected to be small, 1 or 2% of the drag force. The values obtained in this study are an indication of the resolution of the experiment.
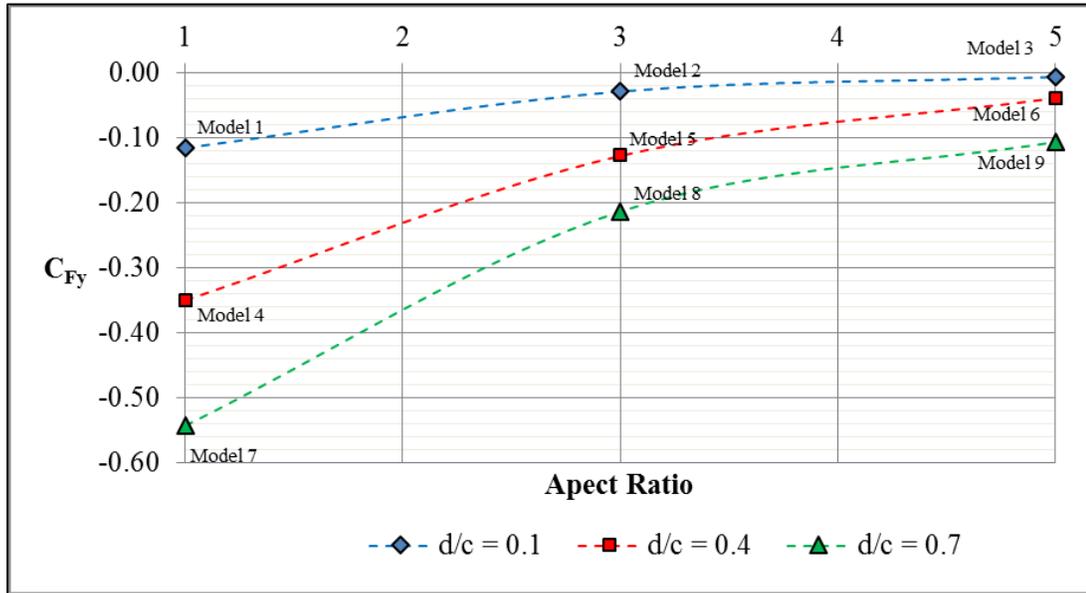

Figure 4.4a Effect of aspect ratio (b/c) on the lateral force coefficient (C_{Fy}) using A_y for the 0° wind direction and 15 m/s wind speed
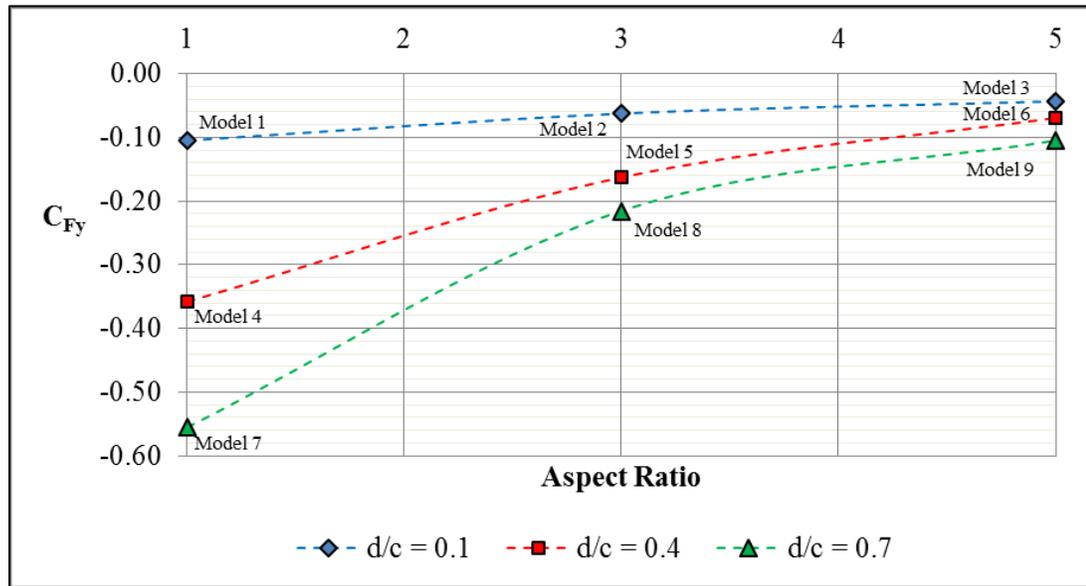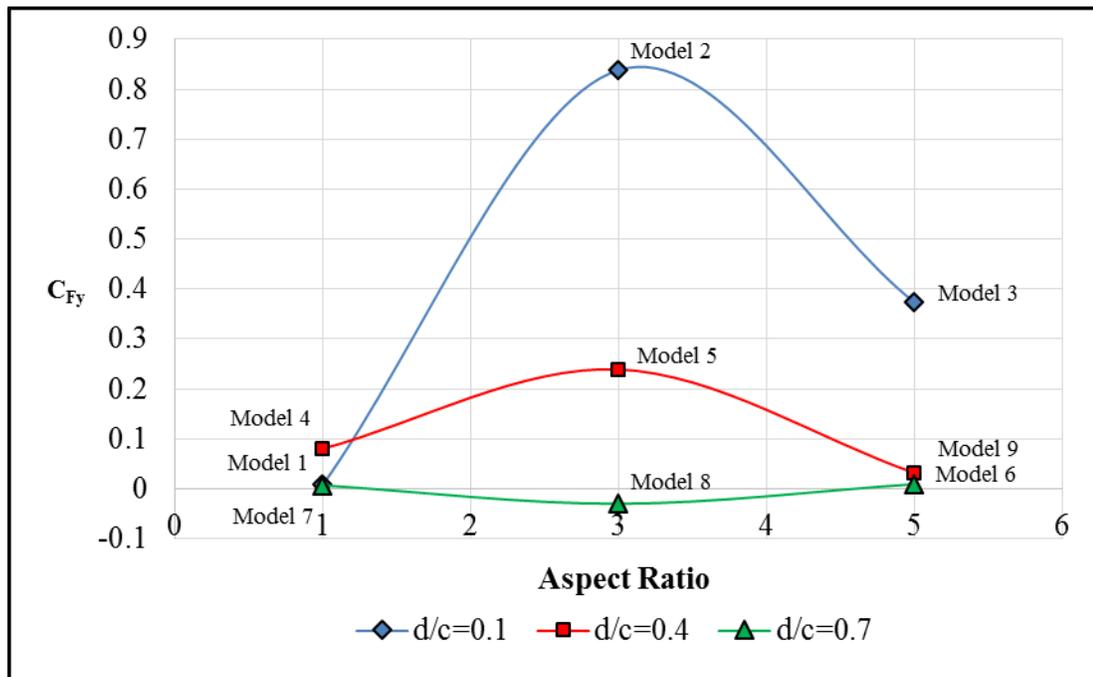
Figure 4.4b Effect of aspect ratio (b/c) on the lateral force coefficient (C_{Fy}) using A_y for the 0° wind direction and 40 m/s wind speed

Figure 4.5a and 4.5b shows the trend of C_{Fy} using A_y as a function of aspect ratio for the 45° wind direction. In contrast to the results for the 0° wind direction, all results for the 45° wind direction are negative (refer to Figure 1.5 for the force orientation). This result is expected due to the positioning of the model with respect to the oncoming flow and the positive orientation of F_y which is 90° to the front face of the model. The values for C_{Fy} using A_y for the 45° wind direction are generally larger than the results obtained for the 0° wind direction. This is also due to the 45° orientation of the model with respect to the oncoming flow since the side face closest to the WOW outlet (see Figure 3.25) is directly impacted by the oncoming flow. For the 15 m/s wind speed test with d/c =0.1, C_{Fy} using A_y decreases from C_{Fy} = -1.16 to C_{Fy} = -0.31 (73% decrease) with increasing aspect ratio. The values of C_{Fy} using A_y for models with d/c = 0.4 and 0.7 increase slightly from b/c = 1 to b/c = 3 then decrease to b/c =5. The largest C_{Fy} using A_y was C_{Fy} = -1.16 obtained for Model 1 and the smallest was obtained for Model 3 which was C_{Fy} = -0.31. The 40 m/s wind speed test results for d/c = 0.4 and d/c = 0.7 are similar to the trends noted for the 15 m/s wind speed tests. However, C_{Fy} using A_y for d/c = 0.1 increases sharply with increasing aspect ratio from C_{Fy} = -1.05 to C_{Fy} = -2.21 for a 110% increase. The largest 45° C_{Fy} using A_y measured was C_{Fy} = -2.21 for Model 3 and the smallest was C_{Fy} = -0.75 obtained for Model 9.

51

Figure 4.5a Effect of aspect ratio (*b/c*) on the lateral force coefficient (C_{Fy}) using A$_y$ for the 45° wind direction and 15 m/s wind speed
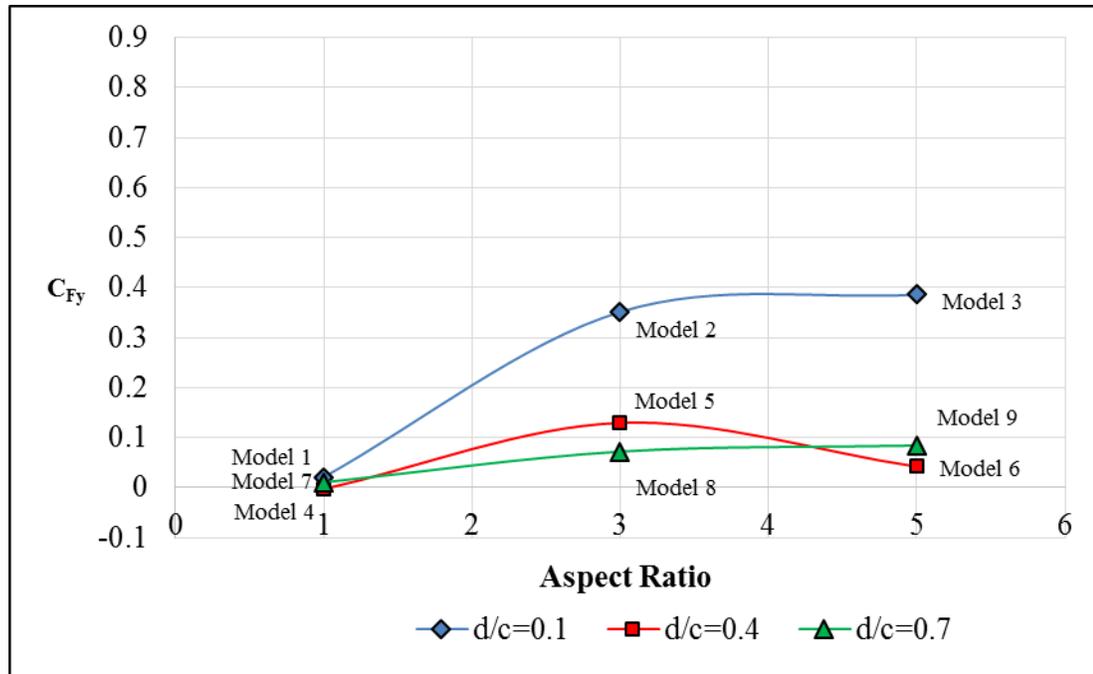

Figure 4.5b Effect of aspect ratio (*b/c*) on the lateral force coefficient (C_{Fy}) using A$_y$ for the 45° wind direction and 40 m/s wind speed

4.1.2   Effect of depth ratio

   Figure 4.6a and 4.6b shows the variation of the normal force coefficient (C_{Fx}) for the 0° horizontal wind approach as a function of depth ratio for the selected aspect ratios $b/c = 1$, 3, and 5. The plotted results for the 15 m/s and 40 m/s wind speeds showed a decreasing trend in the drag coefficient with increasing depth ratio for all aspect ratios tested. These results suggest that partial reattachment of flow over a prismatic VMS reduces the drag force resulting in a smaller drag coefficient for use in design. The sharpest decrease in normal force was noted for the square models, $b/c = 1$ (Models 1, 4 and 7). As the model becomes deeper, flow reattachment is promoted over the sides and the top and bottom faces. Model 7 (largest depth ratio and lowest aspect ratio), produced the narrowest 3-D conical downwind wake which resulted in the smallest normal force coefficient among all models tested.
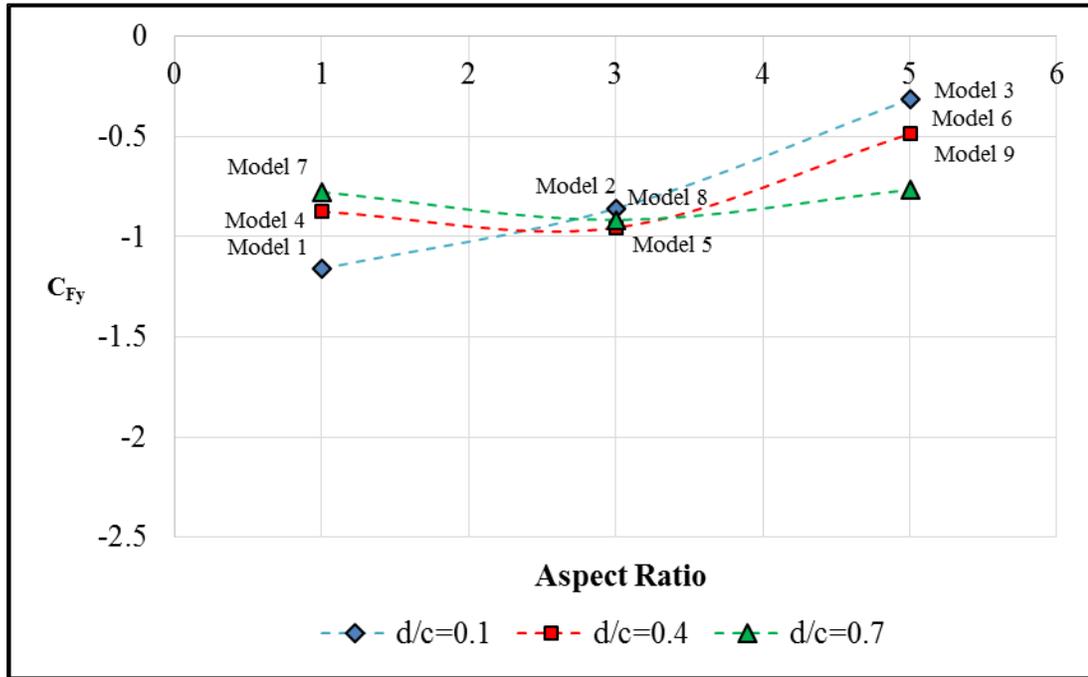

Figure 4.6a Effect of depth ratio (d/c) on the normal force coefficient (C_{Fx}) for the 0° wind direction and 15 m/s wind speed
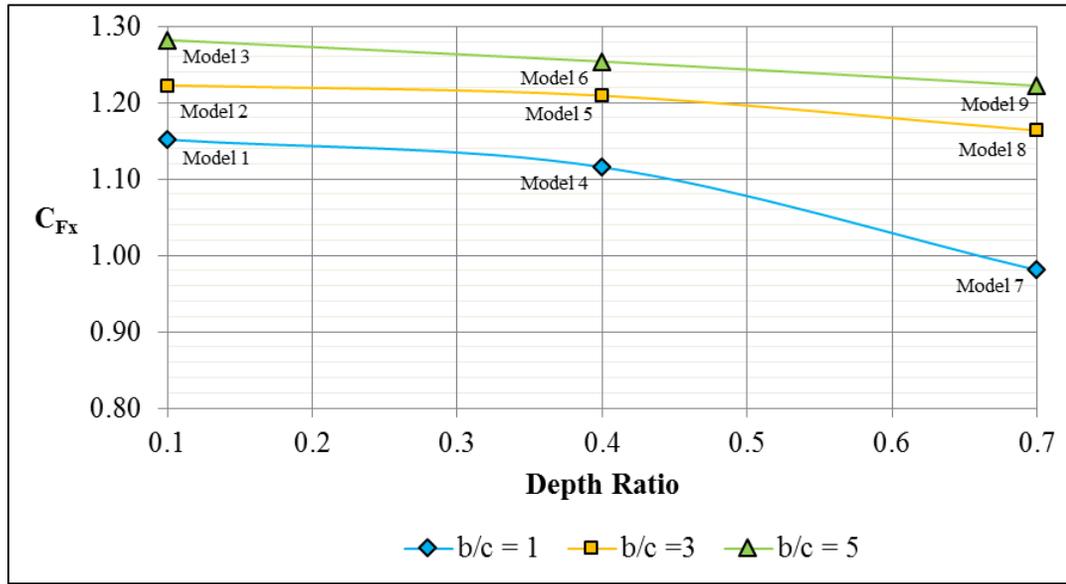
Figure 4.6b Effect of depth ratio (d/c) on the normal force coefficient (C_{Fx}) for the 0°
wind direction and 40 m/s wind speed

Figure 4.7a and 4.7b shows the variation of the C_{Fx} for the 45° horizontal wind approach as a function of depth ratio (d/c) for the aspect ratios $b/c = 1$, 3, and 5. The graphs indicated that C_{Fx} for the 45° wind direction also decreased with increasing depth ratio. Similar to the 45° horizontal wind approach trends for aspect ratio, the normal force coefficient decreased as the depth of the model increased (increased depth ratio). For each aspect ratio, C_{Fx} decreases as the length of the side face increases (depth ratio increases). The smallest C_{Fx} for the 15 m/s wind speed test ($C_{Fx} = 0.89$) was obtained for Model 9 ($d/c = 0.7$, $b/c = 5$), the deepest and longest model. Conversely, the largest ($C_{Fx} = 1.23$) was obtained for Model 1 which had the smallest aspect ratio ($b/c = 1$) and the smallest depth ratio ($d/c = 1$).
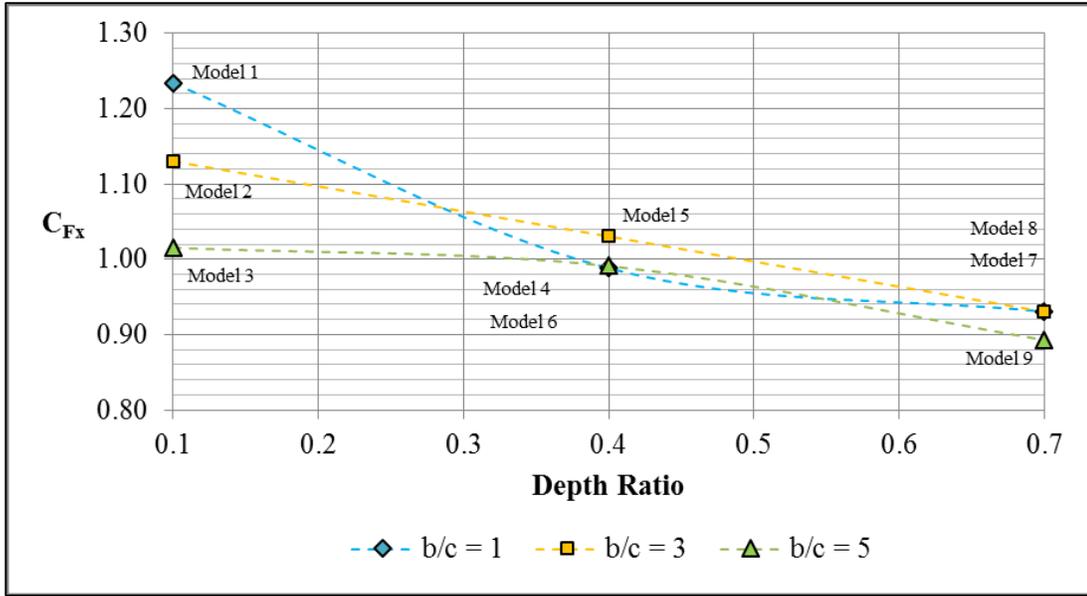
Figure 4.7a Effect of depth ratio (d/c) on the normal force coefficient (C_{Fx}) for the 45° wind direction and 15 m/s
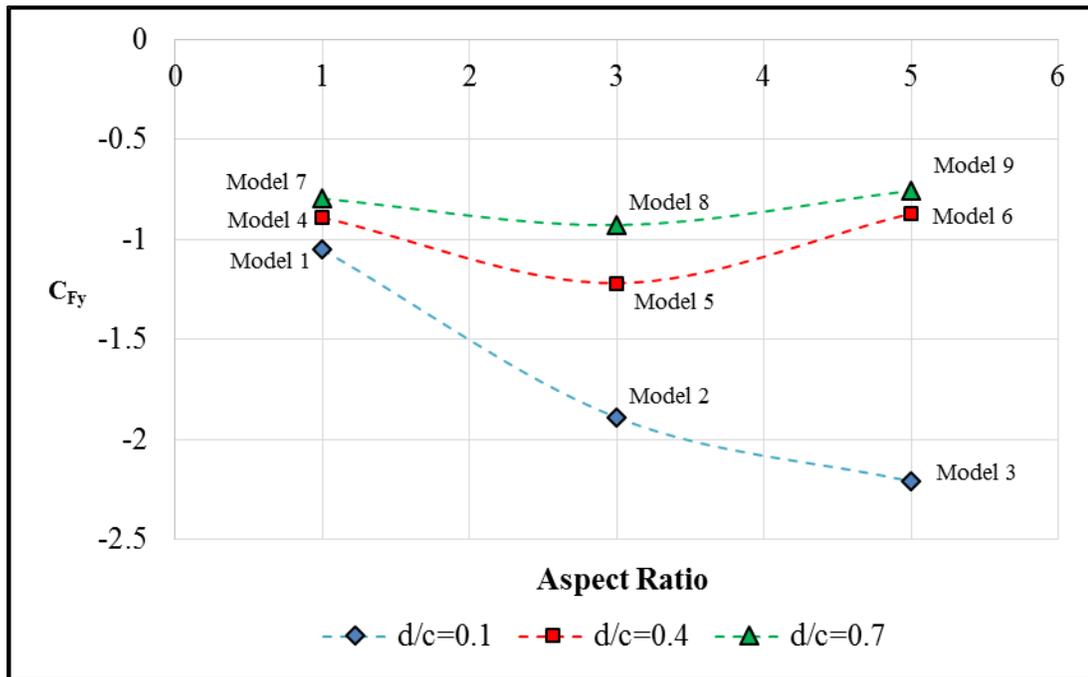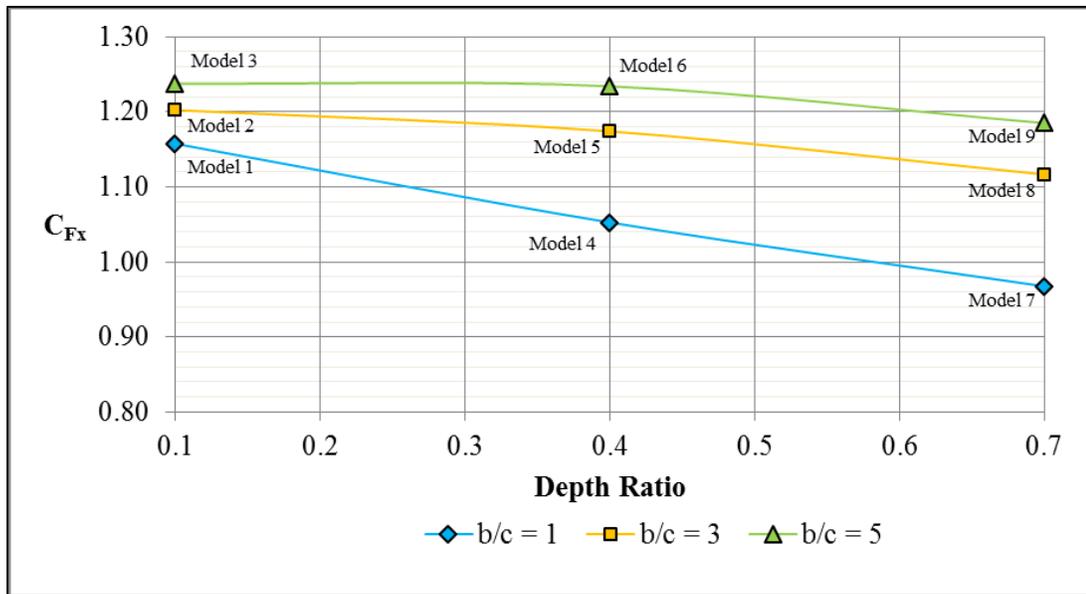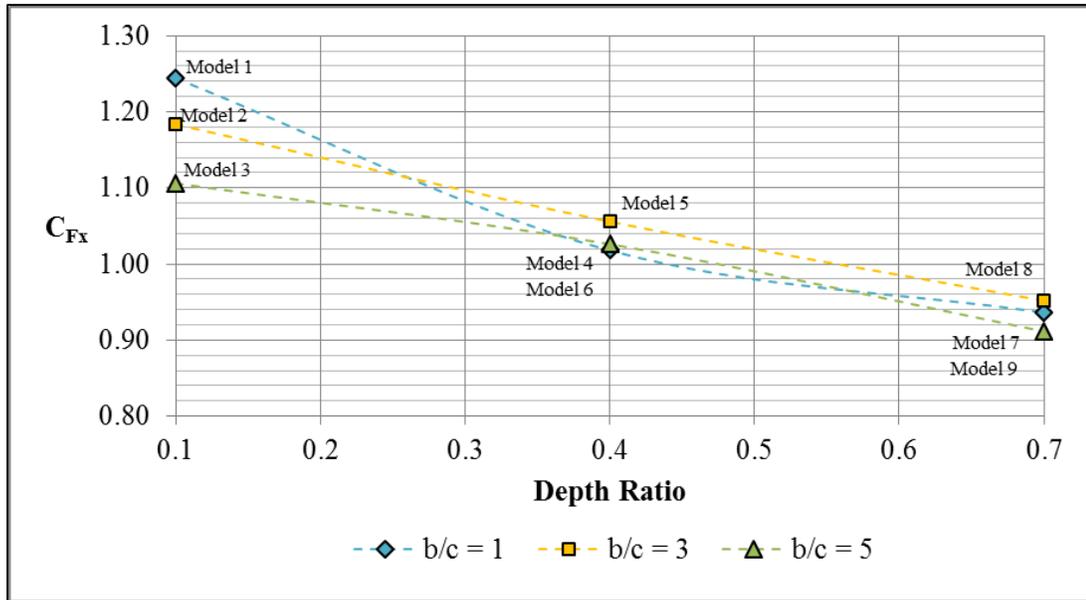

Figure 4.7b Effect of depth ratio (d/c) on the normal force coefficient (C_{Fx}) for the 45° wind direction and 40 m/s wind speed

The results for C_{Fy} using A_x in the 0° horizontal wind direction are approximately zero and consequently not discussed. Figure 4.8a and 4.8b is a plot of C_{Fy} using A_x as a function of depth ratio for the tested aspect ratios of 1, 3, and 5 in the 45° horizontal wind direction. C_{Fy} using A_x is shown to increase with increasing depth ratio for all model tested. Figure 4.9a and 4.9b shows the plot of C_{Fy} using A_y as a function of the depth ratio for the 0° wind direction for the tested aspect ratios of 1, 3, and 5. For $b/c = 1$ the value of C_{Fy} using A_y is

approximately equal to zero. As already discussed in conjunction with the results for C_{Fx} as a function of aspect ratio in the 0° wind direction (Section 4.1.1), the flow around models with $b/c = 1$ produced a narrow 3D wake region and no significant lateral forces develop. However, for the 15 m/s wind speed and $b/c = 3$ and 5, C_{Fy} decreases with increasing depth ratio and converges to approximately zero at $d/c = 0.7$. Again this could be due to partial reattachment of flow along the sides of models with $d/c = 0.7$ resulting in minimal force development in the lateral direction. The plot for the 40 m/s wind speed test was similar except for a slight increase in C_{Fy} for $b/c = 5$ from $d/c = 0.4$ to $d/c = 0.7$.

Figure 4.8a Effect of depth ratio (d/c) on the lateral force coefficient (C_{Fy}) using A_x for the 45° wind direction and 15 m/s wind speed

Figure 4.8b Effect of depth ratio (*d/c*) on the lateral force coefficient (*C_{Fy}*) using A_x for the 45° wind direction and 40 m/s wind speed

Figure 4.9a Effect of depth ratio (*d/c*) on the lateral force coefficient (*C_{Fy}*) using A_y for the 0° wind direction and 15 m/s wind speed

Figure 4.9b Effect of depth ratio (d/c) on the lateral force coefficient (C_{Fy}) using A_y for the 0° wind direction and 40 m/s wind speed

Figure 4.10a and 4.10b is a plot of C_{Fy} using A_y as a function of depth ratio for the tested aspect ratios of 0.1, 0.4, and 0.7 in the 45° horizontal wind direction. For the 15 m/s wind speed, C_{Fy} using A_y for $b/c = 1$ is shown to decrease with increasing depth ratio (34% decrease), C_{Fy} using A_y for $b/c = 5$ is shown to increase with increasing depth ratio (145% increase) and C_{Fy} using A_y for $b/c = 3$ remains approximately constant at $C_{Fy} = -0.91$. For the 40 m/s wind speed, C_{Fy} using A_y decreases with increasing depth ratio for all models tested.
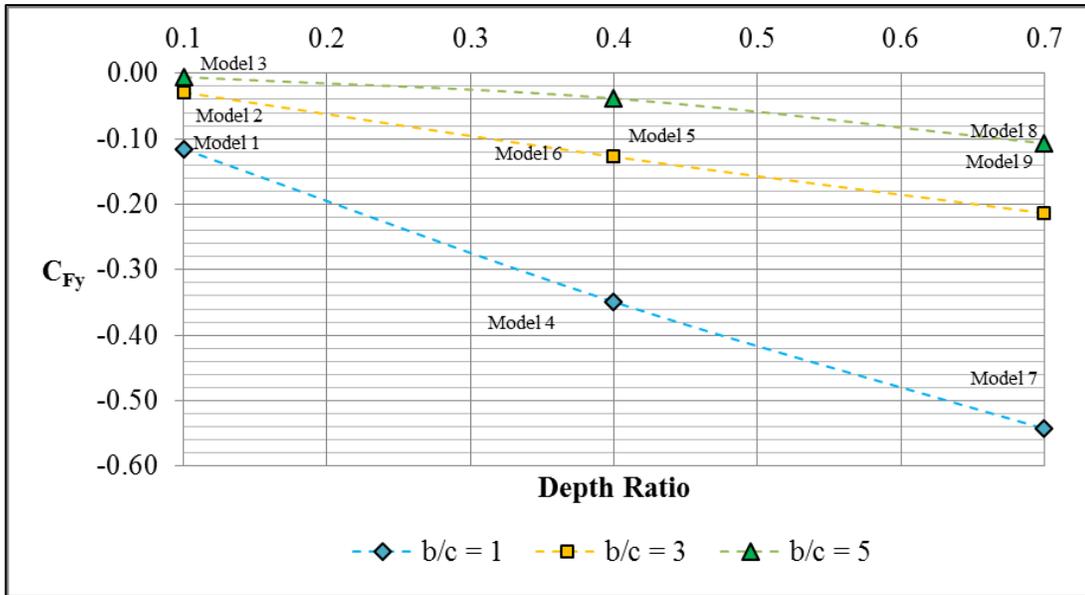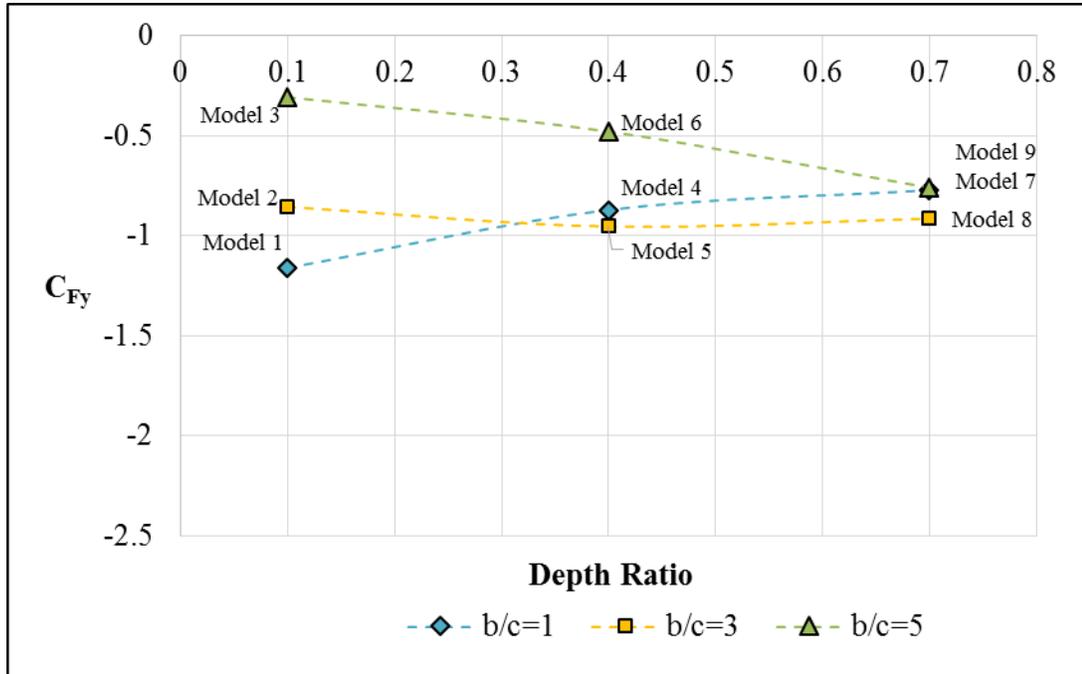
Figure 4.10a Effect of depth ratio (*d/c*) on the lateral force coefficient (*C_{Fy}*) using A_y for the 45° wind direction and 15 m/s wind speed
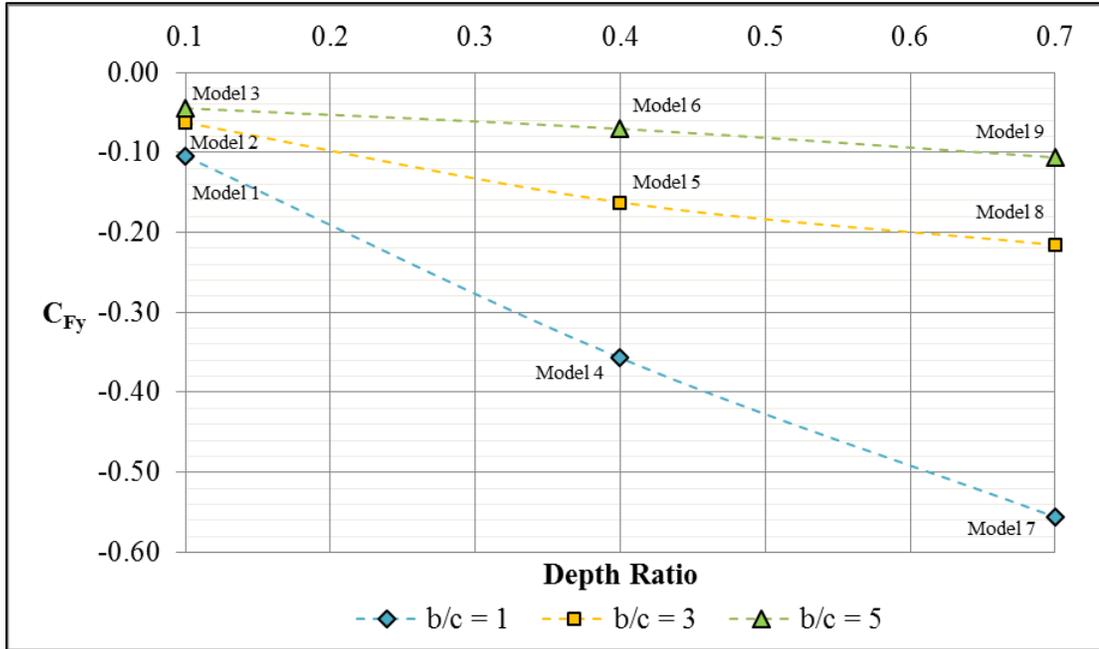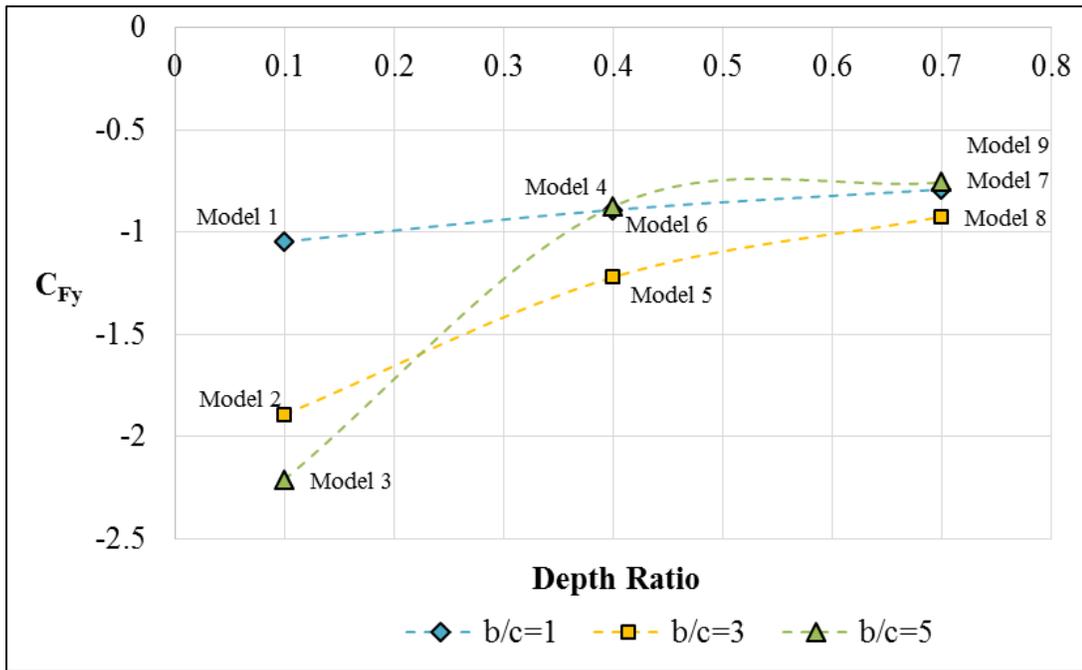

Figure 4.10b Effect of depth ratio (*d/c*) on the lateral force coefficient (*C_{Fy}*) using A_y for the 45° wind direction and 40 m/s wind speed
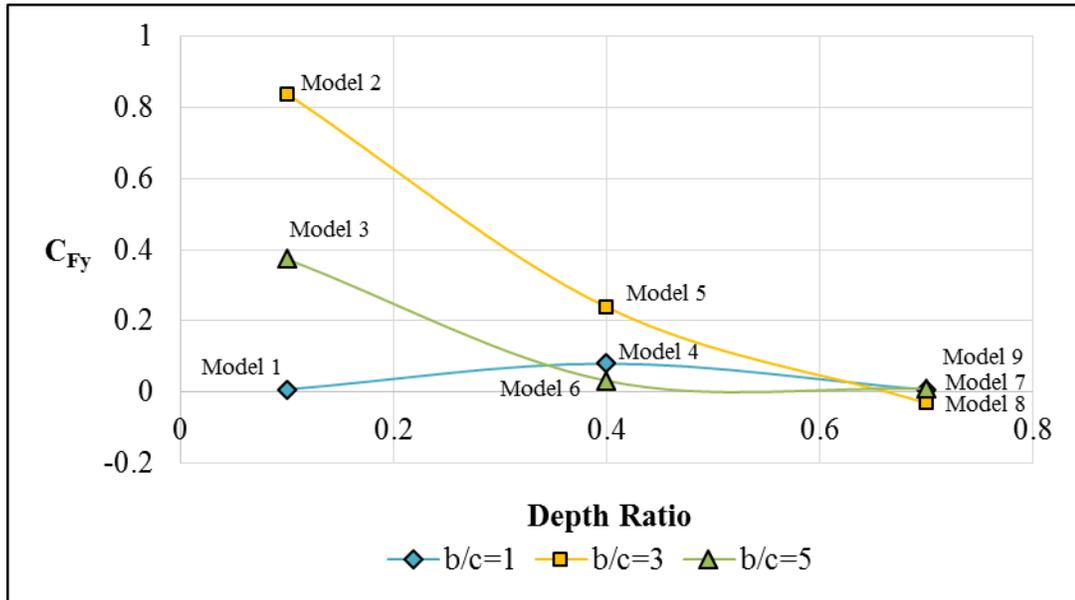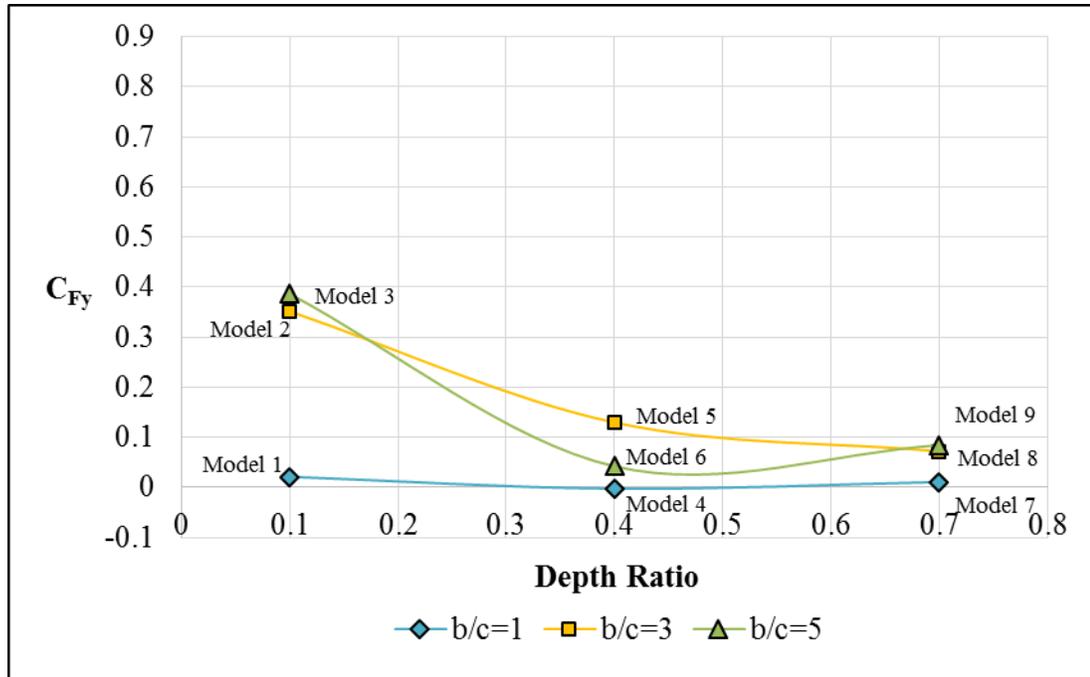
4.1.3 Effect of wind direction

A comparison of C_{Fx} results in the 0° and 45° wind direction is shown in Figure 4.11a and 4.11b. As illustrated, the C_{Fx} results for the 45° horizontal wind approach direction for all models tested were smaller than the 0° horizontal wind approach direction except for Model 1. C_{Fx} for the 45° direction for Model 1 (C_{Fx} = 1.24) was 7% larger than the 0° result (C_{Fx} = 1.16). This finding was noted in preliminary testing and again during final testing. The square shape and small depth ratio may have contributed to this unique result. One possible explanation is that the negative pressure created on the rear leading edge is larger for structures with a short width (b) dimension. In addition, as the depth (d) dimension increases, the streamlines are deflected around the shape instead of curling around the rear edge. This reduces the negative pressure on the rear leading edge resulting in a reduced mean normal force coefficient. The largest variation for the 15 m/s wind speed was generally noted for models with b/c = 5 (Models 3, 6 and 9) with an average difference of 0.25 and the smallest variation was noted for models with b/c = 1 (Models 1, 4, and 7) with an average difference of 0.06. The results for the 40 m/s wind speed tests were similar. The average difference for models with b/c = 1 was 0.08 and the average difference for models with b/c = 5 was 0.23. The largest difference between C_{Fx} results for the 0° and 45° wind directions was approximately 0.30 for Model 9.
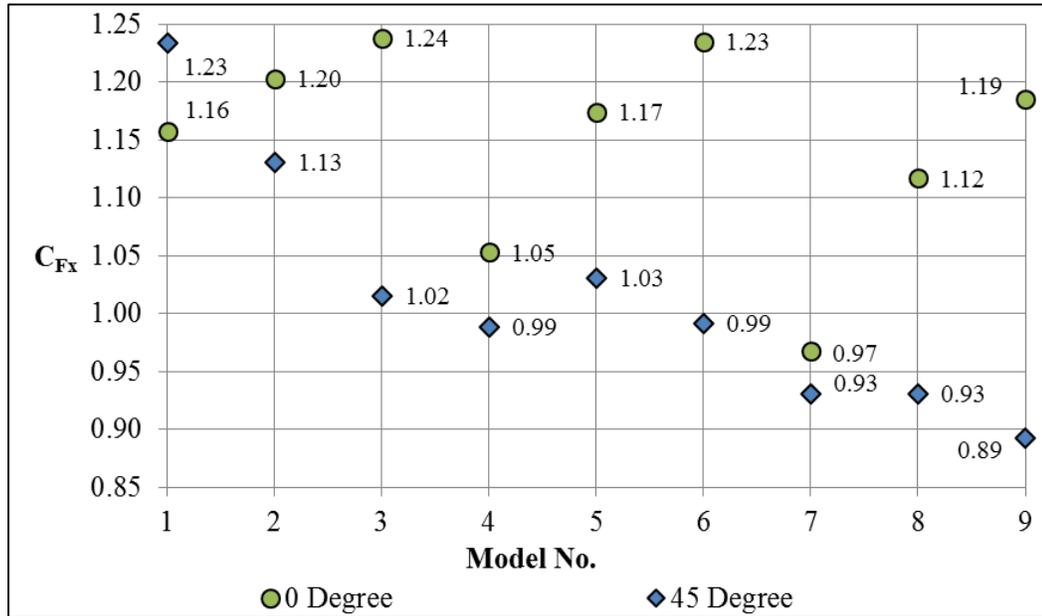
Figure 4.11a Comparison of normal force coefficients (C_{Fx}) for the 0° and 45° wind directions and 15 m/s wind speed
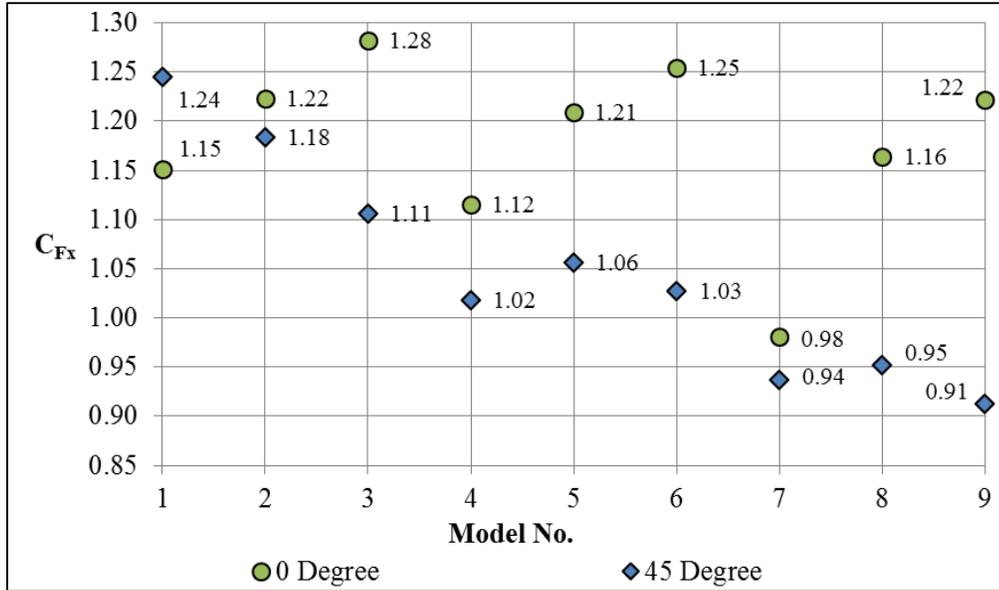
Figure 4.11b Comparison of normal force coefficients (C_{Fx}) for the 0° and 45° wind directions and 40 m/s wind speed

Figure 4.12 shows a comparison of results for 0° and 45° wind directions for C_{Fy} using A_y. As noted previously, the results for the 0° wind direction are approximately equal to zero (except for the small forces measured for Models 2, 3 and 5) while the results for the 45° wind direction are larger and negative due to the wind impacting the end faces directly . The largest difference for C_{Fy} using A_y was 1.7 (Model 2) for the 15 m/s wind speed and 2.6 (Model 3) for the 40 m/s wind speed.
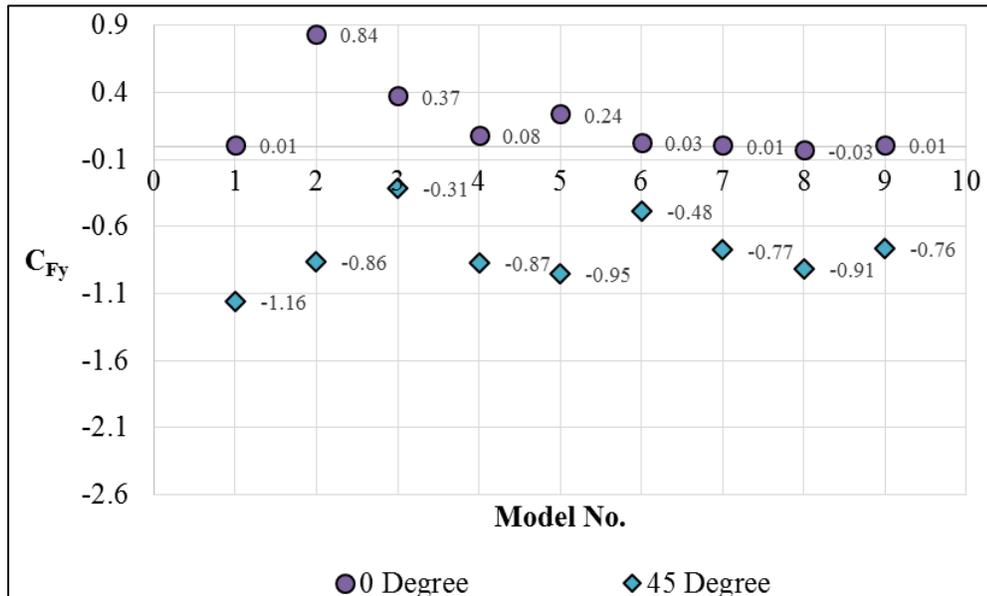
Figure 4.12a Comparison of lateral coefficients (C_{Fy}) using A_y for the 0° and 45°wind directions and 15 m/s wind speed

61
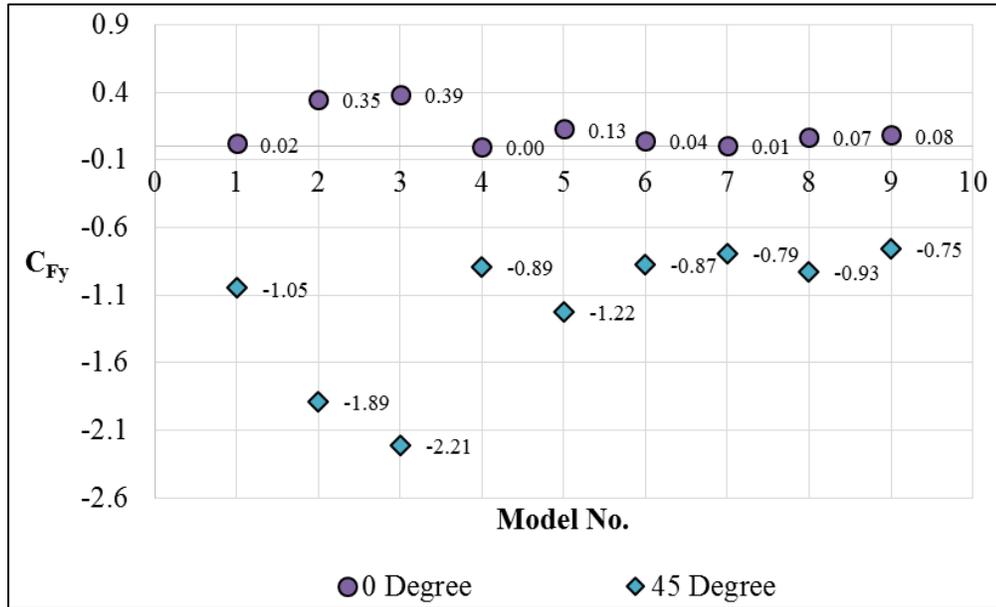
Figure 4.12b Comparison of lateral coefficients (C_{Fy}) using A_y for the 0° and 45°wind directions and 40 m/s wind speed

4.1.4 Reynolds number effect

All models were tested for wind speeds of 15 m/s and 40 m/s which corresponds to a Reynolds Number (*Re*) test range of 5.96 x 10^5 to 1.59 x 10^6. *Re* is defined as:

$$R_e = \frac{c\bar{U}}{\nu} \tag{4-15}$$

Where c is the height of model (0.6 m), $\bar{U}$ is the mean free flow wind speed (m/s) at 2.3 m, and ν is the viscosity of air (1.51 x 10^{-5} m²/sec).

The normal and lateral force coefficients as a function of the Reynolds number are plotted in Figure 4.13. Test results were evaluated to determine the sensitivity of sharp edge models to *Re* effects. Letchford (2001) noted a decreasing trend in C_{Fx} with higher wind speeds but concluded that there is little evidence to support Re dependency. In contrast, the results of this study indicate a small increase in C_{Fx} and C_{Fy} using A_y with wind speed for sharp edge models (Models 1-9) but this was thought to be caused by the introduction of additional vibration in the test setup at higher speeds. Consequently *Re* effects were not considered in this study. However, a possible *Re* dependency was noted for the increase in C_{Fx} for the round edge configuration (Model 10). This illustrates the importance of corner configuration in determining *Re* effects.
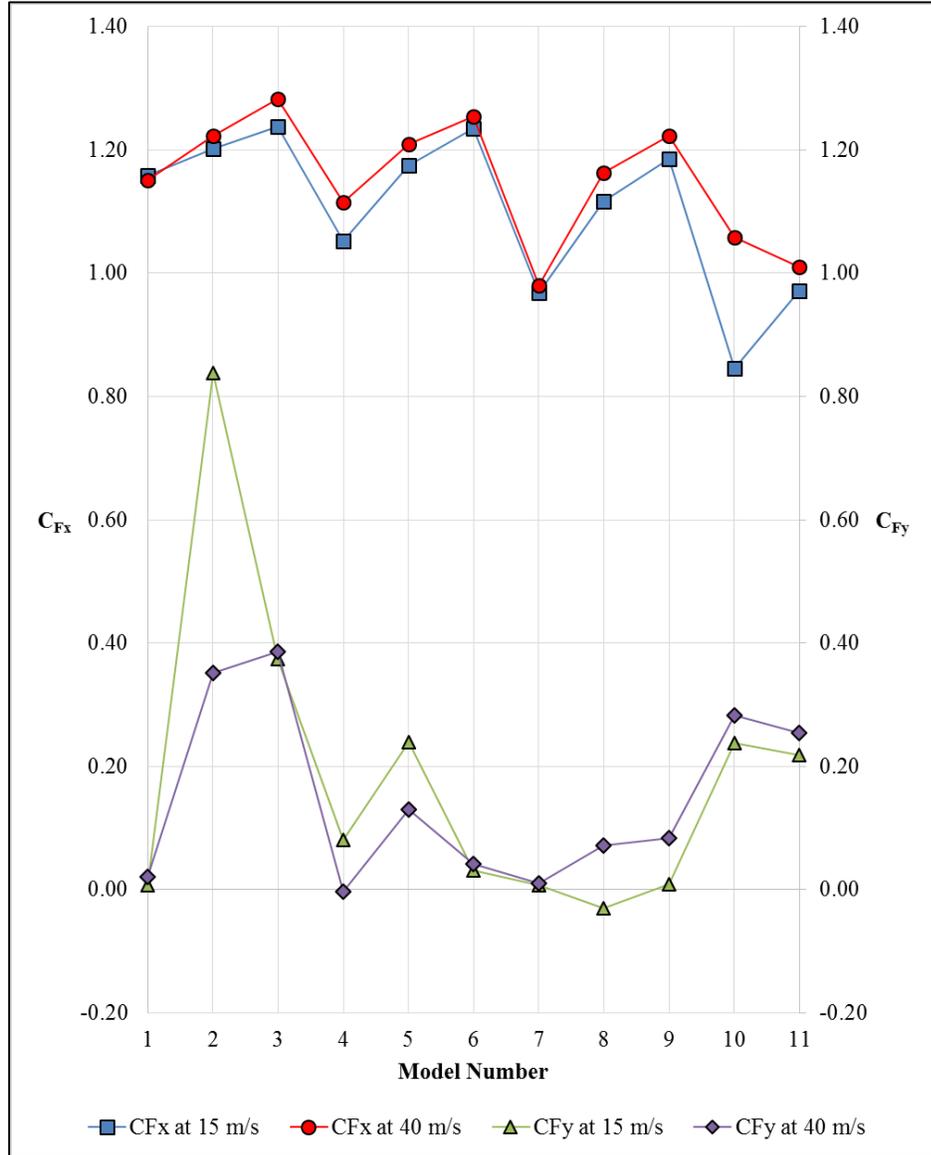
Figure 4.13 C_{Fx} and C_{Fy} using A_y as a function of wind speed

4.2   Twisting coefficient and eccentricity estimates for fatigue and strength design

The twisting moment coefficient was calculated using Equation 1-13 with the sign conventions shown in Figure 1.5. The non-dimensional eccentricity ratio was calculated using Equation 1-16. Table 4.6 is a summary of the results for the twisting moment (C_{Mz}) and eccentricity ratio (r/b) for the 0° horizontal wind direction and Table 4.7 is a summary of the results for the 45° wind direction. The eccentricity for the 0° horizontal wind approach direction is approximately zero for all the models tested. Consequently, only the results for the 45° wind direction are discussed in detail. The largest calculated eccentricity is $r/b = 0.13$ for Model 2 which is still lower than the ASCE 7-10 (2010) suggested code value of 0.2. It should be noted that the current AASHTO specification (2013) does not include a design requirement for eccentricity.

Table 4.6 Summary of twisting moment and eccentricity ratio results for the 0° wind direction

Model No.	15 m/s			40 m/s		
	C_{Mz}	r/b	r	C_{Mz}	r/b	r
1	0.00	0.00	0.00	0.00	0.00	0.00
2	-0.01	-0.01	-0.02	-0.01	-0.01	-0.01
3	-0.01	-0.01	-0.02	0.00	0.00	0.00
4	-0.04	-0.04	-0.03	0.00	0.00	0.00
5	-0.01	-0.01	-0.02	-0.01	-0.01	-0.02
6	0.00	0.00	-0.01	0.00	0.00	-0.01
7	0.01	0.01	0.00	0.00	0.00	0.00
8	-0.01	-0.01	-0.02	0.00	0.00	0.00
9	-0.01	-0.01	-0.03	0.00	0.00	-0.01

Table 4.7 Summary of twisting moment and eccentricity ratio results for the 45° wind direction

Model No.	15 m/s			40 m/s		
	C_{Mz}	r/b	r	C_{Mz}	r/b	r
1	0.13	0.11	0.06	0.13	0.10	0.06
2	0.14	0.12	0.22	0.15	0.13	0.23
3	0.11	0.11	0.33	0.13	0.11	0.34
4	0.05	0.05	0.03	0.06	0.06	0.04
5	0.11	0.11	0.19	0.13	0.12	0.22
6	0.09	0.09	0.27	0.10	0.10	0.30
7	0.02	0.02	0.01	0.03	0.03	0.02
8	0.08	0.09	0.16	0.08	0.08	0.15
9	0.06	0.07	0.20	0.06	0.07	0.21

4.2.1 Effect of aspect ratio

Variation of the twisting moment (C_{Mz}) as a function of aspect ratio (b/c) for the 45° horizontal wind direction is graphed in Figure 4.14a and 4.14b for the selected depth ratios $d/c = 0.1, 0.4$, and 0.7. The results show that for a given depth ratio, the twisting moment coefficient increases from $b/c = 1$ to $b/c = 3$ then decreases at $b/c = 5$. The largest twisting moment coefficient ($C_{Mz} = 0.15$) was obtained for Model 2 and the smallest ($C_{Mz} = 0.03$) for Model 7. The average C_{Mz} for models with b/c = 1, 3 and 5 was 0.07, 0.12 and 0.10 respectively. The results of the eccentricity ratio as function of aspect ratio are plotted in

Figure 4.15a and 4.15b. As expected, the plotted trend for the eccentricity ratio follows the plotted results of the twisting moment coefficient. The largest eccentricity ratio was calculated to be 0.13 (Model 2) and the smallest was 0.03 (Model 7).
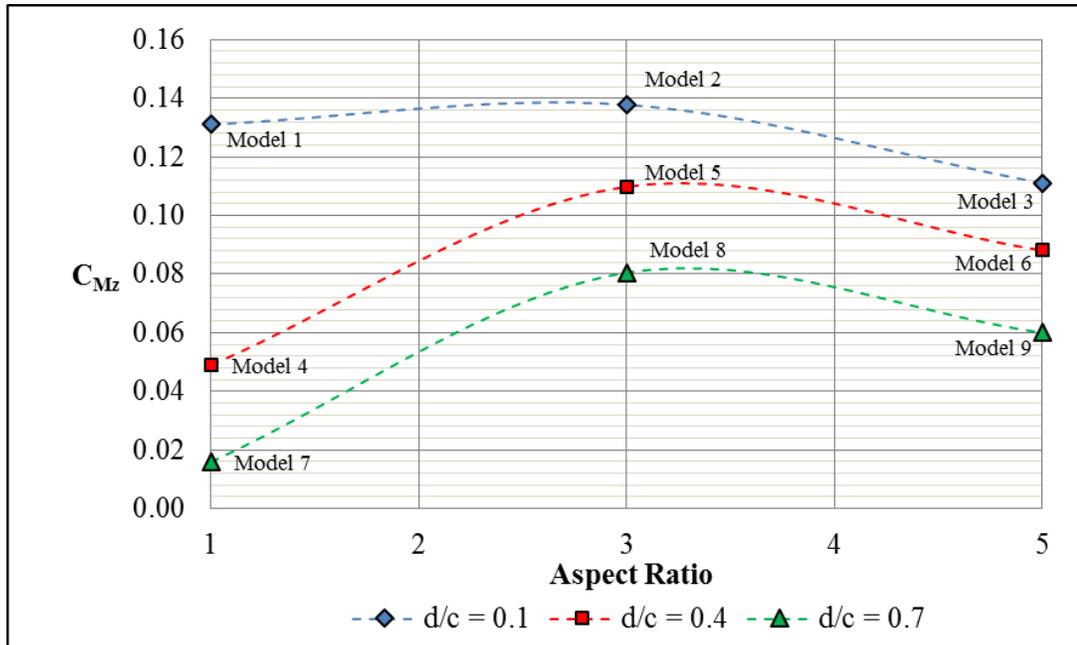
Figure 4.14a Effect of aspect ratio (*b/c*) on the twisting moment coefficient (C_{Mz}) for the 45° wind direction and 15 m/s wind speed
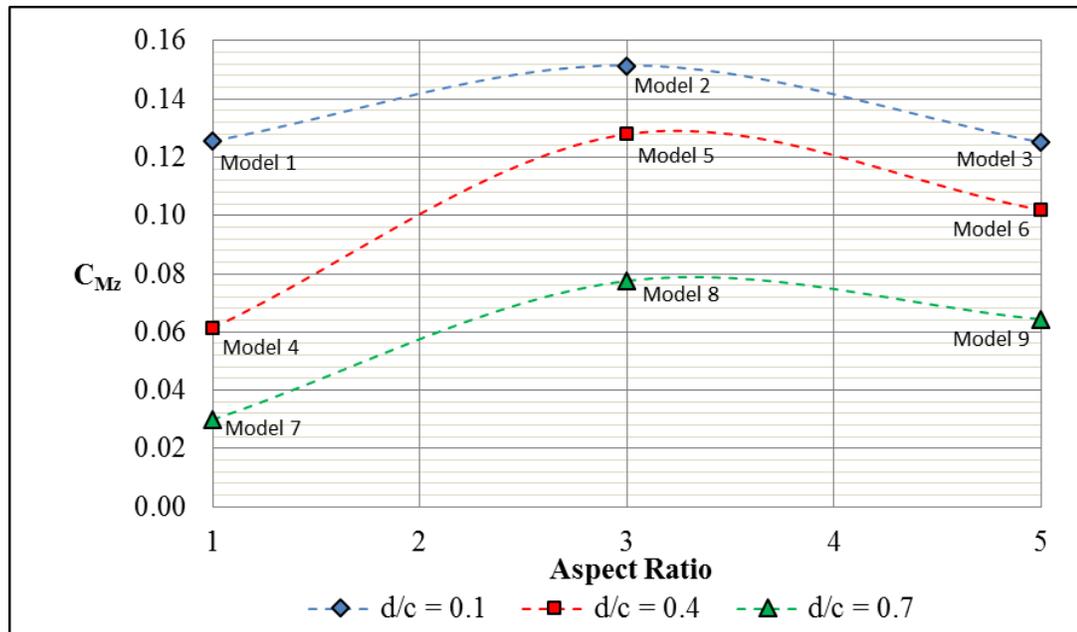
Figure 4.14b Effect of aspect ratio (*b/c*) on the twisting moment coefficient (C_{Mz}) for the 45° wind direction and 40 m/s wind speed
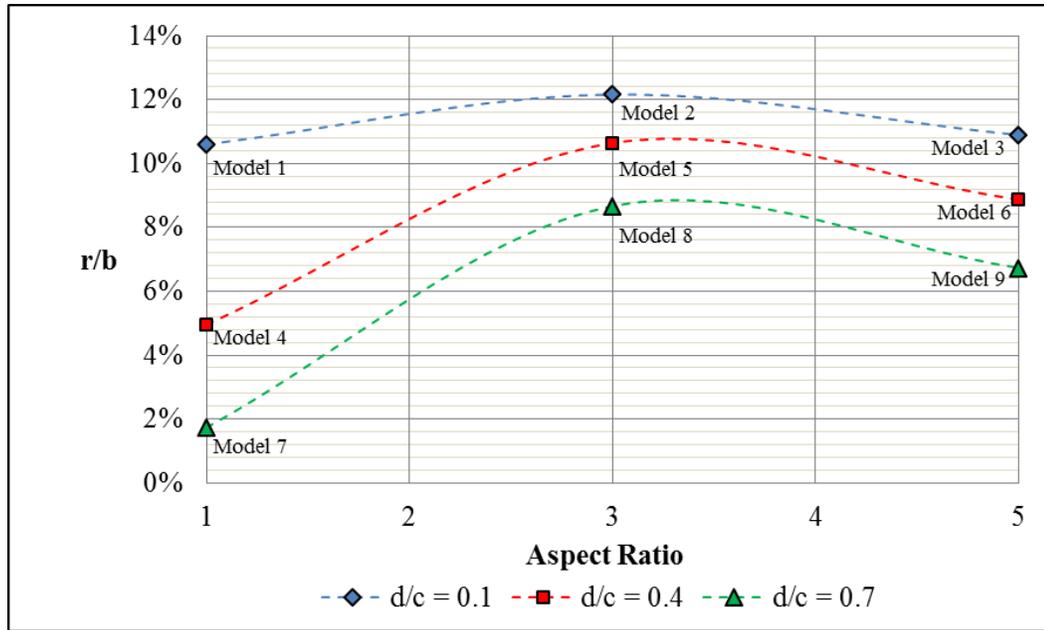
Figure 4.15a Effect of aspect ratio (*b/c*) on the eccentricity ratio (*r/b*) for the 45° wind direction and 15 m/s wind speed
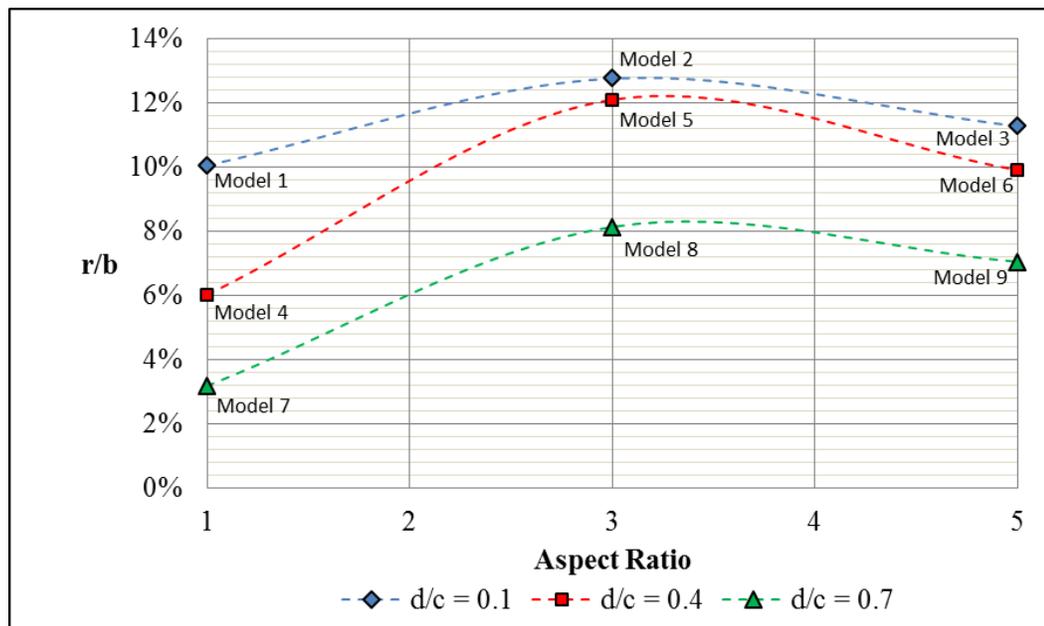
Figure 4.15b Effect of aspect ratio (*b/c*) on the eccentricity ratio (*r/b*) for the 45° wind direction and 40 m/s wind speed

4.2.2 Effect of depth ratio

Variation of the twisting moment (C_{Mz}) as a function of depth ratio (*d/c*) for the 45° wind direction is plotted in Figure 4.16a and 4.16b for the selected aspect ratios *b/c* = 1, 3, and 5. The results show that for a given aspect ratio, C_{Mz} decreases with increasing depth

66

ratio. The results of the eccentricity ratio as function of depth ratio is plotted in Figure 4.17 and follows the same trend as the twisting moment.
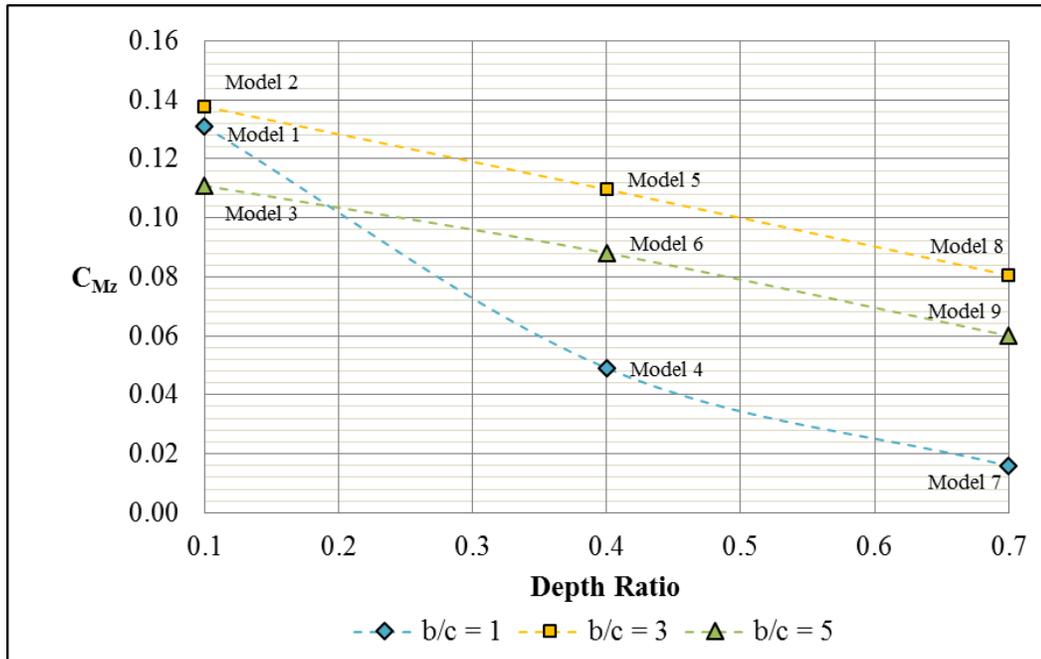
Figure 4.16a Effect of depth ratio (*d/c*) on the twisting moment coefficient (*C_Mz*) for the 45° wind direction and 15 m/s wind speed
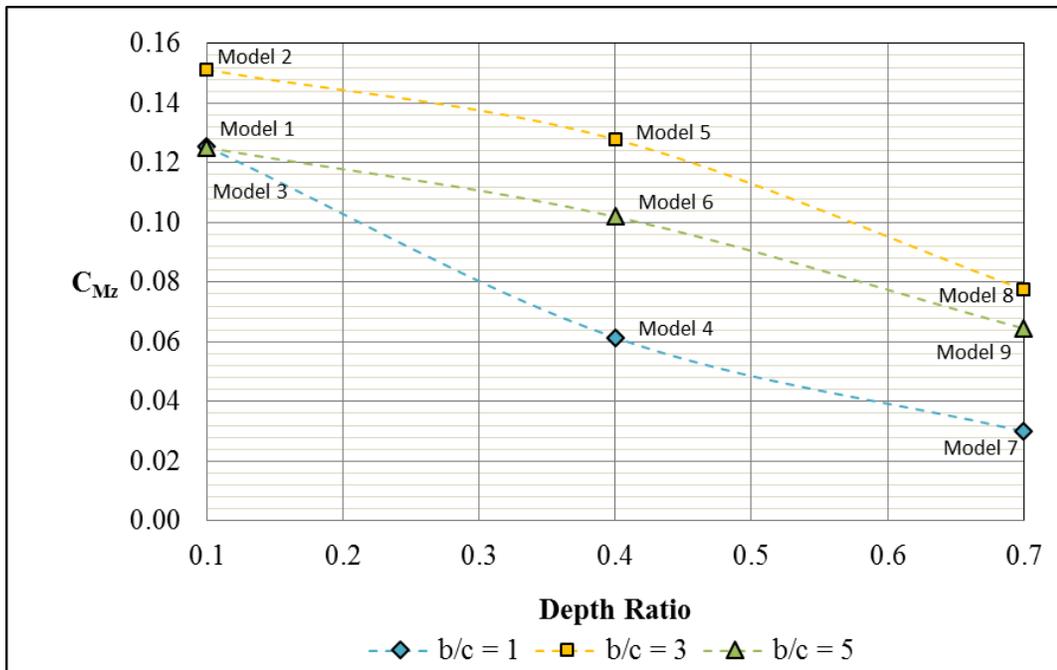
Figure 4.16b Effect of depth ratio (*d/c*) on the twisting moment coefficient (*C_Mz*) for the 45° wind direction and 40 m/s wind speed

67
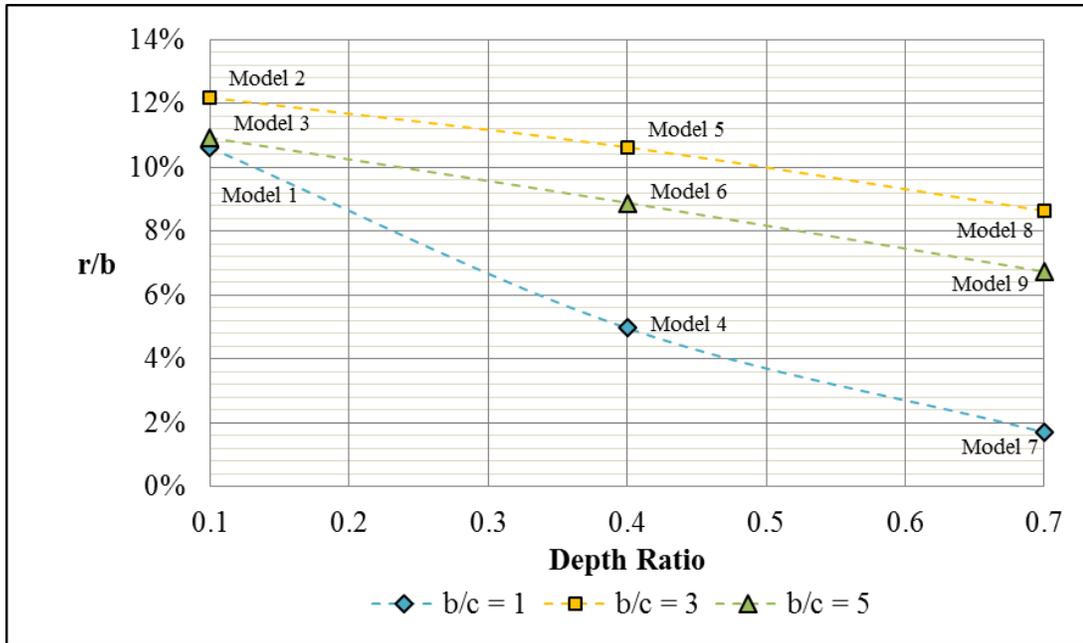
Figure 4.17a Effect of depth ratio (*d/c*) on the eccentricity ratio (*r/b*) for the 45° wind direction and 15 m/s wind speed
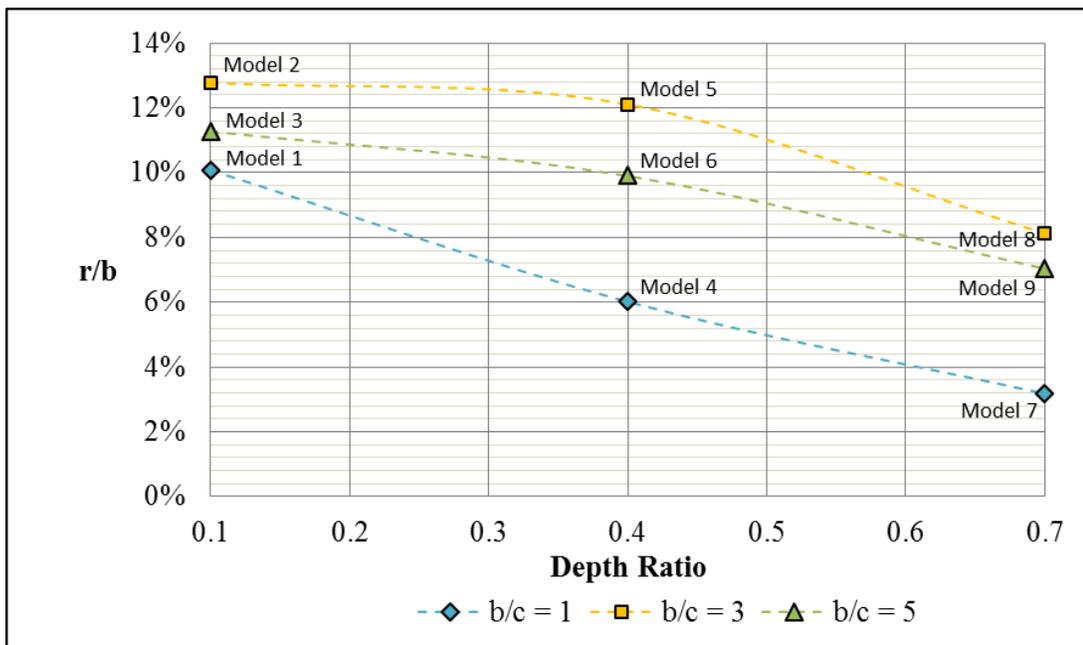
Figure 4.17b Effect of depth ratio (*d/c*) on the eccentricity ratio (*r/b*) for the 45° wind direction and 40 m/s wind speed

4.3   Corner modification

This series of tests investigated the effects of modifying the model by changing the sharp corners to round (Model 10) or chamfered (Model 11) corners. Refer to Table 3.1 for

model dimensions and Figures 3.18, 3.19 and 3.20 for pictures of the test configuration and model setup in the WOW. Testing was performed using the same parameters and conditions as the sharp corner tests. The drag coefficient test results for the modified models are tabulated in Tables 4.8 and 4.9.

Table 4.8 Summary of modified corner results for the 0° wind direction

| Model No. | 0° Wind Direction | | | | | |
| | 15 m/s | | | 40 m/s | | |
	C_{Fx}	C_{Fy}	C_{Fz}	C_{Fx}	C_{Fy}	C_{Fz}
9	1.19	0.00	-0.05	1.22	0.01	0.03
10	0.85	0.03	0.24	1.06	0.04	0.12
11	0.97	0.03	0.04	1.01	0.04	0.12

Table 4.9 Summary of modified corner for the 45° wind direction

| Model No. | 45° Wind Direction | | | | | |
| | 15 m/s | | | 40 m/s | | |
	C_{Fx}	C_{Fy}	C_{Fz}	C_{Fx}	C_{Fy}	C_{Fz}
9	0.89	-0.11	0.02	0.91	-0.11	0.04
10	0.69	-0.07	0.00	0.74	-0.11	0.03
11	0.74	-0.06	0.10	0.72	-0.10	-0.06

Figure 4.18a is a plot of C_{Fx} in the 0° wind direction for the models with modified corners as a function of wind speed. The results for the sharp corner model (Model 9) are included in the graph for comparison. Results show that drag coefficients for models with modified corners are lower than the drag coefficients for the sharp corner models. As outlined by Tamura and Miyagi (1999), this suggests that chamfered and round corners decrease the wake width resulting in reduced drag. At a wind speed of 15 m/s, the drag coefficient decreases in the order of sharp corner, chamfered and round corners. These results agree qualitatively with Tamura and Miyagi (1999) and Yamagishi et al. (2010). The drag coefficient for the chamfered model is 22% smaller than the sharp corner model and the drag coefficient for the round corner model is 40% smaller than the sharp corner model. However, at a wind speed of 40 m/s, Figure 4.18a shows that the drag coefficient decreases in the order of sharp corner, round and chamfered corners. Here the drag coefficient for the round corner model is larger than the coefficient for the chamfered model. The round model is still 16% smaller than the sharp corner model and the drag coefficient for the chamfered is 21% smaller than the sharp corner model. A slight increase in C_{Fx} with wind speed was noted for the sharp and chamfered models. However, C_{Fx} for the round corner model increased significantly which may indicate a possible Re

dependency for the round corner model. The chamfered modification is recommended for wind load mitigation purposes as it has less *Re* dependency and is easier to fabricate.

Figure 4.18b shows results for C_{Fx} in the 45° wind direction. As illustrated, the coefficient for the modified corner models are significantly lower than the sharp corner results for Model 9. Similar to the 0° wind direction, the 45° wind direction coefficient decreases in the order of sharp, chamfered, and round corners for the 15 m/s wind speed test and in the order of sharp, round, and chamfered corners for the 40 m/s wind speed tests.

Figure 4.18a Comparison of sharp (Model 9) and modified corner (Model 10 and 11) results - 0° wind direction
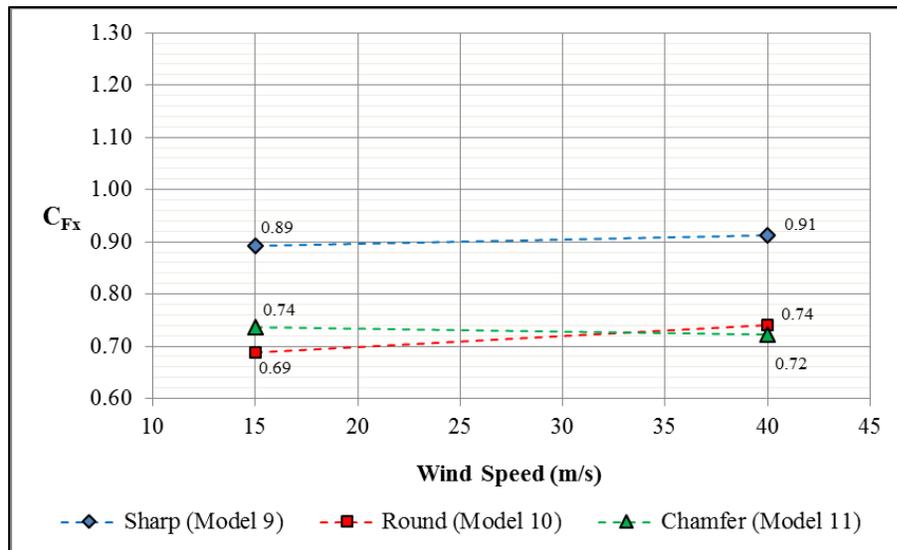
Figure 4.18b Comparison of sharp (Model 9) and modified corner (Model 10 and 11) results - 45° wind direction

4.4 Wind driven rain
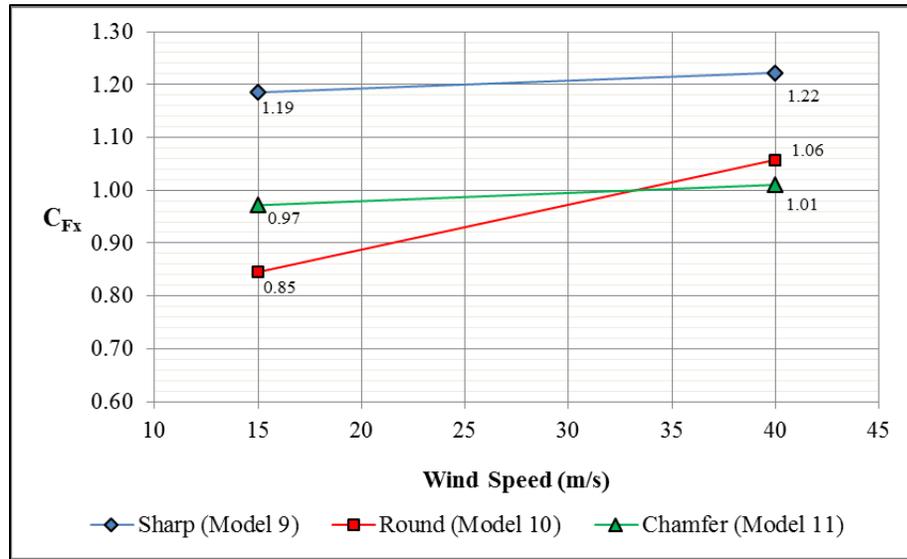
Model 8 (1.8 x 0.6 x 0.4 m) was subjected to a simulated high velocity wind driven rain environment by utilizing spray nozzles mounted on the exhaust side of the WOW fans. The configuration of the wind driven rain test is discussed in Section 3.7.4. This test was only conducted for the 45° wind direction. The measured C_{Fx} for Model 8 with and without wind driven rain was 0.96 and 0.93 respectively for the 15 m/s wind speed. The results for the 40 m/s wind speed were 0.94 and 0.95. It does not appear from this limited testing that wind driven rain has any effect on C_{Fx}.

4.5   Discussion and comparison with previous results

Table 4.10 lists the normal force coefficient results for the 0° horizontal wind approach direction obtained in this study along with results from Letchford (2001), Quinn et al. (2001), Smith et al. (2014), and Zuo et al. (2014). The AASHTO Specification (2013) flat panel and VMS code recommended values are also included. An examination of the results shows good agreement with the wind tunnel results obtained by Zuo et al. (2014) and Smith, et al. (2014). Figure 4.19 graphically compares these results as a function of aspect ratio. As shown in the graph, the flat panel results by Letchford (2001) are larger than the prismatic results obtained in this study and wind tunnel experiments by Zuo et al. (2014). The lower drag coefficient values obtained for prismatic rectangular shapes may be in part due to model thickness and partial reattachment of flow after initial separation from the leading edge of the model. As discussed in Sections 2.1.1, reattachment of flow along the sides of the prismatic shape leads to vortex formation further downstream, a smaller downstream wake region, and a weaker entrainment process resulting in a lower drag coefficient. In addition, the excessive energy content in the high frequency range of Letchford's (2001) wind tunnel ABL simulation may have contributed to the larger results. The partial simulation method used in the WOW ensures that the high frequency spectral content of the WOW flow matches the high frequency portion of the ABL spectrum (see Section 3.4.2). Proper simulation of the high frequency range of the spectrum is critical in the investigation of sharp edge shapes like VMS since small scale high energy fluctuations significantly affect aerodynamic behavior such as local vortex formation, flow separation, and flow reattachment (Fu et al., 2012). Since the current AASHTO Specification (2013) recommended drag coefficient is 1.7, it is suggested that VMS structures designed using these values may be overdesigned and uneconomical.

The drag coefficient result of $C_{Fx} = 1.08$ from Quinn's et al. (2001) full scale study at Silsoe for a sign with $b/c = 1$ and $c/h = 0.32$ is in good agreement with the WOW result for Model 1, 4, and 7 ($C_{Fx} = 1.15, 1.12,$ and 0.98) which have comparable geometry ($b/c = 1$ and $d/c = 0.1, 0.4$ and 0.7). The slightly higher results of the WOW study may be due in part to the smaller clearance ratio (larger gap beneath the sign) of $c/h = 0.24$ used in this study as opposed to $c/h = 0.32$ by Quinn et al. (2001). In addition, the Smith et al. (2014) full scale result of $C_{Fx} = 1.13$ for $b/c = 2$ and $d/c = 0.47$ is in excellent agreement with the interpolated WOW results for Models 4 and 5 which was $C_{Fx} = 1.17$.

71

Table 4.10 Comparison with previous research results for normal force coefficients

Study	Type	Depth Ratio (d/c)	Clearance Ratio (c/h)	Aspect Ratio (b/c)				
				1	2	3	4	5
FIU - Models 1, 2, 3	Large Scale Wind Tunnel	0.10	0.24	1.15	1.19*	1.22	1.25*	1.28
FIU - Models 4, 5, 6	Large Scale Wind Tunnel	0.40	0.24	1.12	1.17*	1.21	1.23*	1.25
FIU - Models 7, 8, 9	Large Scale Wind Tunnel	0.70	0.24	0.98	1.07*	1.16	1.19*	1.22
Zuo (2014) WT	Small Scale Wind Tunnel	0.29	0.50	1.25	-	-	-	-
Zuo (2014) WT	Small Scale Wind Tunnel	0.48	0.50	-	1.22	-	-	-
Zuo (2014) WT	Small Scale Wind Tunnel	0.58	0.50	-	-	-	1.21	-
Zuo (2014) WT	Small Scale Wind Tunnel	0.53	0.50	-	-	-	-	1.27
Smith (2014)	Full Scale	0.47	0.50	-	1.13	-	-	-
Quinn (2001)	Full Scale	Flat Panel	0.32	1.08	-	-	-	-
Letchford (2001)	Small Scale Wind Tunnel	Flat Panel	0.30	1.42	1.45	-	1.53	1.57
Letchford (2001)	Small Scale Wind Tunnel	Flat Panel	0.50	1.38	1.42		1.45	1.44
AASHTO Flat Panel	N/A	All	All	1.12	1.19	-	-	1.2
AASHTO VMS	N/A	All	All	1.70	1.70	1.70	1.70	1.70

* Interpolated results

The measured WOW normal force coefficients for the 45° horizontal wind approach direction were compared to the results obtained by Letchford (2001), Quinn et al. (2001), Ginger et al. (1998), Paulotto et al. (2006) and Zuo et al. (2014). In the WOW study, all normal force coefficient results for the 45° horizontal wind approach direction (except the results for Model 1 which is discussed separately in Section 4.1.3) were lower than the results for the 0° horizontal wind approach direction. This finding is consistent with Ginger et al. (1998), Zuo et al. (2014) and the limited results obtained by Paulotto et al. (2006) but is not consistent with Letchford's (2001) and Quinn's et al. (2001) suggestion that C_{Fx} is independent of the wind approach direction for approach angles between 0° and 45°. However, graphs of Letchford's (2001) drag coefficient results versus wind direction show a significant reduction in the drag coefficient for wind direction angles larger than 45°. Letchford's (2001) result for the wind direction of 45° with $b/c = 2$ and $c/h = 0.5$ is approximately $C_{Fx} = 1.5$, but decreases to approximately $C_{Fx} = 1.1$ at the wind direction of 60°. In Zuo et al. (2014), a graph of drag coefficient versus wind direction shows a significant drop in C_{Fx} for the 45° yaw angle (horizontal wind direction). The reduction increases with increasing wind direction angles up to 90°.

The eccentricity ratios computed in the FIU WOW study were compared to the wind tunnel values from Letchford (2001) and Zuo et al. (2014) and the full scale results from Smith et al. (2014). The eccentricity ratios in this study were mostly below 0.13 and in good agreement with the full scale results obtained by Smith et al. (2014) and Zuo et al. (2014) but considerably lower than the results obtained by Letchford (2001) and the suggested ASCE 7-10 value of 0.2. However, Smith et al. (2014) tested a range of attack angles and the maximum eccentricity ratio occurred around an angle of attack of 70° (200° using the model orientation of Smith et al. 2014). Consequently the FIU WOW results may not be conservative since only the 45° angle of attack was tested.
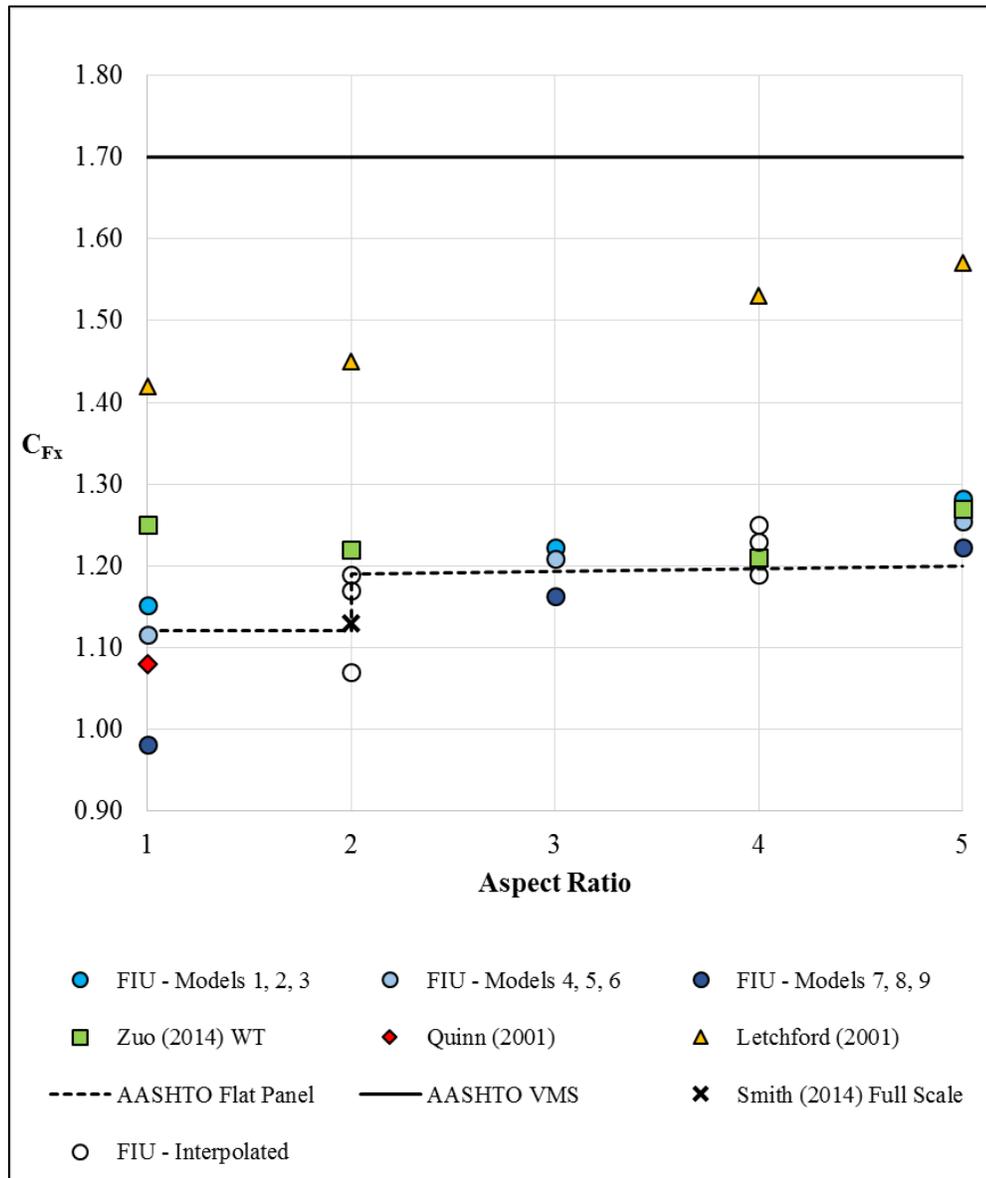
Figure 4.19 Comparison of FIU WOW and past research results for normal force coefficients

In summary, the FIU WOW results are in very good agreement with the full scale tests results by Quinn et al. (2001) and Smith et al. (2014). It is also evident from the results of this study and the wind tunnel results by Zuo et al. (2014) that the drag coefficient values for prismatic signs are lower than the values for flat panels with corresponding aspect and clearance ratios.

5   ASSESSMENT OF AERODYNAMIC INSTABILITY

5.1   Predictions of vortex shedding amplitudes from spectra of lift

Vortices shed from the upper and lower edges of the VMS cause fluctuating forces primarily in the crosswind direction. The simplest theory for predicting vortex excitation assumes the excitation force oscillates in time t in a pure sinusoidal manner, with the excitation force per unit length being given by

$$f(t) = \tfrac{1}{2}\rho U^2 c C_L' \sin \omega_v t \tag{5-1}$$

in which C_L' is a fluctuating "lift coefficient", $c =$ cross-section width normal to wind, and $\omega_v = 2\pi N_v$ and N_v is the shedding frequency of the vortices.

Considering crosswind motions in the direction, z, the deflection $z(y,t)$ of the structure in each of its natural modes of vibration may be expressed as

$$z(y,t) = \phi(y)q(t) \tag{5-2}$$

where $\phi(y) =$ deflection shape of the mode of vibration, and q(t) = generalized coordinate for the mode of vibration. It can then be shown that the equation of motion in a particular mode of vibration is

$$M_G(\ddot{q} + 2\varpi_0 \varsigma \dot{q} + \varpi_0^2 q) = F_G(t) \tag{5-3}$$

where

$$M_G = \text{generalized mass} = \int_0^L m(y)\phi(y)^2 \, dy \tag{5-4}$$

and

$$F_G = \text{generalized aeodynamic force} = \int_0^L f(y,t)\phi(y) \, dy \tag{5-5}$$

where $m =$ mass per unit length, and $L =$ length of structure. As we are assuming, for simplicity, that the force fluctuation is uniform along the length of the structure, Equation 5-5 becomes

$$F_G = \tfrac{1}{2}\rho U^2 C_L' c \times \int_0^L \phi \, dy \times \sin(\omega_v t) \tag{5-6}$$

The solution to Equation 5-3 can be obtained by assuming $q = q_0 sin\,(\omega_v t + \varphi)$ where φ = phase angle, which leads to a predicted maximum response when $\omega_v = \omega_0$, with the amplitude being

$$|q_0| = \frac{\frac{1}{2}\rho U^2 C_L' c \int\limits_0^L \phi\,dy}{\omega_v^2 M_G.2\zeta} \tag{5-7}$$

If the mass distribution is uniform then this becomes

$$|q_0| = \frac{\rho U^2 C_L' c}{4\omega_v^2 m\zeta} \times \frac{\int\limits_0^L \phi\,dy}{\int\limits_0^L \phi^2\,dy} \tag{5-8a}$$

Equation 5-8a implies that if the mode shape ϕ were anti-symmetric, as for a complete sine wave for example, then the response would be zero. In fact, it is found that the rotation of the vortices often is able to switch sign when the mode shape changes sign and a response still occurs. Therefore, recognizing this we replace ϕ in the numerator of Equation 5-8a by its absolute value. Also, we can group the variables into non-dimensional parameters that help in assessing when vortex excitation might be a problem.

$$\frac{|q_0|}{c} = \frac{C_L'}{16\pi^2}\left(\frac{U}{N_v c}\right)^2\left(\frac{\rho c^2}{m\zeta}\right) \times \frac{\int\limits_0^L |\phi|\,dy}{\int\limits_0^L \phi^2\,dy} \tag{5-8b}$$

The parameter $4\pi m\zeta/\rho c^2$ has been named the Scruton number S_c after Scruton, who first identified it as a key parameter by which to assess the susceptibility of a structure to vortex excitation. It has also often been expressed as $2m\delta/\rho c^2$ where δ = the logarithmic decrement, which equals $2\pi\zeta$ for the low values of ζ of interest in wind engineering. The higher the Scruton number the less will be the vortex excitation amplitude. Also, from Equation 5-8b, the parameter $N_v c/U$ is the Strouhal number, S_t. Therefore Equation 5-8b can be expressed as

$$\frac{|q_0|}{c} = \frac{C_L'}{4\pi S_t^2 S_c} \times \frac{\int\limits_0^L |\phi|\,dy}{\int\limits_0^L \phi^2\,dy} \tag{5-8c}$$

From the power spectra of the fluctuating lift obtained on the VMS signs with $d/c = 0.7$ a peak in the excitation spectrum was noted at a non-dimensional frequency $fc/U = 0.10$. This may be identified as the Strouhal number for the VMS signs. The lift coefficients shown in Table 5.1 were determined by measuring the area under the peak from the spectra included in Figure 5.1a, 5.1b, and 5.1c.

Table 5.1 Lift coefficients determined from spectra

b/c	S_t	S_c	C'_L
1	0.10	4.9	0.035
3	0.10	4.9	0.046
5	0.10	4.9	0.052
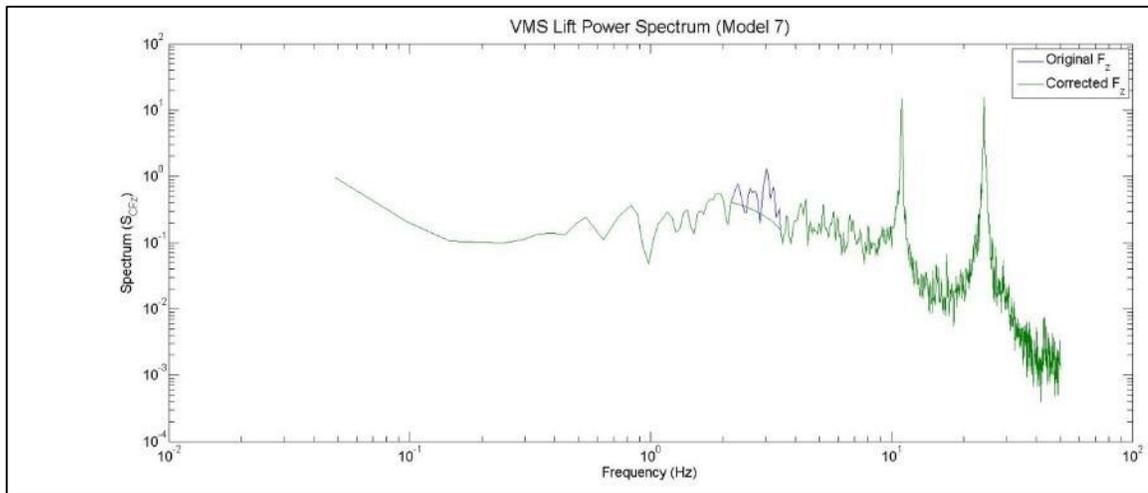
Figure 5.1a VMS lift power spectrum for Model 7
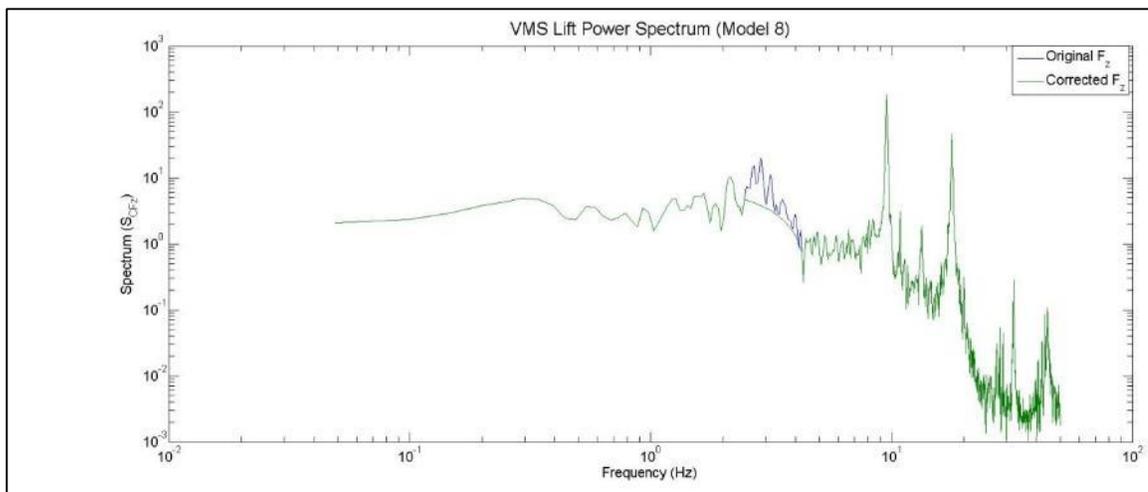
Figure 5.1b VMS lift power spectrum for Model 8

76
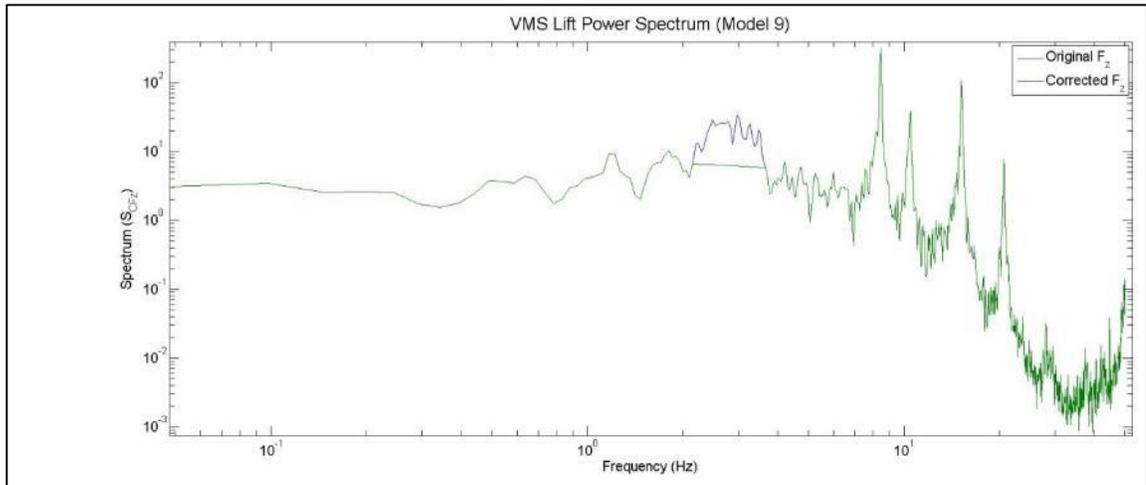
Figure 5.1c VMS lift power spectrum for Model 9

In estimating the Scruton Number S_c the damping ratio was taken as 0.005, the vertical dimension as 1.8 m and the weight per unit length of the VMS as 201 kg/m. The weight of the truss was assumed to be approximately 217 kg/m. As suggested by Ginal (2003), the entire mass of the VMS and 50% of the mass of the truss was used in the calculation. With knowledge of the natural frequency and the inputs in the above table one may then estimate the amplitude of oscillation of the VMS due to vortex excitation using Equation 5-8c. The ratio of integrals in Equation 5-8c was taken to be that for a sinusoid, i.e. $4/\pi \approx 1.27$.

Based on the above calculations, a sign with $c = 1.8$ m and $b = 9.1$ m is predicted to experience vertical sinusoidal oscillations due to vortex shedding with amplitude of about 203 mm. The predicted 3 second gust speeds where oscillations would start to build to the 203 mm amplitude are dependent on the natural frequency of the sign structure in the vertical direction and are plotted in Figure 5.2. Vortex oscillations take some time to build up and the gust speeds plotted here are used only as an indicator of when the accompanying sustained speeds are sufficient to generate oscillations.
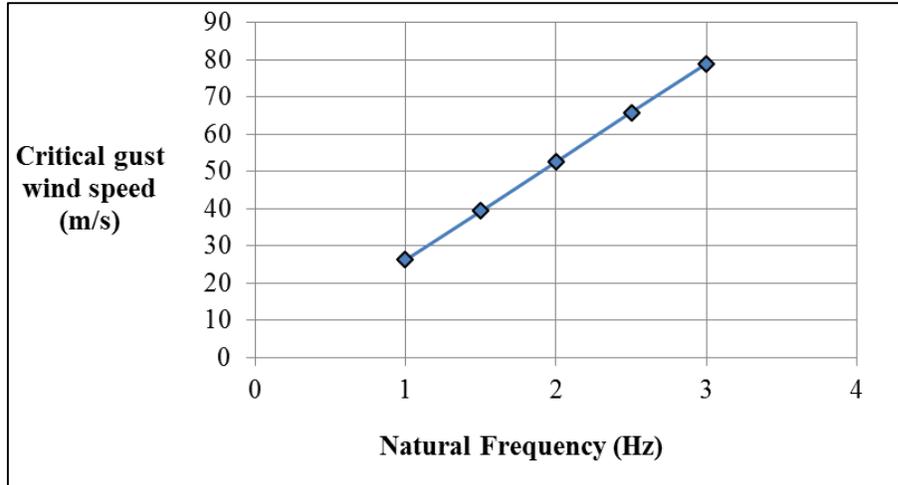
Figure 5.2 Critical gust speeds in winds that will cause vortex shedding oscillations for
$c = 1.8$ m

These results are for $d/c = 0.7$ which is expected to be the worst case, since it has most horizontal area for the vortices to act on. While lift spectra were not obtained for the other d/c values, the vertical excitation forces are expected to be reduced roughly in proportion to the plan area of the sign, i.e. for $d/c = 0.4$ an amplitude of approximately 116 mm would be expected. At $d/c=0.1$ the amplitude is expected to reduce further but the plane area of the support structure would then be comparable to that of the sign so a straight proportional reduction is probably no longer valid.

From the above discussion it can be concluded that significant vortex induced oscillations are possible of VMS with 1.8 m vertical dimension within wind speed ranges of concern if the natural frequency is low.

5.2   Galloping tests

Galloping in the lateral direction for VMS with d/c = 0.7 was investigated. Figures 5.3a and 5.3b are graphs showing the variation of C_L (vertical lift coefficient) and C_D (normal force coefficient) as a function of the wind angle of attack (α). The graphs show that the slope of C_L is negative in the range -4.5°< α < 4.5° for both wind speeds. For the 15 m/s wind speed, the slope of C_L ($dC_L/d\alpha$) is -2.31 and C_D = 1.19 at α = 0°.
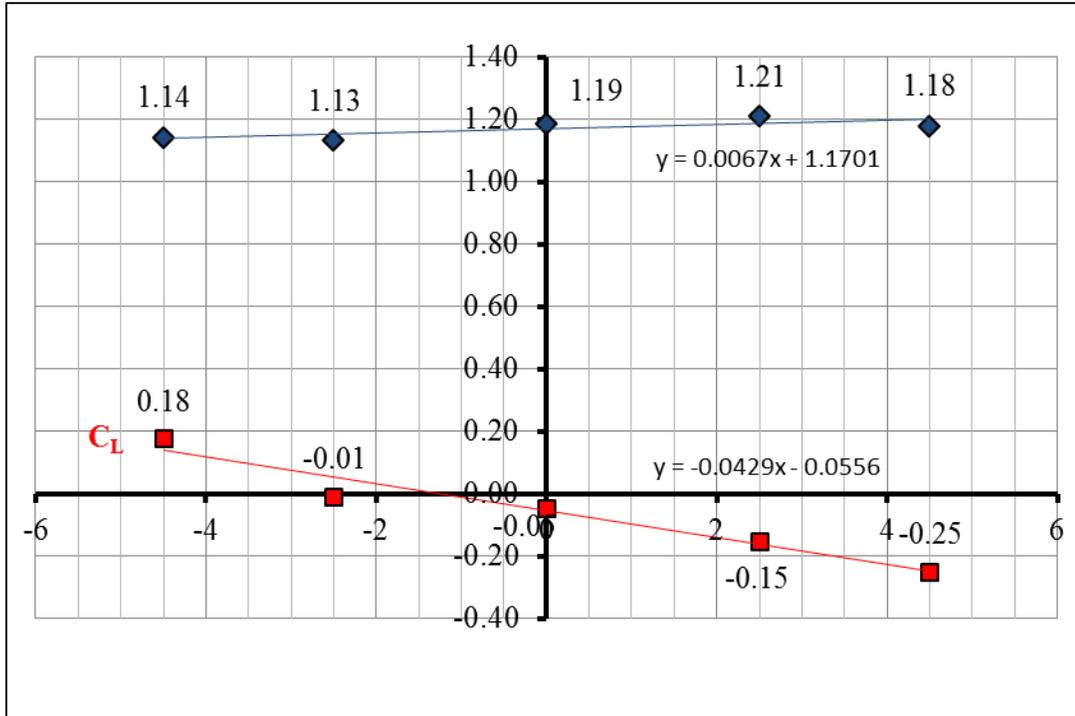
Figure 5.3a Graph of C_D and C_L versus angle of approach – 15 m/s wind speed
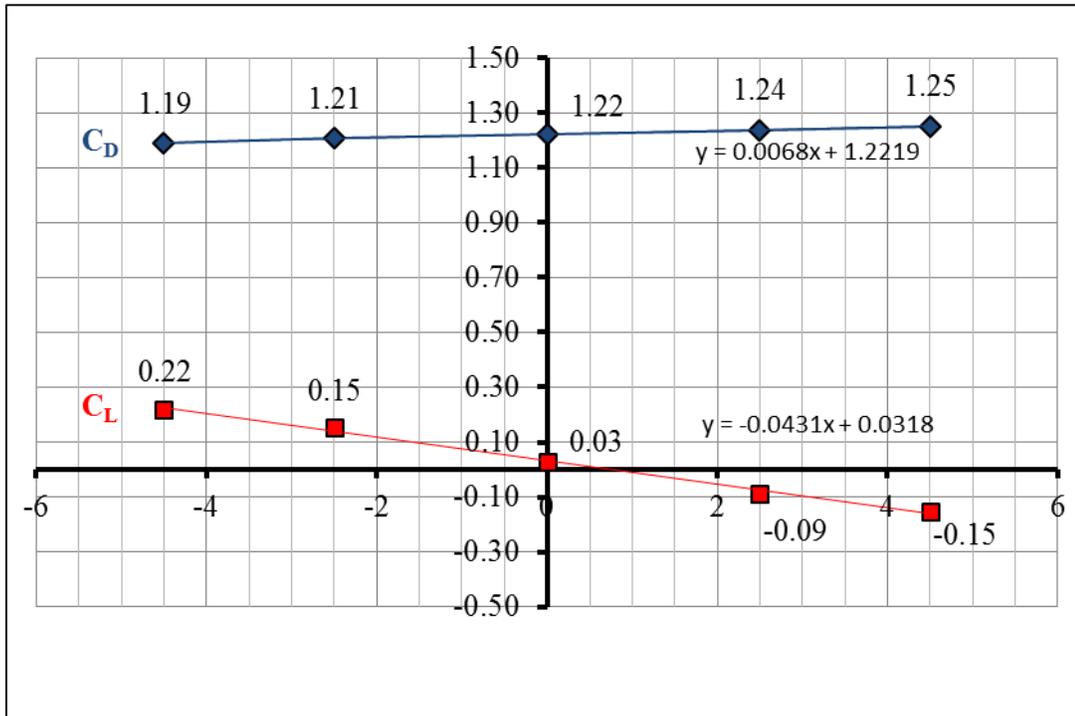
Figure 5.3b Graph of C_D and C_L versus angle of approach – 40 m/s wind speed

Evaluation of the Den Hartog criterion for the 15 m/s wind speed yields

$$\left[\frac{dC_L}{d\alpha} + C_D < 0\right]_{\alpha=0} = -1.12 \tag{5-9}$$

This suggests the model, as configured, is susceptible to galloping. A similar calculation for the 40 m/s wind speed shows that $(dC_L/d\alpha)$ is -2.32 and $C_D = 1.22$ at $\alpha = 0°$. Evaluation of the Den Hartog criterion for the 40 m/s wind speed yields

$$\left[\frac{dC_L}{d\alpha} + C_D < 0\right]_{\alpha=0} = -1.10 \tag{5-10}$$

which also suggests that the model, as configured, is susceptible to galloping.

The critical galloping onset wind velocity (U_{crit}) for a typical span truss VMS support structure was calculated. Starting with the vertical force per unit length being given by

$$Z = \frac{1}{2}\rho U^2 c \frac{dC_Z}{dC_\alpha}\alpha \tag{5-11}$$

and

$$\alpha = -\frac{\dot{q}}{U} \tag{5-12}$$

Therefore

$$Z = -\frac{1}{2}\rho U^2 c \frac{dC_Z}{dC_\alpha}\frac{\dot{q}}{U} \tag{5-13}$$

Assuming the vertical mode of vibration for the structure can be modeled as a SDOF oscillator, the equation of motion including the aerodynamic force in the vertical direction can be written

$$M_G(\ddot{q} + 2\omega_0\varsigma\dot{q} + \omega_0^2 q) = -\int_{sign}\frac{1}{2}\rho U^2 b \frac{dC_Z}{d\alpha}\cdot\frac{\dot{q}}{U}\emptyset^2 dy \tag{5-14}$$

Rearranging the equation and combining the right hand term with the $\dot{q}$ term on the left yields

$$M_G\left(\ddot{q} + 2\omega_0\dot{q}\left(\varsigma + \frac{\rho U\int_{sign}b\frac{dC_Z}{d\alpha}\emptyset^2 dy}{4\omega_0 M_G}\right) + \omega_0^2 q\right) = 0 \tag{5-15}$$

80

The $dC_Z/d\alpha$ term is assumed to be zero along parts of the structure where the VMS is not present. Therefore the integral is only evaluated over the part of the structure where the VMS is present. From Equation 5-15, the total damping of the system becomes

$$\varsigma_{total} = \varsigma + \frac{\rho U \int_0^b c \frac{dC_Z}{d\alpha} \emptyset^2 dy}{4\omega_0 M_G} \qquad (5\text{-}16)$$

Where ς is the structural damping ratio; ρ the density of air; b is the length of the VMS; c is the height of the VMS; $dC_Z/d\alpha$ is the slope of C_Z at 0; ϕ^2 is the modal deflection shape; ω_0 is the natural circular frequency and M_G is the generalized mass.
At critical velocity the total damping of the system is zero,

$$\varsigma + \frac{\rho U_{crit} \int_0^b c \frac{dC_Z}{d\alpha} \emptyset^2 dy}{4\omega_0 M_G} = 0 \qquad (5\text{-}17)$$

Where U_{crit} is the onset wind velocity for galloping. Solving Equation 5-17 for the critical velocity yields

$$U_{crit} = -\frac{4\varsigma\omega_0 M_G}{\rho \int_0^b c \frac{dC_Z}{d\alpha} \emptyset^2 dy} \qquad (5\text{-}18)$$

Since the mass is assumed constant along the length of the VMS, U_{crit} becomes

$$U_{crit} = -\frac{4\varsigma\omega_0 M_G}{\rho bc \frac{dC_Z}{d\alpha} \emptyset^2} \text{ for } \frac{dC_Z}{d\alpha} < 0 \qquad (5\text{-}19)$$

Equation 5-19 was used to estimate the critical galloping onset wind velocity for a typical VMS support structure. The structure consisted of a 3-chord steel truss 1.8 m high x 1.5 m deep with a horizontal truss span of 30.5 m. The weight of the truss was increased 5% to account for the additional weight of connections. A 9.1 m long x 1.8 m high x 1.2 m deep walk-in style VMS was assumed for this calculation. The mass of the VMS was assumed to be 201 kg/m and the mass of the truss (including a catwalk and 5% additional for connections) was assumed to be 217 kg/m. As discussed in Section 5.1, the entire mass of the VMS and 50% of the mass of the truss was used in the critical onset velocity calculation. Damping ratios (ς) from 0.0025 to 0.0075 and natural frequencies (f) from 0.8 to 3.0 were used to cover a wide range of conditions.

Using Equation 5-19 and the parameters in Table 5.2 with $dC_Z/d\alpha = -1.12$, the critical galloping onset wind velocity (U_{crit}) was calculated and graphed in Figure 5.4.

Table 5.2 Parameters for critical galloping onset wind velocity calculation

ρ (kg/m^3)	c (m)	b (m)	Span (m)	m_{VMS} (kg/m)	m_{Truss} (kg/m)	φ	ζ (%)	f (Hz)
1.227	1.8	9.1	30.5	201	217	0.9	0.25 - 0.75	0.8 - 3.0
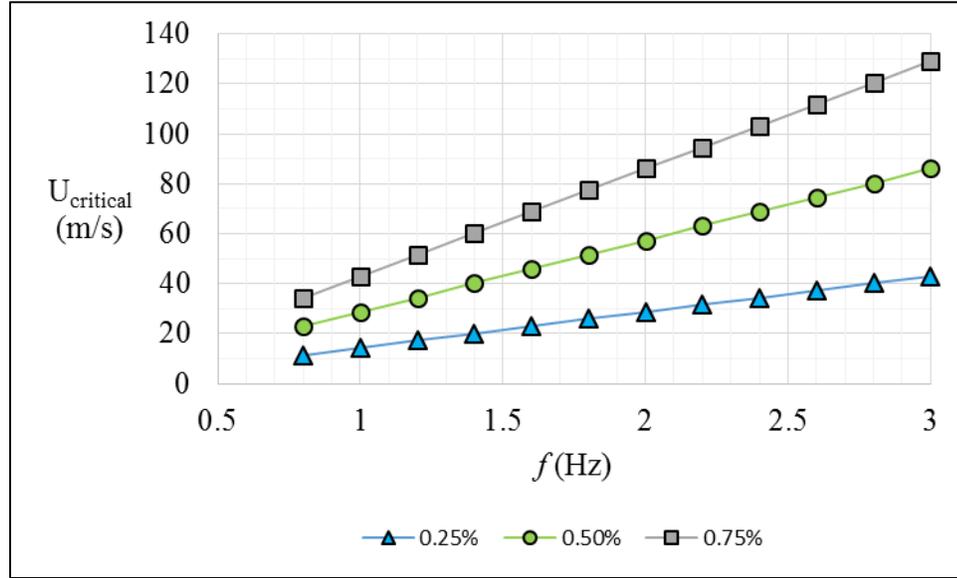
Figure 5.4 Critical galloping onset wind velocity

The U_{crit} calculated for this research are lower than the velocities determined for two span sign structures by Ginal (2003). The details and geometry of Ginal (2003) structures are discussed in Section 2.2.2 but the results are repeated below for reference:

$$98 \text{ m/s} \leq U_{crit} \leq 133 \text{ m/s } (f = 2.4 \text{ Hz}; \zeta = 0.004) \tag{5-20a}$$

$$212 \text{ m/s} \leq U_{crit} \leq 289 \text{ m/s } (f = 6.3 \text{ Hz}; \zeta = 0.004) \tag{5-20b}$$

The lower critical wind speed result for the WOW study was anticipated since according to Parkinson (1963) there is an increased potential for shapes with a longer afterbody length to gallop. This occurs because the afterbody length interferes with the vortex formation in the downstream wake region. Flow that separates from the windward edges can reattach along one side of the afterbody length which leads to an asymmetric surface pressure distribution and a net force in the z-direction. Since the resulting galloping instability is a function of the afterbody length, the results of this study based on $d/c = 0.7$ is expected to be lower than Foley et al. (2004) which was based on $d/c = 0.5$. Since the critical galloping onset wind velocity for structures with low natural frequency and low critical damping is in the range of likely wind speeds experienced in many areas of the country, it is suggested that galloping potential be investigated further and considered in the design of VMS structures.

5.3 Buffeting and aerodynamic damping

Figure 5.5 shows a horizontally aligned long, line-like, flexible structure of length L, width b_1, vertical depth d_1, and mass per unit length $m(y)$, with wind of uniform mean velocity normal to its length. To begin with we assume that b_1 and d_1 are very small relative to L; hence term "line-like". Later we will deal with the fact that they may not be small relative to L. Although the instantaneous turbulence velocities at different points are different, statistically the turbulence is homogeneous along the span. We will make the quasi-steady assumption that the fluctuating wind loads can be determined from the aerodynamic force coefficients measured in steady flow.
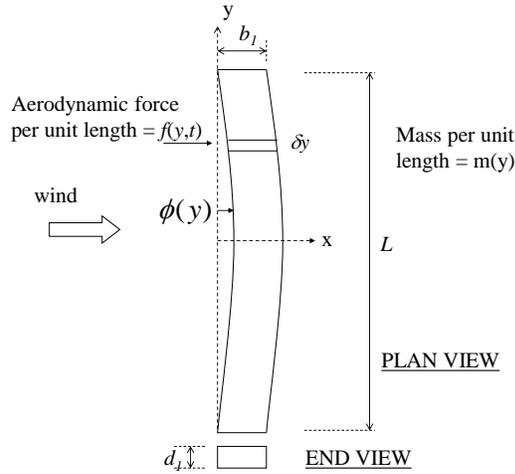
Figure 5.5 Flexible line-like structure

We consider forces and motions in the x direction, which is aligned with the mean wind direction. The deflection $x(y,t)$ of the structure in each of its natural modes of vibration may be expressed as

$$x(y,t) = \phi(y)q(t) \tag{5-21}$$

Where $\phi(y)$ = deflection shape of the mode of vibration, and $q(t)$ = generalized coordinate for the mode of vibration. It can then be shown that the equation of motion in a particular mode of vibration, that has frequency $\bar{\omega}_0$ and damping ratio ζ, is

$$M_G(\ddot{q} + 2\bar{\omega}_0 \zeta \dot{q} + \bar{\omega}_0^2 q) = F_G(t) \tag{5-22}$$

Where

$$M_G = \text{generalized mass} = \int_0^L m(y)\phi(y)^2 \, dy \tag{5-23}$$

and

$$F_G = \text{generalized aeodynamic force} = \int_0^L f(y,t)\phi(y)dy \tag{5-24}$$

where m = mass per unit length and f = force per unit length. Using the quasi-steady assumption, and ignoring second order effects, the equation for the fluctuating aerodynamic force in the along wind direction may be expressed as

$$f(y,t) = \rho U C_{Fx} d_1 . \left(u(y,t) - \dot{x}(y,t)\right) \tag{5-25}$$

where C_{Fx} = aerodynamic drag coefficient. Therefore the generalized aerodynamic force may be written

$$F_G = \int_0^L \rho U C_{Fx} d_1 . \left(u(y,t) - \phi(y)\dot{q}(t)\right)\phi(y)dy \tag{5-26}$$

The term involving $\dot{q}$ may be taken over to the left hand side of Equation 5-22 and combined with the damping term already there. The Equation of motion may then be written as

$$M_G \left(\ddot{q} + 2\varpi_0 \left[\varsigma + \frac{\rho U \int_0^L C_{Fx} d_1 . \phi^2 dy}{2\omega_0 M_G} \right] \dot{q} + \varpi_0^2 q \right) = \rho U \int_0^L C_{Fx} d_1 \phi u \, dy \tag{5-27}$$

In this equation it can be seen that the left hand side is the same as that of Equation 5-22 except that the total damping ratio is now given by the structural damping ratio, ζ plus the aerodynamic damping ratio, ζ_a : i.e.

$$\zeta_{tot} = \zeta + \zeta_a \tag{5-28}$$

where

$$\zeta_a = \frac{\rho U \int_0^L C_{Fx} d_1 . \phi^2 dy}{2\omega_0 M_G} \tag{5-29a}$$

Note that for the case where C_{Fx} and d are constant along the span, and where the mass per unit length m is also constant, this relationship reduces to

$$\zeta_a = \frac{\rho U C_{Fx} d_1}{2\omega_0 m} \tag{5-29b}$$

Using random vibration theory Equation 5-27 may be used to derive the power spectrum of generalized deflection of the structure.

$$S_q(n) = \frac{(\rho U)^2}{M_G^2 \omega_0^4} \left|H(\tfrac{n}{n_0}, \zeta_{tot})\right|^2 S_u(n) \int_0^L \int_0^L C_{Fx} C'_{Fx} d_1 d'_1 \phi \phi' \bar{S}_{uu}(n, y, y') \, dy \, dy' \tag{5-30}$$

in which $\left|H(\tfrac{n}{n_0}, \zeta_{tot})\right|$ is the mechanical admittance given by

$$\left|H(\tfrac{n}{n_0}, \zeta_{tot})\right| \equiv \sqrt{\frac{1}{\left[1_0 - (\tfrac{n}{n_0})^2\right]^2 + 4\zeta_{tot}^2 (\tfrac{n}{n_0})^2}} \tag{5-31}$$

$\bar{S}_{uu}(n, y, y')$ is the cross-spectrum of the velocity fluctuations at locations y and y' along the span, divided by the power spectrum, S_u (which, like the mean velocity and all turbulence statistical properties, is assumed to be homogeneous along the span).

Equation 5-30 was derived on the basis that the dimensions b_1 and d_1 were so small that the turbulence velocity u remains perfectly correlated over these dimensions. In many situations this assumption is somewhat approximate and introduces too much conservatism. To overcome this, a correction can be made by introducing a two dimensional aerodynamic admittance function $\left|\chi_{2D}(n, b_1, d_1)\right|$ that models the lack of correlation over the dimensions b_1 and d_1. With this correction term the power spectrum of deflection becomes

$$S_q(n) = \frac{(\rho U)^2}{M_G^2 \omega_0^4} \left|H(\tfrac{n}{n_0}, \zeta_{tot})\right|^2 S_u(n) \int_0^L \int_0^L C_{Fx} C'_{Fx} d_1 d'_1 \phi \phi' \bar{S}_{uu}(n, y, y') \left|\chi_{2D}(n, b_1, d_1)\right|^2 \, dy \, dy' \tag{5-32}$$

Allowing for the fact that C_x, b_1 and d_1, may vary along the span, Equation 5-32 may be written as

$$S_q(n) = \frac{(\rho U C_{Fx,ref} d_{1ref} L)^2}{M_G^2 \omega_0^4} \left|H(\tfrac{n}{n_0}, \zeta_{tot})\right|^2 \left|\chi_y(n, L)\right|^2 \left|\chi_{2D}(n, b_{1ref}, d_{1ref})\right|^2 S_u(n) \tag{5-33}$$

Where $C_{x,ref}$, b_{1ref} and d_{1ref}, are reference values at a selected location along the span, and

$$\left|\chi_y(n,L)\right|^2 \left|\chi_{2D}(n,b_{1ref},d_{1ref})\right|^2 =$$

$$\frac{1}{L^2}\int_0^L\int_0^L\left(\frac{C_{Fxo}C'_{Fxo}}{C_{Fx,ref}^2}\right)\left(\frac{d_1 d'_1}{d_{1ref}^2}\right)\frac{\left|\chi_{2D}(n,b_1,d_1)\right|^2}{\left|\chi_{2D}(n,b_{1ref},d_{1ref})\right|^2}\phi\phi'\overline{S}_{uu}(n,y,y')\,dy\,dy' \quad \text{(5-34)}$$

Also the aerodynamic damping ratio may be written

$$\zeta_a = \frac{\rho U C_{Fx,ref}d_{1ref}\int_0^L\dfrac{C_{Fx}}{C_{Fx,ref}}\dfrac{d_1}{d_{1ref}}.\phi^2 dy}{2\omega_0 M_G} \quad \text{(5-35)}$$

The variance of generalized deflection may be evaluated by integrating Equation 5-34 over all frequencies. For a lightly damped structure this integration can be simplified considerably by noting that nearly all the contribution to the integral comes from a very narrow range of frequencies close to the natural frequency. This a consequence of the form of the mechanical admittance term $\left|H(\frac{n}{n_0},\zeta_{tot})\right|^2$. As a result we may express the integration of Equation 5-33 as

$$\sigma_q^2(n) = \frac{(\rho U^2 C_{Fx,ref}d_{1ref}LI_u)^2}{M_G^2\omega_0^4}\left(\begin{array}{l}\displaystyle\int_0^\infty\left|\chi_y(n,L)\right|^2\left|\chi_{2D}(n,b_{1ref},d_{1ref})\right|^2 S_u(n)dn + \\[2ex] \left|\chi_y(n_0,L)\right|^2\left|\chi_{2D}(n_0,b_{1ref},d_{1ref})\right|^2\dfrac{n_0 S_u(n_0)}{\sigma_u^2}\dfrac{\pi}{4\zeta_{tot}}\end{array}\right) \quad \text{(5-36)}$$

5.3.1 Gust factor calculation of ASCE 7-10

The general form of Equation 5-36 is reflected in the detailed gust factor calculation for along wind response in ASCE 7-10, with the integral term being the background factor and the last term being the resonant contribution. Empirical expressions have been used in ASCE 7 to account for the aerodynamic admittance terms and simplify the calculation in a convenient fashion suitable for a building code or standard. However, as part of the simplification process, and as a conservative approximation, the aerodynamic contribution to total damping ratio has been omitted in ASCE 7. Although this is a reasonable approach for most large structures, for flexible sign structures this can lead to significant over-estimates of the gust factor.

Therefore, in order to estimate the gust factor for the VMS signs the ASCE 7-10 procedure can be adopted with one modification, which is to add the aerodynamic damping to the structural damping. As can be seen from Equation 5-29a the aerodynamic damping depends on the deflection shape ϕ and generalized mass of the mode of vibration. In

general these will be specific to each sign structure, including the wind drag and mass not only of the sign itself but also of the truss or other structure supporting the sign. However, to provide rough estimates of the contribution of aerodynamic damping to total damping in the present study the following simplifying assumptions have been made.

1. The generalised mass of the entire sign structure, including the sign, is assumed to be the mass of the VMS and 50% of the mass of the truss.

2. The sign is assumed to be located at the point of maximum deflection.

3. The aerodynamic drag forces on the support structure are ignored for the calculation of aerodynamic damping.

The effects of these three assumptions are expected to result in a conservative estimate of the aerodynamic damping.

5.3.2 Estimates of gust factor based on ASCE 7-10 with aerodynamic damping included

Using the ASCE 7-10 formulae for the gust factor, but including the aerodynamic damping term as described above (Equation 5-29b), gust factors were estimated for a selection of sign geometries and weights. These estimates are provided here to give an indication of the sensitivity of the gust factor to size, natural frequency, weight, and wind velocity. The signs selected were as follows.

1. Width b = 9.1 m, height c = 2.4 m, depth d = 1.2 m. Two weights were examined, 201 kg/m and 104 kg/m.

2. A large sign with b = 15.2 m, c = 3.7 m and d = 1.8 m. Two weights were examined, 335 kg/m and 179 kg/m.

3. A small sign with b = 3.7 m, c = 1.8 m and d = 0.9 m. Two weights were examined, 112 kg/m and 60 kg/m.

Figures 5-6 through 5-11 show the behavior of the gust factor plotted versus 3 second reference gust speed for various natural frequencies. The exposure was taken as open terrain (Exposure C of ASCE 7) and the reference wind speed was the standard speed at 10 m height in open terrain. Appropriate adjustments were made to the speed to determine the speed at the mid height of the sign. A representative drag coefficient of 1.25 was used in the calculations. The structural damping ratio was taken to be 0.005 but tended to be far outweighed by the aerodynamic damping at high wind speeds. As a result the gust factor calculations were not overly sensitive to the assumed structural damping.

It can be seen in Figures 5-6 to 5-11 that these rough estimates show a wide range of possible gust factors, some below the existing 1.14 value in AASHTO and some above. For the mid-sized sign at heavier weight, Figure 5-6, and for wind speeds above 45 m/s,

the gust factor G ranges from about 1.07 for a fairly stiff sign with frequency 3 Hz to about 1.34 for a very flexible sign with a low frequency of 1 Hz. For the light-weight mid-sized sign, Figure 5-7, the aerodynamic damping is relatively higher. This reduces the gust factor so that at speeds above 45 m/s it ranges from about 1.00 for the stiffest case (frequency = 3 Hz) to 1.18 for the most flexible (frequency = 1 Hz). The larger sign sees generally lower gust factors, ranging from about 0.95 to 1.24 for speeds above 45 m/s, Figures 5-8 and 5-9. The smallest sign sees the highest gust factors ranging from about 1.11 up to 1.43 at speeds above 45 m/s (Figures 5-10 and 5-11).

Although the scope of the current studies was focused on aerodynamic drag coefficient of VMS signs this preliminary assessment of the gust factor allows some conclusions to be drawn on this other important factor that forms part of the aerodynamic drag calculation. It indicates that gust factors in excess of the standard 1.14 value assumed by AASHTO are possible for the more flexible sign structures. A future, more detailed study of gust factor would be warranted in view of these results.

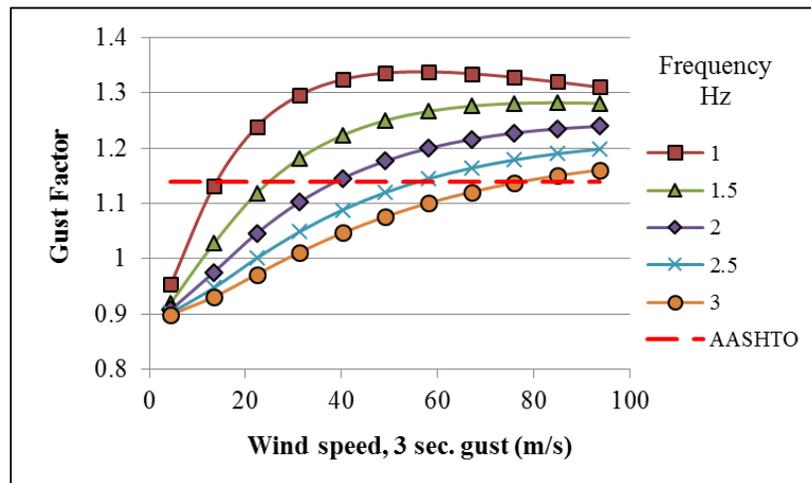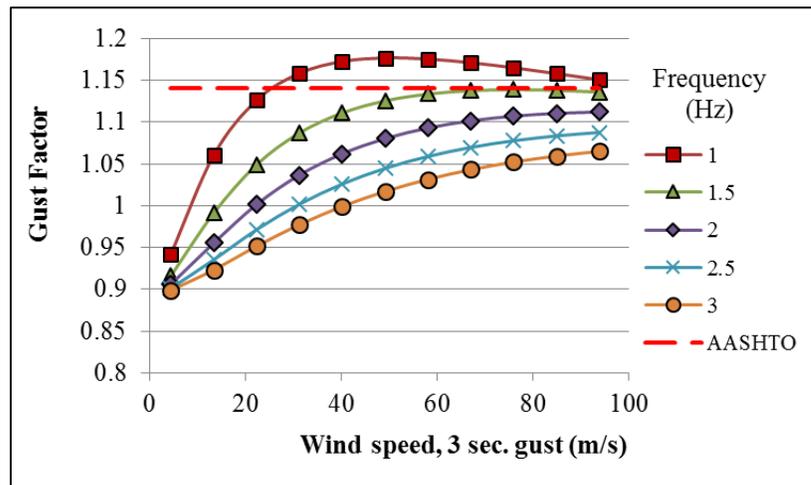Figure 5.6 Estimated gust factor for mid-sized sign (heavier weight)

Figure 5.7 Estimated gust factor for mid-sized sign (lighter weight)
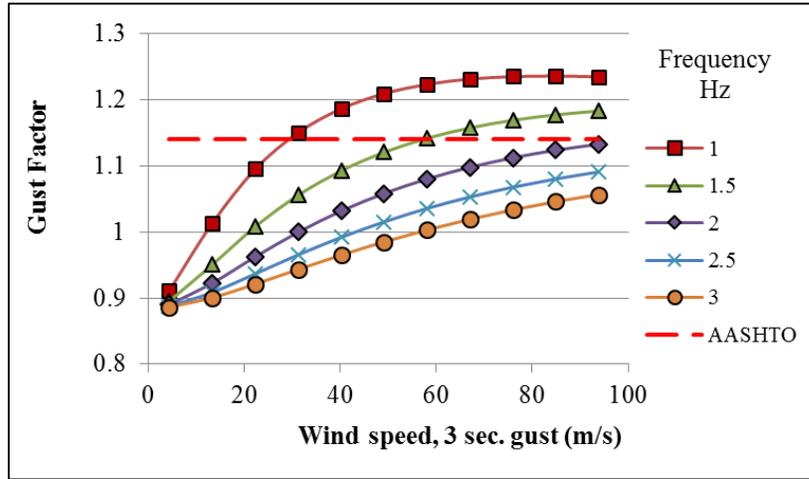

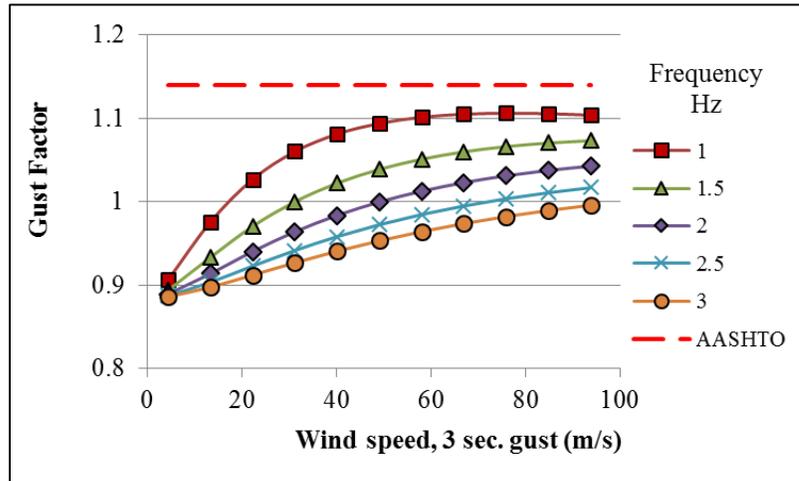Figure 5.8 Estimated gust factor for large sign (heavier weight)

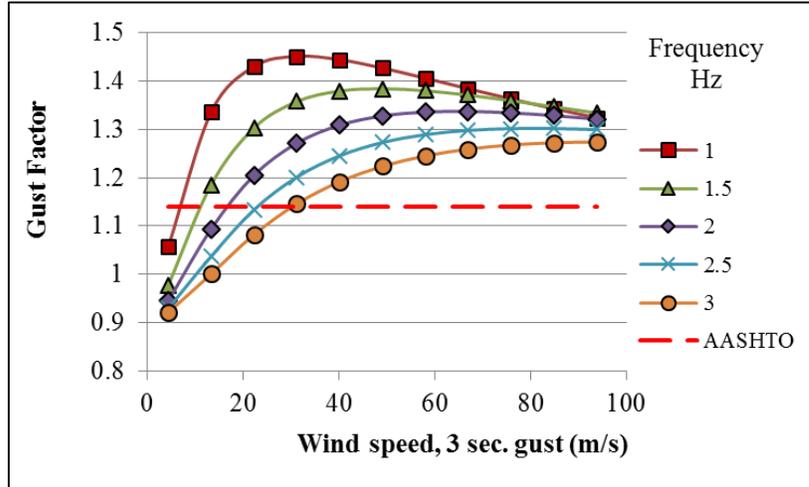Figure 5.9 Estimated gust factor for large sign (lighter weight)

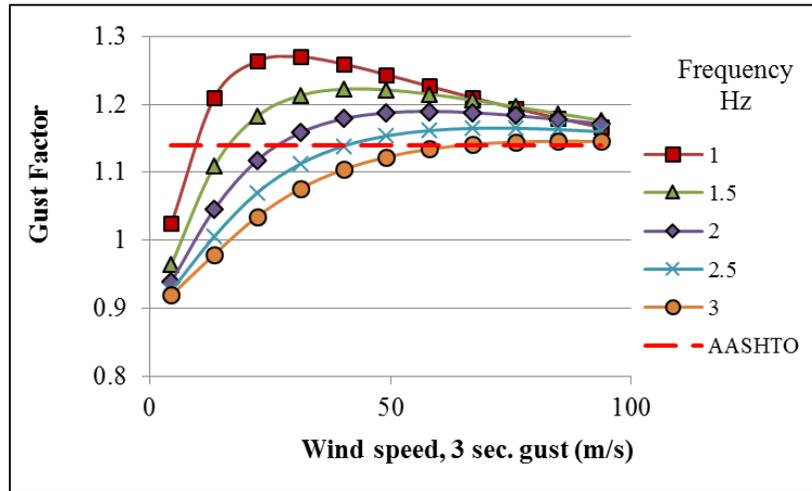Figure 5.10 Estimated gust factor for small sign (heavier weight)

Figure 5.11 Estimated gust factor for small sign (lighter weight)

90

6   DISCUSSIONS AND RECOMMENDATIONS

One objective of this study was to determine accurate drag coefficients for VMS that could be incorporated into the AASHTO Specification. The matrix shown in Table 6.1 is the synthesis of the drag coefficient results from this research. Since no significant difference was noted in the results for the tested fatigue level wind speed of 15 m/s and the extreme event wind speed of 40 m/s, a single design matrix is suggested for use in both fatigue and strength design. The C_{Fx} values are based on the results obtained for the 40 m/s wind speed in the 0° horizontal wind direction since these values were slightly larger than the values obtained for the 15 m/s wind speed. The one noted exception is the value for b/c = 1 with d/c = 0.1. The value of C_{Fx} = 1.21 is a rounded value that takes into account the large result obtained for the geometric configuration of Model 1 in the 45° horizontal wind direction. Intermediate values for b/c = 2 and 4 and d/c = 0.2, 0.3, 0.5, and 0.6 were interpolated from actual tested geometric configurations.

Table 6.1 Drag Coefficient design matrix for C_{Fx}

Aspect Ratio (b/c)	Depth Ratio (d/c)						
	0.1	0.2	0.3	0.4	0.5	0.6	0.7
1.0	1.21	1.18	1.15	1.12	1.08	1.04	0.98
2.0	1.21	1.20	1.18	1.17	1.14	1.11	1.09
3.0	1.22	1.22	1.22	1.21	1.20	1.18	1.16
4.0	1.25	1.25	1.24	1.24	1.23	1.22	1.21
5.0	1.28	1.27	1.26	1.25	1.24	1.23	1.22

The maximum value of the eccentricity ratio (r/b) obtained in the WOW study was 0.13. This value is in good agreement with the r/b ratios obtained by Smith et al. (2014) which were less than 0.15. Based on these results, an r/b value of 0.15 is recommended for use in design. However, it is important to note that the current AASHTO Specification (2013) does not include a recommendation for r/b.

Another objective of this study was to estimate gust effect factors and recommend drag force evaluation methodology. Although the findings of the study are limited, preliminary results indicate that gust factors in excess of the AASHTO Specification (2013) suggested value of 1.14 are possible for flexible sign structures. Additional research is suggested to explore this finding in more detail to see if a change to the current 1.14 value is warranted.

The dynamic analysis conducted as part of this research indicates that VMS signs with a large depth ratio attached to structures with a low natural frequency may be susceptible to vortex shedding and galloping when subjected to a range of likely expected wind speeds. Based on these findings, it is suggested that the AASHTO design procedure be expanded to evaluate VMS structures for vortex shedding and galloping potential. In addition, a recent review and experiments conducted by Mannini et al. (2014) further supports the notion that elongated shapes such as VMS may be susceptible to aeroelastic instability.

The study indicates that both vortex induced vibration and galloping are possible for elongated prismatic shapes with dimensions similar to VMS (large depth ratios) and that a strong interaction between the two phenomena may arise for a range of Kármán vortex resonance and galloping wind speeds that are consistent with the estimated parameters and wind speeds obtained in the FIU WOW study. It is therefore suggested that future research is conducted using a dynamic rig to investigate this interaction further.

7   CONCLUSIONS AND FUTURE RESEARCH

7.1   Summary of findings

The increasing national interest in ITS and the need for more efficient transportation systems have led to an expanding use of VMS technology. This necessitated an evaluation of the current design criteria and code guidance for VMS. The FIU WOW study investigated wind effects on VMS, focusing specifically on wind induced drag and the response of VMS. The research included a comprehensive literature review, investigation of industry specifications, testing of large scale VMS models, extensive data analysis, and discussion of results.

Drag coefficients were obtained for thirteen models at wind speeds of 15 m/s and 40 m/s in horizontal wind directions of 0° and 45°. Based on the extensive large scale testing in the WOW, several conclusions were drawn regarding wind induced drag on VMS. The drag coefficient results in the FIU WOW study are generally in good agreement with the results obtained in full scale studies such as the ones conducted by Quinn et al. (2001) at Silsoe and Smith et al. (2014) at the Reese Technology Center in Texas. A comparison of results for full scale and small scale drag coefficients shows that the values obtained in small scale wind tunnel studies were generally larger. It was suggested that this may be in part due to excessive energy content in the high frequency range of the wind tunnel ABL simulation. The WOW testing confirmed that the prismatic geometry of a VMS can significantly affect wind loading. A comparison of the FIU WOW results with earlier flat panel results suggests that the normal force coefficient for prismatic signs such as VMS is lower than the drag coefficients obtained for flat panel signs. Consequently, the FIU WOW results are lower than the AASHTO Specification (2013) recommended value of 1.7.

Testing also revealed trends in the drag coefficients based on aspect ratio, depth ratio, and wind direction. It was demonstrated that the drag coefficient increases with increasing aspect ratio which is consistent with the results from Letchford (2001) and Zuo et al. (2014). It was also shown that the drag coefficient decreases with increasing depth ratio resulting in a reduced drag force and a smaller drag coefficient for VMS. Wind direction results for the 45° horizontal wind direction were considerably less than the results obtained in the 0° direction (except for Model 1 which is discussed in Section 4.1.3). This finding was consistent with the studies conducted by Zuo et al. (2014), Ginger (1998), and Paulotto (2006) but inconsistent with trends noted in the studies by Letchford (2001) and Quinn (2001).

The effect of corner modification was investigated by testing models with chamfered and round corners. Chamfered corner tests demonstrated an additional decrease in the drag coefficient resulting in a drag coefficient value around $C_{Fx} = 1.00$. This minor modification in manufacturing could have a significant impact on VMS wind loading and lead to more efficient structure designs. Results from the round corner tests indicated a possible Reynolds number dependency.

The maximum value obtained for the non-dimensional eccentricity ratios for the 45° wind direction (r/b = 0.13) was lower than the ASCE 7-10 suggested value of 0.2. The FIU WOW results are in good agreement with the study conducted by Zuo et al. (2014) which also reported eccentricity ratios below 0.15. However, eccentricity is not currently considered in the AASHTO Specification (2013) design procedure.

Wind driven rain results were compared to the wind only results for the same model. Based on the limited testing conducted as part of this study, it does not appear that drag on VMS is affected by wind driven rain in the Reynolds number test range of 5.96 x 10^5 to 1.59 x 10^6.

Vortex shedding of a typical VMS with d/c = 0.7 was investigated by analyzing the power spectra of the fluctuating lift measured in the WOW. Vertical oscillations with an amplitude of about 203 mm was predicted when 3 second gust speeds are as low as 26 m/s for structures with a natural frequency of 1 Hz. Since this is in the range of likely wind speeds, further experimental confirmation is suggested. Galloping instability of a model with b/c = 5 and d/c = 0.7 was investigated experimentally and analyzed using basic galloping theory. Evaluation of the Den Hartog criterion suggested that the model as configured is susceptible to galloping. Based on this finding, galloping is possible for VMS with a large depth ratio attached to a flexible structure with a low natural frequency. It is suggested that galloping potential for VMS structures should be investigated further. Gust factors were estimated for a selection of sign geometries and weights using the ASCE 7-10 formula including the aerodynamic damping term. This was done to provide an indication of the sensitivity of the gust factor to size, natural frequency, weight, and wind velocity. Results showed a wide range of possible gust factors, both above and below the current AASHTO Specification (2013) value of 1.14. Based on this preliminary assessment, gust factors in excess of 1.14 are possible for the more flexible sign structures and warrant a more detailed study.

An alternative to the AASHTO drag coefficient value of 1.7 was presented in the form of a design matrix (see Table 6.1). However a single representative value of C_{Fx} = 1.25 may be used. It is important to note that the current AASHTO Specification (2013) does not provide guidelines for aeroelastic behavior which can lead to unsafe designs for very flexible VMS.

7.2   Recommendations for future research

Based on the findings of this study, future research and testing may include:

- Comprehensive large scale testing of additional VMS geometries and configurations. This should include a more inclusive range of horizontal wind directions (0° to 180°) and a representative range of clearance ratios.

- Finite element modeling of typical VMS structures using the new FIU WOW drag coefficients. This should include dynamic analysis to evaluate the susceptibility of VMS to aeroelastic instabilities.

- Additional large scale wind tunnel testing to evaluate the sensitivity of VMS structures to galloping and vortex shedding. Testing should include a larger range of attack angles and VMS geometries.

- Comprehensive wind tunnel testing of various corner modifications. Testing should evaluate various sizes and additional shape options. The use of rounded corners should be investigated further.

- The results for the square VMS in the 45° horizontal wind direction needs to be investigated in more detail. Although the large results for Model 1 in the 45° wind direction were obtained in preliminary testing and again during final testing, the magnitude of the difference with the 0° wind direction was not anticipated.

- Full scale sectional models of VMS structures should be tested in the wind tunnel to investigate fluctuating lift and shed more light on the potential for aeroelastic instabilities. Use of innovative dampers can be investigated at full scale to reduce potential aeroelastic instabilities.

- Further investigation of the gust effect factor should be carried out.

- Field measurements should be performed to facilitate comparison of wind induced responses to the wind tunnel results for both fatigue and ultimate conditions.

REFERENCES

American Association of State Highway and Transportation Officials. 2001. Standard Specification for Structural Supports for Highway Signs, Luminaires, and Traffic Signals. Washington, D.C.

American Association of State Highway and Transportation Officials. 2009. Standard Specification for Structural Support for Highway Signs, Luminaries, and Traffic Signals. Washington, DC.

American Association of State Highway and Transportation Officials. 2013. Standard Specifications for Structural Support for Highway Signs, Luminaires, and Traffic Signals. Washington, DC.

American Society of Civil Engineers. 1995. Minimum Design Loads for Buildings and Other Structures. New York, NY.

American Society of Civil Engineers. 2010. Minimum Design Loads for Buildings and Other Structures. New York, NY.

Bearman, P.W., and D.M. Trueman. 1972. "An investigation of the flow around rectangular cylinders." Aeronautical Quarterly 229-237.

Bearman, P.W., and D.M. Trueman. 1972. "An investigation of the flow around rectangular cylinders." Aeronautical Quarterly 23 229-237.

Blevins, R.D. 1977. Flow induced vibration. New York: Van Nostrand Reinhold Company.

Bosch, H.R., and R.M. Guterres. 2001. "Wind tunnel experimental investigation on tapered cylinders for highway support structures." Journal of Wind Engineering 1311-1323.

Consolazio, Gary R., Kevin W. Johns, and Robert J. Dexter. 1988. Fatigue performance of variable message sign & luminaire support structures volume ii - fatigue testing and failure analysis of aluminum luminaire support structures. Trenton: New Jersey Department of Transportation.

Cook, Ronald A., David Bloomquist, and Angelica M. Agosta. 1994. "Truck-induced dynamic wind loads on variable-message signs." Transportation Research Record 187-193.

Cruzado, Hector J. 2007. "Risk assessment model for wind-induced fatigue failure of cantilever traffic signal structures." Dissertation, Civil Engineering, Texas Tech University, 217.

D'Auteuil, Annick. 2006. "Aerodynamic behavior of rectangular prisms with sharp edges at high Reynolds number." MS Thesis, Ottawa.

Dexter, R.J., and M.J. Ricker. 2002. NCHRP Report 469: Fatigue-resistant design of cantilever signal, sign, and light supports. University of Minnesota, Washington, D.C.: Transportation Research Board, 111.

Dyrbye, C., and S.O. Hansen. 1997. Wind loads on structures. Chichester: John Wiley & Sons, Ltd.

Fisher, J.W., A. Nussbaumer, P.B. Keating, and B.T. Yen. 1993. NCHRP Report 354: Resistance of welded details under variable amplitude long-life fatigue loading. Washington, D.C.: TRB, National Research Council.

Florea, Micah J., Lance Manuel, Karl H. Frank, and Sharon L. Wood. 2007. Field tests and analytical studies of the dynamic behavior and the onset of galloping in traffic signal structures. Technical Report, Center for Transportation Research, University of Texas, Austin, Austin, TX: Texas Department of Transportation, 128.

Florida Department of Transportation (2013) Span overhead sign program (version 6) [computer software] available from http:// www.dot.state.fl.us/structures/ProgLib.shtm.

Foley, Christopher M., Baolin Wan, Mathew Welglarz, Matthew Hellenthal, Jordan Komp, Andrew Smith, and Joseph P. Schmidt. 2008. Fatigue risks in the connections of sign support structures - phase 1. Technical Report, Department of Civil & Environmental Engineering, Marquette University, Madison, WI: Wisconsin Department of Transportation.

Foley, Christopher M., Raymond A. Fournelle, Scott J. Ginal, and John L. Peronto. 2004. Structural analysis of sign bridge structures and luminaire supports. Technical Report, Department of Civil & Environmental Engineering, Marquette University, Madison: Wisconsin Department of Transportation, 243.

Fouad, Fouad H., and Elizabeth A. Calvert. 2001. Evaluating the design safety of highway structural supports. Technical Report, Department of Civil & Engineering, University of Alabama at Birmingham, Tuscaloosa, AL: University Transportation Center for Alabama.

Fouad, Fouad H., James S. Davidson, Norbert Delatte, Elizabeth A. Calvert, Shen-En Chen, Edgar Nunez, and Ramy Abdalla. 2003. NCHRP Report 494: Structural supports for highway signs, luminaires, and traffic signals. Technical Report, University of Alabama at Birmingham, Washington, D.C.: Transportation Research Board, 59.

Fu, T.C. 2013. "Development of effective approaches to the large-scale aerodynamic testing of low-rise buildings." PhD Thesis, Civil Engineering, Florida International University.

Fu, T., A.M. Aly, A.G. Chowdhury, G. Bitsuamlak, D. Yeo, and E. and Simiu. 2012. "A proposed technique for determining aerodynamic pressures on residential homes." Wind and Structures 15 27-41.

Gerrard, J.H. 1966. "The mechanics of the formation region of vortices behind bluff bodies." Journal of Fluid Mechanics 25: 401-413.

Giannoulis, A., T. Stathopoulos, D. Briassoulis, and A. Mistriotis. 2012. "Wind loading on vertical panels with different permeabilities." J. Wind Eng. Ind. Aerodyn. 1-16.

Ginal, Scott. 2003. Fatigue performance of full-span sign support structures considering truck-induced gust and natural wind pressures. PhD Thesis, Milwaukee: Marquette University.

Ginger, J.D., G.F. Reardon, and B.L. Langtree. 1998. "Wind loads on hoardings and fences." Technical Report, Cyclone Structural Testing Station James Cook University.

Holmes, John D. 2001. Wind loading of structures. London: Spon Press.

Irwin, Peter A. 1998. "The role of wind tunnel modelling in the prediction of wind effects on bridges." Proceedings of the International Symposium Advances in Bridge Aerodynamics, Copenhagen, Balkema, Rotterdam, 99-117.

Irwin, Peter A. 2008. "Bluff body aerodynamics in wind engineering." J. Wind Eng. Ind. Aerodyn. 701-712.

Kacin, Jennifer A. 2007. Fatigue life estimation of a highway sign structure. PhD Thesis, Pittsburgh: University of Pittsburgh.

Kaczinski, M.R., and R.J. Dexter. J.P. Van Dien. 1998. NCHRP Report 412: Fatigue-resistant design of cantilevered signal, sign and light supports. Technical Report, Lehigh University, Washington, D.C.: Transportation Research Board, 266.

Laneville, A., and L.Z. Yong. 1983. "Mean flow patterns around two-dimensional rectangular cylinders and their interpretation." J. Wind Eng. Ind. Aerodyn. 387-398.

Laneville, A., S. Gartshore, and G.V. Parkinson. 1975. "An explanation of some effects of turbulence on bluff bodies." Wind Effects on Buildings and Structures. London: Syndics of the Cambridge University Press. 333-341.

Larose, G.L., and A. D'Auteuil. 2008. "Experiments on 2D rectangular prisms at high Reynolds numbers in a pressurized wind tunnel." J. Wind Eng. Ind. Aerodyn. 923-933.

Letchford, C.W. 2001. "Wind loads on rectangular signboards and hoardings." J. Wind Eng. Ind. Aerodyn 135-151.

Li, Q.S., and W.H. Melbourne. 1999. "The effect of large-scale turbulence on pressure fluctuations in separated and reattaching flows." J. Wind Eng. Ind. Aerodyn. 159-169.

Lundgren, H.R. 1989. Evaluation of monotube sign support structure. Report No. FHWA AZ89-829, Arizona Department of Transportation.

Martin, Kipp A., Mohammad R. Ehsani, Reidar Bjorhovde. 1987. "Field testing of highway sign support structures." Journal of Structural Engineering (ASCE) 113 (4): 850-863.

McDonald, J.R., Mehta, K.C., Oler, W. and Pulipaka, N. 1995. Wind effects on signs, luminaires, and traffic signal structures. Technical Report No. 1303-F, Wind Engineering Research Center, Texas Tech University, Austin, TX: Texas Department of Transportation.

McLean, T. Weston, and J. Michael Stallings Jong Sup Park. 2004. Fatigue evaluation of two variable message sign structures. Montgomery: Alabama Department of Transportation.

Mooneghi, Maryam Asghari, Peter Irwin, and Arindam Gan Chowdhury. 2014. "Large-scale testing on wind uplift of roof pavers." J. Wind Eng. Ind. Aerodyn. 128 22-36.

Nakaguchi, H., Hashimoto, K., Muto, S. 1968. "An experimental study on the aerodynamic drag of rectangular cylinders." J. Japan Soc. Aeronaut. Space Sci. 16: 1-5.

Nakamura, Y., and Y. Ohya. 1984. "The effects of turbulence on the mean flow past two-dimensional rectangular cylinders." Journal of Fluid Mechanics 255-273.

Novak, M. 1972. "Galloping oscillations of prismatic structures." Journal of Engineering Mechanics Division (ASCE) 98: 27-46.

Ocel, Justin M., Robert J. Dexter, and Jerome F. Hajjar. 2006. Fatigue-resistant design for overhead signs, mast-arm signal poles, and lighting standards. Technical Report No. MN/RC-2006-07, Department of Civil Engineering, University of Minnesota, St. Paul: Minnesota Department of Transportation.

Park, Jong Sup, and J. Michael Stallings. 2006. "Fatigue evaluations of variable message sign structures based on AASHTO Specifications." KSCE Journal of Civil Engineering 207-217.

Parkinson, G.V. June 1963. "Aeroelastic galloping in one dimension of freedom." International Conference on Wind Effects on Buildings and Structures. Teddington, UK. 26-28.

Parkinson, Geoffrey. 1989. "Phenomena and modelling of flow-induced vibrations of bluff bodies." Progress in Aerospace Sciences 26 (2): 169-244.

Paulotto, Carlo, and Giuliano Augusti Marcello Ciampoli. 2006. "Wind tunnel evaluation of mean wind pressure on a frame-type signboard." J. Wind Eng. Ind. Aerodyn. 94: 397-413.

Pulipaka, Narendra, Partha P. Sarkas, and James R. McDonald. 1998. "On galloping vibration of traffic signal structures." J. Wind Eng. Ind. Aerodyn. 77 & 78: 327-336.

Quinn, A.D., C.J. Baker, and N.G. Wright. 2001. "Wind and vehicle induced forces on flat plates - Part 1: wind induced force." J. Wind Eng. Ind. Aerodyn. 817-829.

Sitheeq, M. Mohamed, Arun K.S. Iyengar, and Cesar Farell. 1997. "Effect of turbulence and its scales on the pressure filed on the surface of a three-dimensional square prism." J. Wind Eng. Ind. Aerodyn. 461-471.

Smith, Douglas A., Delong Zuo, and Kishor C. Mehta. 2014. "Characteristics of net force and torques on a rectangular sign measured in the field." Manuscript submitted for publication (Unpublished manuscript).

Sohankar, A. 2008. "Large eddy simulation of flow past rectangular-section cylinders: side ratio effects." J. Wind Eng. Ind. Aerodyn. 640-655.

Sohankar, A., C. Norberg, and L. Davidson. 1999. "Simulation of unsteady 3D flow around a square cylinder at moderate Reynolds number." 11 (2): 288-306.

South, Jeffrey M. 1994. Fatigue Analysis of Overhead Sign and Signal Structures. Technical Report No. FHWA/IL/PR-115, Bureau of Materials and Physical Research, Illinois Department of Transportation, Springfield: Illinois Department of Transportation, 118.

Tamura, Tetsuro, and Tetsuya Miyagi. 1999. "The effect of turbulence on aerodynamic forces on a square cylinder with various corner shapes." J. Wind Eng. Ind. Aerodyn. 135-145.

Tieleman, H.W. 1992. "Problems associated with flow modeling procedures for low-rise structures." J. Wind Eng. Ind. Aerodyn. 42: 923-934.

Tieleman, H.W.., and R.E. Atkins. 1990. "Effect of incident turbulence on pressure distributions on rectangular prisms." J. Wind Eng. Ind. Aerodyn. 36: 579-588.

Yamagishi, Y., S. Kimura, and Makoto Oki. 2010. "Flow characteristics around a square cylinder with changing chamfer dimensions." Journal Visualization 13: 61-68.

Yen, Shun C., and Chen W. Yang. 2011. "Flow patterns and vortex shedding behavior behind a square cylinder." J. Wind Eng. Ind. Aerodyn. 868-878.

Yeo, D., and Chowdhury, A.G. 2013. "Simplified wind flow model for the estimation of aerodynamic effects on small structures." J. Eng. Mech. 139: 367-375.

Zuo, Delong, and Christopher Letchford. 2008. Investigation of Wind-Induced Highway Lighting Pole Vibration Using Full-Scale Measurement. Technical Report No. FHWA/TX-08-0-4586-5, College of Engineering, Texas Tech University, Austin, Texas: Texas Department of Transportation.

Zuo, Delong, Douglas A. Smith, and Kishor C. Mehta. 2014. "Experimental study of wind loading of rectangular sign structures." J. Wind Eng. Ind. Aerodyn. 130 62-74.

APPENDICES

Appendix A – Load Cell Calibration Matrices

JR3
Multi-Axis Load Cell Technologies

FORCE-MOMENT SENSOR
SPECIFICATION SHEET

75E20S4-M125D-AF 1350L

Serial Number 4541

Analog calibration.

	Electrical Load Settings	Sensor Load Ratings	Calibration Loads used
Fx	1,350 lbs	1,350 lbs	400 lbs
Fy	1,350 lbs	1,350 lbs	400 lbs
Fz	1,500 lbs	2,700 lbs	400 lbs
Mx	6,000 in-lbs	10,125 in-lbs	2,600 in-lbs
My	6,000 in-lbs	10,125 in-lbs	2,600 in-lbs
Mz	3,000 in-lbs	10,125 in-lbs	2,600 in-lbs

Calibration Matrix: Multiply the calibration matrix and the sensor
Voltage vector to determine the loads.   (lb and in-lbs)

$$
\begin{bmatrix}
267.26 & -1.67 & -0.62 & -4.88 & 4.00 & -1.68 \\
-0.78 & 269.98 & 1.41 & -1.46 & -14.34 & -0.22 \\
2.68 & -8.55 & 295.98 & 1.84 & -0.02 & -8.23 \\
23.09 & -42.46 & 2.29 & 1202.55 & 3.23 & 2.24 \\
-2.98 & 26.82 & -0.94 & -0.73 & 1207.56 & 4.08 \\
-9.90 & 12.21 & 18.09 & -2.13 & -9.35 & 603.50
\end{bmatrix}
\begin{bmatrix}
\text{Fx Volts} \\
\text{Fy Volts} \\
\text{Fz Volts} \\
\text{Mx Volts} \\
\text{My Volts} \\
\text{Mz Volts}
\end{bmatrix}
$$

Color		
Brn	Fx	
R	Fy	
O	Fz	
Y	Mx	
Grn	My	
Blu	Mz	
V(pink)	+12V (12 to 15)	
Gry	-12V (12 to 15)	
W	Power COMMON	
Tan	Gnd, Signal Reference	
Bare	Shield drain, not connected to sensor body	

Final Inspection:

Calibration Date	3/8/09
Calibration Matrix	✓
Axis Orientation	✓
Units (lb and in-lbs	✓
Hardware Correct	✓
Label Correct	✓
Functional Test	✓
Inspection Date	4/2/09
Inspector Initial	

JR3

Multi-Axis Load Cell Technologies

FORCE-MOMENT SENSOR
SPECIFICATION SHEET

75E20S4-M125D-AF 1350L

Serial Number 4542

Analog calibration.

	Electrical Load Settings	Sensor Load Ratings	Calibration Loads used
Fx	1,350 lbs	1,350 lbs	400 lbs
Fy	1,350 lbs	1,350 lbs	400 lbs
Fz	1,500 lbs	2,700 lbs	400 lbs
Mx	6,000 in-lbs	10,125 in-lbs	2,600 in-lbs
My	6,000 in-lbs	10,125 in-lbs	2,600 in-lbs
Mz	3,000 in-lbs	10,125 in-lbs	2,600 in-lbs

Calibration Matrix: Multiply the calibration matrix and the sensor
Voltage vector to determine the loads.   (lb and in-lbs)

$$\begin{bmatrix} 261.17 & 0.23 & -0.15 & -6.46 & 2.69 & -0.86 \\ -0.91 & 262.77 & 1.35 & -0.93 & -8.94 & 0.79 \\ 8.73 & -1.49 & 297.54 & 2.06 & 1.86 & 1.56 \\ -11.39 & -29.62 & 0.43 & 1190.83 & -6.66 & -1.37 \\ 44.62 & -0.01 & 5.45 & -8.27 & 1218.80 & -1.01 \\ -8.19 & 7.77 & 13.29 & -5.46 & -7.61 & 592.36 \end{bmatrix} \begin{bmatrix} \text{Fx Volts} \\ \text{Fy Volts} \\ \text{Fz Volts} \\ \text{Mx Volts} \\ \text{My Volts} \\ \text{Mz Volts} \end{bmatrix}$$

Color		
Brn	Fx	
R	Fy	
O	Fz	
Y	Mx	
Grn	My	
Blu	Mz	
V(pink)	+12V (12 to 15)	
Gry	-12V (12 to 15)	
W	Power COMMON	
Tan	Gnd, Signal Reference	
Bare	Shield drain, not connected to sensor body	

Final Inspection:

Calibration Date	3/27/09
Calibration Matrix	✓
Axis Orientation	✓
Units (lb and in-lbs	✓
Hardware Correct	✓
Label Correct	✓
Functional Test	✓
Inspection Date	4/2/09
Inspector Initial	

Appendix B – Model Test Setups

Model 1
0.6 x 0.6 x 0.06 m

Model 2
1.8 x 0.6 x 0.06 m

Model 3
3.0 x 0.6 x 0.06 m

Model 4
0.6 x 0.6 x 0.2 m

Model 5
1.8 x 0.6 x 0.2 m

Model 6
3.0 x 0.6 x 0.2 m

Model 7
0.6 x 0.6 x 0.4 m

Model 8
1.8 x 0.6 x 0.4 m

Model 9
3.0 x 0.6 x 0.4 m